2002

Magnetic hysteresis and relaxation in Bi2212 single crystals doped with iron and lead

Krishna Kamal Uprety
University of Wollongong

MAGNETIC HYSTERESIS AND RELAXATION IN Bi2212 SINGLE CRYSTALS DOPED WITH IRON AND LEAD

A thesis submitted in fulfillment of the requirements
for the award of the degree

Doctor of Philosophy

from

University of Wollongong

by

KRISHNA KAMAL UPRETY, M.Sc., M. Eng.

INSTITUTE FOR SUPERCONDUCTING AND ELECTRONIC MATERIALS

&

FACULTY OF ENGINEERING

2002

CANDIDATE'S CERTIFICATE

This is to declare that the work presented in this thesis is original and was carried out by me in the laboratories of the Institute for Superconducting & Electronic Materials and Faculty of Engineering at the University of Wollongong, New South Wales, Australia. The document has not been submitted for a degree to any other university or institution.

Krishna Kamal Uprety

ACKNOWLEDGEMENT

I would like to express my most sincere appreciation and gratitude to my supervisors, Prof. S. X. Dou and Dr. J. Horvat for their unceasing academic guidance, encouragement and support throughout the course of this thesis work.

I would also like to give my sincere thanks to Prof. H.K. Liu, Dr. M. Ionescu, Dr X. L. Wang, Dr. M. Qin and Dr. A. Pan for their useful discussions and suggestions. Thanks are also due to Dr. G. D. Gu, University of New South Wales for providing Fe-doped Bi2212 single crystals.

I would also like to express sincere gratitude to Prof. E. H. Brandt for his valuable academic guidance during his short visit to ISEM. Also, special thanks are given to T. Silver and S. Bewlay for providing help in proof reading my papers and this thesis.

Many thanks go to all my friends and all the members at the Institute for Superconducting & Electronic Materials, and all the technicians at the Faculty of Engineering. Thanks also go to Mrs. B. M. Allen and Mrs J. De. Mestre for their help in administrative matters.

I would like to acknowledge the financial support of the University of Wollongong and DEET.

Finally, I wish to thank my wife Susmita for her encouragement, patience and support at home and my son Kusal, who was born in the third year of my PhD, for bringing me some pleasures during this work.

Abstract:

Magnetic hysteresis and magnetic relaxation measurements have been performed to study vortex pinning behaviour for $Bi_{2.1}Sr_{1.9}Ca_{1.0}(Cu_{1-y}Fe_y)_2O_{8+\delta}$ single crystals with Fe concentration y = 0, 0.005, 0.016 and 0.022 and for $Bi_{(2-x)}Pb_xSr_2CaCu_2O_{8+\delta}$ single crystals with Pb content x = 0.34. Here y = 0 is pure Bi2212 single crystal. The main objective of this thesis was to study mechanisms for the dramatically improved vortex pinning behaviour in Bi2212 single crystals with heavy Pb doping. It is argued that the strong vortex pinning behaviour in the heavily Pb doped Bi2212 single crystal came from improved *c*-axis conductivity i. e. a reduction in the resistivity anisotropy parameter. In heavily Pb doped Bi2212 single crystals, Pb resides between CuO_2 planes and thus reduces the anisotropy parameter significantly. Two microstructures such as Pb rich and Pb poor lamellar plates are also observed in heavily Pb doped Bi2212 single crystals. The Pb content in our crystal was relatively low. Therefore, these lamellar plates are not likely to dominate the vortex dynamics in our heavily Pb doped Bi2212 single crystal. However, no significant improvement in the vortex pinning behaviour has been observed in the Bi2212 single crystals with Fe doping. In iron doped Bi2212 single crystals, Fe substitutes Cu in the CuO_2 planes and does not decrease the anisotropy parameter.

A comparative study of the temperature dependence of the field $H_{peak}(T)$, at which the second magnetization peak occurs in $|M(H)|$, is made for pure, Fe doped and heavily Pb doped Bi2212 single crystals. The second magnetization peak, persisting close to the critical temperature T_c is observed for heavily Pb doped Bi2212 single crystals. The

second peak is not enhanced in Bi2212 single crystals after Fe doping. Pure and Fe doped Bi2212 single crystals have second peaks between temperatures 20 and 40 K. The peak field H_{peak} for all the crystals is observed to decrease with increasing temperatures, T. Comparative studies are also made on the temperature dependence of fields $H_{min}(T)$ and $H_{infl}(T)$, where $M(H)$ has a minimum between the first and second peaks at $H_{min}(T)$, and it has an inflection point on the low-field-side of the second peak at $H_{infl}(T)$. In pure and Fe doped Bi2212 single crystals, a pronounced peak in the derivative $|dM/dH|$ is observed corresponding to $H_{infl}(T)$, and $H_{infl}(T)$ is independent of temperature T. We relate this peak to the field $H_{dis}(T)$, an order-disorder field that separates a weakly elastically disordered vortex lattice from a plastically disordered vortex solid. A minimum in the normalized relaxation rate $S(H)$ is observed at H_{infl}, indicating two different flux-creep mechanisms above and below that field, and two different solid vortex phases. In heavily Pb doped single Bi2212 crystals, $H_{infl}(T)$ was observed to decrease with increasing T. However, in pure and Fe doped Bi2212 single crystals, $H_{infl}(T)$ was observed to be temperature independent. It is concluded that the negative slope of $H_{infl}(T)$ in heavily Pb doped Bi2212 crystals is related to the enhanced c-axis conductivity caused by the Pb sitting between the CuO_2 layers and causing 3D vortex lines, while in Fe doped Bi2212 crystals the defects sit on the CuO_2 planes and thus do not enhance the coupling between pancake vortices. The field H_{min} is observed to increase with temperature for pure and Fe doped Bi2212 single crystals. However, in heavily Pb doped Bi2212 single crystals, H_{min} is observed to decrease with T.

An increase in the crossover temperature T_{CR}, a temperature separating two different pinning regimes, has been observed with heavy Pb doping in Bi2212 single crystals. Discussion on these pinning regimes is presented in section 5.3. The increase of T_{CR}

may be interpreted as due to improved interlayer Josephson coupling of 2D vortices in Bi2212 crystal after heavy Pb doping. Heavily Pb doped crystal has $T_{CR} = 35K$ for the field that is within the second peak in its magnetic hysteresis loop. The T_{CR} in Fe doped crystal, however, did not change with Fe doping. For pure Bi2212 and Fe doped Bi2212 crystals, $T_{CR} = 19K$. The observed different results above or below T_{CR} in the current-voltage curve and in the effective activation energy have also suggested the different pinning regimes.

Comparative studies of the field dependence of the normalized critical current density, J_c/J_{c0}, have also been made for pure, Fe doped and heavily Pb doped Bi2212 single crystals. Below 20 K, pure and heavily Pb doped crystals showed a weak field dependence of J_c/J_{c0}, indicating strong vortex pinning behaviour. Above 20 K, all other crystals, except heavily Pb doped crystals show a strong field dependence of J_c/J_{c0}.

List of Figures

List of Tables

CHAPTER ONE: INTRODUCTION

1. 1 Introduction

Since the discovery of High T_c Superconductivity by Bednorz and Müller in 1986 [1], a tremendous number of research studies have been carried out with a hope of high T_c superconducting materials (HTS) operating above the liquid nitrogen boiling temperature (temperature greater than 77K) in technical applications. The first high T_c superconductor with a T_c higher than the boiling temperature of liquid nitrogen was $YBa_2Cu_3O_7$ (Y123), discovered by Wu et al. [2]. The highest T_c in Y123 was 93K. T_c values between 80K and 110K were reported by Maeda et al for $Bi_2Sr_2Ca_1Cu_2O_8$ (Bi2212) and $Bi_2Sr_2Ca_2Cu_3O_{10}$ (Bi2223) [3]. T_c = 20K was discovered for $Bi_2Sr_2Cu_1O_6$ (Bi2201) [4]. The highest T_c = 134 K was obtained for $HgBa_2Ca_2Cu_3O_8$ [5].

Y123 has a strong vortex pinning behaviour in comparison with Bi2212. The resistivity anisotropy parameter, $\gamma = \rho_c/\rho_{ab}$ for Y123 is approximately 10^3, whereas Bi2212 has $\gamma \approx 10^5$ [6,7]. This suggests that the strong vortex pinning in Y123 can arise from the strong coupling of the 2D pancake vortices. Furthermore, the *H-T* phase diagram of Y123 shows the presence of 3D vortex lines over a wide range of fields and temperatures [8]. Twin boundaries and grain boundaries are also suggested to act as a vortex pinning centers.

The other technologically most important superconductors are Bi2212 and Bi2223. For example, Bi2212 silver sheathed tapes show a critical current density higher than 2 ×

10^5 A/cm^2 at 4.2 K and 10 T [9]. This is well above the critical current density in the conventional superconductors NbTi and Nb_3Sn [9]. Bi2223 tapes show excellent performance at boiling temperature of liquid nitrogen. For instance, a critical current of 8×10^4 A/cm^2 is reached in short individual filaments extracted from multifilamentary tapes at 77 K ($H = 0$) [10].

Besides the technical applications, Bi2212 and Bi2223 systems are of great interest in the study of the vortex pinning behaviour of the HTS materials. The structure of the Bi-compounds can be viewed as a stack of CuO_2 layers interleaved with Ca layers and BiO layers and sandwiched between SrO layers. The formation energy of $Bi_2Sr_2Cu_1O_6$ (Bi2201), $Bi_2Sr_2Ca_1Cu_2O_8$ (Bi2212) and $Bi_2Sr_2Ca_2Cu_3O_{10}$ (Bi2223) phases is very close, preventing creation of a single phase (such as Bi2201 or Bi2212 or Bi2223) [11]. For example, the Bi2223 system is always contaminated by the Bi2212 and Bi2201 systems. The phase contamination (such as staking faults) is clearly seen in the intergrowth defects [11]. It is also not possible to synthesize large size Bi2223 single crystals to be used in the transport measurements. However, Bi2212 can be grown to large size single crystals with only single Bi2212 phase. The size of Bi2212 single crystals can be large enough to permit all types of transport and magnetization measurements in order to study vortex pinning behaviour.

It is well established that in layered HTS superconductors, the vortices for an applied field parallel to the c-axis are described in terms of pancake vortices. For less anisotropic materials (such as Y123), the pancake vortices are coupled through Josephson currents to form 3D vortex lines. However, for the highly anisotropic materials (such as Bi2212), the pancake vortices are decoupled due to thermal energy.

With a current passing through such superconductor, the decoupled pancake vortices move under the influence of the Lorentz force, producing energy dissipation. This dissipation is one of the serious problems in bringing these materials into technical application. However, the dissipation can be reduced by improving the vortex pinning and this can be done by introducing pinning centres or improving the Josephson coupling of the pancake vortices.

In Bi2212 single crystal with heavy Pb doping, a dramatic improvement in the vortex pinning behaviour has been reported [12, 13]. Two microstructures i. e. lead reach and lead poor lamellar plates are reported in heavily Pb doped $Bi_{2.2-x}Pb_xSr_{1.8}CaCu_2O_{8+\delta}$ for x > 0.4 [12]. It has been reported that the observed microstructures are responsible for the improved vortex pinning behaviour in heavily Pb doped Bi2212 single crystals [12]. Besides these lamellar microstructures, a significant reduction in the resistivity anisotropy parameter that leads to one order of magnitude larger *c*-axis conductivity, has been reported in Bi2212 single crystals after heavy Pb doping [7]. Further, significant increment in the Josephson coupling has also been reported in heavily Pb doped single crystals [6].

In this thesis, we study the vortex pinning properties of the heavily Pb doped Bi2212 single crystals, which helped us assess whether the lamellar structure or improved c-axis conductivity are a prevailing factor behind the improved pinning. A comparison study of this vortex pinning has also been made with Bi2212 single crystals doped with various concentration of Fe. In a heavily Pb doped Bi2212 crystal, it is known that the Pb ions sit between the CuO_2 planes and thus reduces the anisotropy parameter [6,7,12]. Our magnetic hysteresis and magnetic relaxation results showed a strong vortex pinning

in heavily Pb doped Bi2212 single crystal. Based on our observed experimental, we have proposed that strong pinning behaviour in heavily Pb doped Bi2212 single crystal arises from the improved inter-layer coupling of 2D pancake vortices. This is a consequence of improved c-axis conductivity with heavy Pb Doping. A decrease of order-disorder transition field H_{dis} with temperature T for heavily Pb doped Bi2212 single crystal was also related to the improved inter-layer coupling. Here, H_{dis} is a field that separates a weakly (elastically) disordered quasilattice from a highly (plastically) disordered solid phase [14,15]. We have also shown that the vortex pinning in Bi2212 single crystals is not improved by Fe doping. In Fe doped Bi2212 single crystals, Fe sits on CuO_2 planes and does not improve the c-axis coupling [16]. As a consequence of this, we observed a temperature independent H_{dis} for the pure and Fe doped Bi2212 single crystals. A temperature independent H_{dis} has also been confirmed by Hall Probe measurements in pure Bi2212 single crystals [17].

1.2 References for Chapter One

1. J. G. Bednortz and K. A. Mullar, Z. *Phys. B* **64,** 189 (1986).
2. M. K. Wu, J. R. asburn, C. J. Torng, P. H. Hor, R. L. Meng, L. Gao, Z. J. Huang, Y. Q. Wang and C. W. Chu, *Phys. Rev. Lett.* **58,** 908 (1987).
3. H. Maeda, Y. Tanaka, M. Fukutomi and T. Asano, *Japan J. Appl. Phys.* **27,** L209 (1988).
4. C. Michel, M. Herviev, M. M. Borel, A. Grandin, f. Deslands, J. Provost and B. Raveau, *Z. Phys. B* **68,** 421 (1987).
5. L. Gao, Y. Y. Xue, F. Chen, Q. Xiong, R. L. Meng, D. Ramirez, C. W. Chu, J. H. Eggert and H. K. Mao, *Phys. Rev B* **50,** 4260 (1994).
6. L. Winkeler, S. Sadewasser, B. Beschoten, H. Frank, F. Nouvertne and G. Guntherrodt, *Physica C* **265,** 194 (1996).
7. T. Motohashi, Y. Nakayama, T. Fujita, K. Kitazawa, J. Shimoyama and K. Kishio, *Phys. Rev. B* **59,** 14080 (1999).
8. G. Blatter, M. V. Feigel'man, V. V. Geshkenbein, A. I. Larkin, V. M. Vinokur, *Rev. Mod. Phys* **66,** 1125 (1994).
9. A. P. Malozemoff, Q. Li and S. Fleshler *Physica C,* **282-287,** 424 (1998).
10. A. Polyanskii, V. M. Beilin, E. Yashchin, A. Goldgirsh, M. Roth and D. Larbalestier, *IEEE Trans. Appl. Supercond,* **11,** 3736 (2001).
11. C. H. Chen, *Physical properties of high temperature superconductors II,* D. M. Ginsberg ed., World Scientific, Singapure, p. 242-252 (1990).
12. Z. Hiroi, I. Chong and M. Takano, *J. Solid State Chem*,**138,** 98 (1998).
13. I. Chong, Z. Hiroi, M. Izumi, J. Shimoyama, Y. Nakayama, K. Kishio, T. Terashima, Y. Bando, M. Takano, *Science*, **276**, 770 (1997).

14. T. Nishiziki, T. Naito, S. Okayasu, A. Iwase, and N. Kobayashi, *Phys. Rev. B*, **61**, 3649 (2000).

15. D. Giller, A. Shaulov, R. Abulafia, Y. Wolfus, L. Burlachkov, and Y. Yeshurun, *Phys. Rev. Lett.*, 79, 2542 (1997).

16. B. vom Hedt, W. Lisseck, K. Westerholt and H. Bach, *Phys. Rev. B* **49,** 9898 (1994).

17. B. Khaykovich, E. Zeldov, D. Majer, T. W. Li, P. H. Kes and M. Konczykowski, *Phys. Rev. Lett.* **76**, 2555 (1996).

CHAPTER TWO: LITERATURE REVIEW

2.1. Models and Theories

2.1.1 London's Local Electrodynamics

F. and H. London developed a phenomenological theory to describe the electromagnetic behaviour of superconductors [1].They postulated two equations. The first equation describes a relationship between the electric field $\boldsymbol{E}$ and the supercurrent $\boldsymbol{J}_s$:

$$\frac{d\boldsymbol{J}_s}{dt} = \frac{n_s e^2}{m}\boldsymbol{E} \qquad (2.1.1.1)$$

Here n_S, e, m are, respectively, the density of superconducting electrons, the electronic charge and the mass of the electron.

The second equation describes a relationship between the supercurrent density $\boldsymbol{J}_S$ and the magnetic field $\boldsymbol{H}$:

$$\nabla \times \boldsymbol{J}_s = -\frac{n_s e^2}{m}\boldsymbol{H} \qquad (2.1.1.2)$$

Here, the supercurrent density $\boldsymbol{J}_S$ has a local relation with the vector potential $\boldsymbol{A}$ since $\boldsymbol{H} = \nabla \times \boldsymbol{A}$. The second equation leads to the Meissner effect. These two postulations are used to obtain an expression for the exponential decrease of magnetic field with the distance from the surface of the superconductor:

$$H(x) = H(0)\exp(-x/\lambda_L) \qquad (2.1.1.3)$$

The magnetic field vanishes in the bulk of the superconductor, and one obtains perfect diamagnetism, as required for the complete Meissner effect. Here, $\lambda_L = \left(mc^2/4\pi n_s e^2\right)^{1/2}$

is called the London penetration depth and represents the characteristic decay length of the magnetic field within the superconductor.

The temperature dependence of the London penetration depth, $\lambda_L(T)$, can be obtained from the Gorter and Casimir model, and it is equal to $\lambda_L(T) = \lambda_L(0)/\left[1-(T/T_c)^4\right]^{1/2}$. This is very close to the experimental results for pure superconductors. From this equation, we see that for $T = T_c$, $\lambda_L \to \infty$ (infinite) so that no flux is excluded at T_c. As T drops infinitesimally below T_c, λ_L decreases rapidly, thereby establishing the Meissner effect in the bulk of superconductors for all temperatures below T_c.

2.1.2 Pippard's Non-Local Electrodynamics

The relation between the vector potential $\boldsymbol{A}$ and the supercurrent density $\boldsymbol{J}_s$ in London's equation is a local relation. This is because the supercurrent density $\boldsymbol{J}_s$ at a point $\boldsymbol{r}$ is determined by the vector potential $\boldsymbol{A}$ at the same point $\boldsymbol{r}$. However, Pippard, on the basis of numerous experimental results, suggested that the relation between current density and vector potential should be non-local [1]. He proposed that the current density $\boldsymbol{J}_s(\boldsymbol{r})$ at a given point in space is determined by the values of $\boldsymbol{A}$ within a distance ξ_0 of the point $\boldsymbol{r}$, where ξ_0 is the intrinsic coherence length (also called the Pippard coherence length). In the case of impure superconductors, the Pippard coherence length (ξ_0) may be larger than the mean free path for elastic scattering l. In this case, the relation between $\boldsymbol{J}_s$ and $\boldsymbol{A}$ is non local, however, the range of interaction is shorter i. e $\xi < \xi_0$. In the dirty limit, the coherence length is ξ given by: $1/\xi = 1/\xi_0 + 1/\alpha_i l$, where α_i is an

empirical constant near unity. The coherence length ξ is important in determining the energy of the boundaries between superconducting and normal regions.

2.1.3 Ginzburg -Landau (GL) Phenomenology

The G-L macroscopic theory extends the local electrodynamics described by the London equation with further consideration of the spatially varying superconducting order parameter [1]. It is based on Landau's general phenomenology of second order phase transitions in terms of the order parameter expansion and the symmetry of a free energy functional. The theory in its original form was valid only close to the critical temperature $(T_c\text{-}T)/T_c << 1$ where the order parameter was small and slowly varying with T. Later, it was extended to arbitrary temperatures but in a region close to the critical field H_{c2}.

The crucial insight in G-L theory was that for a superconductor, the order parameter must be identified with the macroscopic wave function i. e. $\Psi(\boldsymbol{r}) = \sqrt{n_s(\boldsymbol{r})/n}\exp(i\theta)$, where θ is the phase factor, n_s is the supercurrent density and n is the charge carrier density.

For temperatures close to the critical temperature, the superconducting carriers are only present in very small quantities, and G-L was able to define the free energy density $F(\Psi(r),T)$ by expanding it as a power series in $|\Psi|^2$.

For an isotropic and homogenous system in a magnetic field, the free energy function becomes

$$F = \int\left(a(T)|\Psi|^2 + b(T)/2|\Psi|^4 + (n/2)m^*\left|\{-ih\Delta/2\pi\} - e^*\boldsymbol{A}/c\right|^2 + H^2/8\pi \right).d\boldsymbol{r} \quad (2.1.3.1)$$

The two quantities $a(T)$ and $b(T)$ are experimentally measurable. The m^* and e^* are respectively, the effective mass and effective charge of the electrons. $\boldsymbol{H}$ is the macroscopic magnetic field and $\boldsymbol{A}$ is the vector potential.

A relation for current density $\boldsymbol{J}_s$ can be obtained from the G-L free energy function.

$$\boldsymbol{J}_s = -\frac{ie^*h}{4\pi m^*}\left(\Psi^*\Delta\Psi - \Psi\Delta\Psi^*\right) + \frac{e^{*2}}{m^*c}\left(\Psi^*\Psi\right)\boldsymbol{A} \qquad (2.1.3.2)$$

where $\nabla \times \boldsymbol{H} = 4\pi\boldsymbol{J}_s / c$. The first term in the above equation refers to the paramagnetic current, and the second term refers to the diamagnetic current. For a purely real wave function, ψ, the paramagnetic term becomes zero and the diamagnetic term gives

$\boldsymbol{J}_s = \frac{n_s e^{*2}}{m^* c}|\Psi|^2 \boldsymbol{A}$, which is defined in the London theory.

Two very important characteristic length scales: the penetration depth $\lambda_L(T) = \left|m^* c^2 b(T) / 4\pi n_s e^{*2} a(T)\right|$ and the coherence length $\xi(T) = \left[\hbar^2 n_s / 2m^* a(T)\right]^{1/2}$ can be obtained from the G-L theory. Here the temperature dependent coherence length $\xi(T)$ and penetration depth $\lambda(T)$ are given as

$$\xi(T) = \xi(0)(T - T/T_c)^{-1/2} \qquad (2.1.3.3)$$

$$\lambda_L(T) = \lambda_L(0)(T - T/T_c)^{-1/2} \qquad (2.1.3.4)$$

The ratio λ_L / ξ defines the Ginzburg-Landau parameter κ. The significance of $\lambda_L / \xi = \kappa$ is in describing regimes where the interfacial energy between superconducting and normal materials is positive or negative. For $\kappa < 1/\sqrt{2}$ the interfacial energy $[\sigma \approx -\frac{H_c^2}{8\pi}(\lambda_L - \xi)]$ is positive and the material favours a complete expulsion of the

flux lines. In other words, the superconductor shows a complete Meissner effect. In a pure superconductor, magnetic flux is expelled completely upon field cooling (FC). The total induction field $\boldsymbol{B} = \boldsymbol{H} + 4\pi\boldsymbol{M}$ is zero inside this superconductor and the susceptibility $\chi \cong M/H = -1/4\pi$ indicating perfect diamagnetic properties. These are called Type I superconductors. For $\kappa > 1/\sqrt{2}$ the interfacial energy $[\sigma \approx -\frac{H_c^2}{8\pi}(\lambda_L - \xi)]$ is negative and the material favours the admission of flux lines. These superconductors are called impure superconductors, where there are normal conducting regions inside the bulk of the superconductor. These superconductors are called Type II superconductor. Type II superconductors have two critical fields: the lower critical field H_{c1} and the upper critical field H_{c2}. The perfect diamagnetic state (Meissner phase) in these superconductors persists only to a lower critical field, H_{c1}. The persistence of superconductivity above H_{c1} is explained in terms of a mixed state in which the superconductor coexists with quantized units of magnetic flux called vortices. The H-T phase diagram in Type II superconductors therefore exhibits a single Meissner phase for $H < H_{c1}(T)$, a mixed state for $H_{c1} < H < H_{c2}$ and a normal state phase above $H > H_{c2}$.

2.1.4 Microscopic (BCS) Theory of Superconductivity

In 1957, J. Bardeen, L. N. Cooper and J. R. Schriefer proposed a microscopic theory of superconductivity [1]. This theory is strictly valid for the low temperature superconductors. The main idea of this theory is electron pairing $(k\uparrow, -k\downarrow)$ of conduction electrons in the superconductor, by a phonon. They are called Cooper pairs.

The BCS Hamiltonian is given as:

$$H_{red}^{BCS} = \sum_{k\alpha} E_k C_{k\alpha}^{+} C_{k\alpha} - V_0 \sum_{kk'} C_{k\uparrow}^{+} C_{-k\downarrow}^{+} C_{-k'\uparrow} C_{-k'\downarrow} \qquad (2.1.4.1)$$

where $E_k = \frac{\hbar^2 k_F^2}{2m}$ is the kinetic energy , the $C_{k\uparrow}^{+} C_{-k\downarrow}^{+}$ operator creates a Cooper pair and the conjugate of this annihilates a pair. The second term in the BCS Hamiltonian represents an interaction with attractive potential V_0.

The BCS wave function is

$$|\Psi_{BCS}\rangle = \prod_k \left[u_k + v_k C_{k\uparrow}^{+} C_{-k\downarrow}^{+}\right]|0\rangle, \qquad (2.1.4.2)$$

with $|u_k|^2 + |v_k|^2 = 1$,where $|u_k|^2$ is the probability that the $(k\uparrow, -k\downarrow)$state is empty and $|v_k|^2$ is the probability that the $(k\uparrow, -k\downarrow)$ state is occupied. $|0\rangle$ is the state with no Cooper pairs. The main point of the BCS wave function is that if $k\uparrow$ is occupied, then $-k\downarrow$ is also occupied.

The important results obtained from BCS theory are summarised below.

- The critical gap ratio $2\Delta(0)/k_B T = 3.52$ agrees very well with experimental results. Here $\Delta(0)$ is the binding energy per charge carrier in the pairing process and k_B is the Boltzmann constant. For example the gap ratio for Al is 3.4 and for Sn is 3.5. The deviation from the BCS value may be due to isotopic impurity
- The discontinuity of the specific heat ΔC at T_c is $\Delta C/k_B T$ =1.43.
- The coherence length is obtained as $\xi_0 = 0.18\hbar v_F / k_B T_c$.

- The critical field $H_C^2/8\pi = 2\Delta^2(0)\mathrm{N}(0)$, as calculated from the BCS ground state energy, is in reasonably good agreement with the experimental results. Here, $\Delta(0)\mathrm{N}(0)$ is the energy difference between the superconducting ground state and the normal ground state.

2.1.5 Structure of an Isolated Vortex

The structure of an isolated vortex can be described by using the modified London theory [2, 3]. For large κ materials, with the Ginzburg-Landau theory one can obtain a spatial variation of the superconducting order parameter over a distance, ξ, which is small compared to the range of field penetration. In such circumstance, the single quantized unit of flux, ϕ_0 can be described by the δ function.

In this case, the London theory can be written as follows,

$$\nabla^2 \boldsymbol{H} - \left(\frac{n_s e^2}{m}\right)^2 \boldsymbol{H} = -\frac{\phi_0}{\lambda_L^2}\delta(\boldsymbol{r}) \qquad (2.4.1.1)$$

By considering the cylindrical shape of the vortex line, the solution for $\boldsymbol{H}$ in the cylindrical coordinate system is:

$$H = \frac{\phi_0}{2\pi\lambda_L^2} K_0\left(\frac{r}{\lambda_L}\right) \qquad (2.1.4.2)$$

where $K_0(r/\lambda_L)$ is a hyperbolic Bessel function of order zero and imaginary arguments.

The above equation has two solutions

Case 1: when $\xi < r << \lambda_L$

$$H \cong \frac{\phi_0}{2\pi\lambda_L^2}\left[\ln\left(\frac{\lambda_L}{r}\right) + 0.12\right] \qquad (2.1.4.3)$$

This equation diverges for small r, and in order to prevent this divergence r must be truncated by choosing $r = \xi$ for a small r [2, 3]. Here $r = \xi$ describes the normal core of the vortex line. In G-L theory, the ratio $\lambda_L / \xi = \kappa$ is a fundamental parameter of the superconductor.

Case 2: when $r >> \lambda_L$

$$H \cong \frac{\phi_0}{2\pi\lambda_L^2}\left(\frac{\pi\lambda_L}{2r}\right)^{1/2} e^{-r/\lambda_L} \qquad (2.1.4.4)$$

H in equation (2.1.4.4) decreases exponentially with r. The distance at which H decays exponentially is given by the London penetration depth, λ_L. Here, λ_L gives the outer radius of the vortex line.

2.2 Crystallographic Structures of High T_c Superconductors

2.2.1 $YBa_2Cu_3O_{7-\delta}$ (Y123)

$YBa_2Cu_3O_{7-\delta}$ (Y123) was discovered by Wu in late 1986 [4]. This was the first compound for which T_c exceeded the liquid nitrogen boiling temperature 77 *K*. This discovery has initiated an unprecedented level of world-wide activity due to the great possible technological potential of superconductivity in industry. The $YBa_2Cu_3O_{7-\delta}$ compound has both orthorhombic (δ = 0.0-0.2) and tetragonal ($\delta > 0.2$) structures [5]. The orthorhombic structure is a superconducting phase, while the tetragonal structure is a non-superconducting phase. Figure 2.2.1 shows the orthorhombic crystal structure of Y123. This figure has three perovskite-like cubes with four different layers stacked sequentially as BaO – CuO – BaO - CuO_2 – Y - CuO_2 – BaO – CuO - BaO [5]. Yittrium (Y) and Barium (Ba) atoms are positioned in the center of the cubes. There are two CuO_2 layers in a unit cell and they are connected by a Y ion. Oxygen sites in these CuO_2 layers are fully occupied. The CuO_2 layers are the regions in which the superconducting condensate resides and they are usually known as copper oxide planes. There are no oxygen atoms in the plane containing the Y. Oxygen sites in the Ba plane are fully occupied. There are also two CuO layers in a unit cell. Unlike the CuO_2 layers, the CuO layers do not have fully occupied oxygen sites. Oxygen in CuO layers occupies sites between the copper atom along the a-axis (OB1 sites) and along the b-axis (OA1 sites). For $\delta = 1$, OA1 sites are fully occupied and OB1 sites are empty. With no oxygen atoms in the OB1 sites, the structures consisting of copper and oxygen atoms oriented along the b-axis are usually called the CuO chain. The CuO chain is termed a charge

reservoir because the charge carriers are injected into CuO_2 planes from the chains. T_c is affected by varying the number of oxygen atoms in the chain.

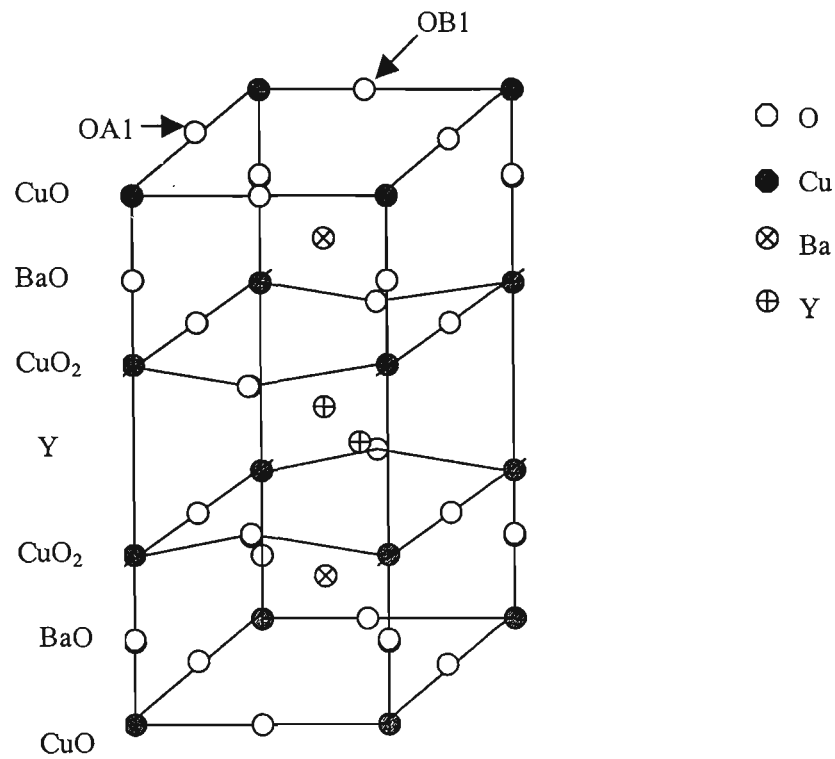

Fig. 2.2.1: Crystal structure of $YBa_2Cu_3O_{7-\delta}$ (Y123) [ref.5].

2.2.2 $Bi_2Sr_2Ca_{n-1}Cu_nO_{2n+4}$ (BSCCO)

A series of $Bi_2Sr_2Ca_{n-1}Cu_nO_{2n+4+\delta}$ compounds exists in the Bi-Sr-Ca-Cu-O system. The best known are the compounds with n = 1 to 3, namely $Bi_2Sr_2CuO_{6+\delta}$ (Bi2201), $Bi_2Sr_2CaCu_2O_{8+\delta}$ (Bi2212) and $Bi_2Sr_2Ca_2Cu_3O_{10+\delta}$ (Bi2223). Superconductivity in the Bi2201 system was discovered by Michel et al. at a relatively low critical temperature

T_c = 20K [6]. The addition of Ca and Cu to this Bi2201 system led to the report of a superconducting transition between 80K and 110K by Maeda et al. (Bi2212 and Bi2223 phases) [7]. Though the basic topology is simple, the structures in $Bi_2Sr_2Ca_{n-1}Cu_nO_{2n+4+\delta}$ compounds are always complicated by incommensurate modulation, oxygen nonstoichiometry, cation disorder and layer stacking faults [8-11]. The three principal structures of the BSCCO family are described below.

2.2.2.1 $Bi_2Sr_2CuO_{6+\delta}$ (2201)

The Bi2201 structure has one CuO_2 plane sandwiched between two SrO layers. The Cu ion in the plane is coordinated by O1 oxygen. The distance between Cu-O1 is 1.9 Å. The oxygen O2 lies above and below each Cu ion forming an extremely elongated CuO_6 octahedron (Cu-O2 =2.6 Å). The strontium ion has nine nearest oxygen ions with an average Sr-O distance of about 2.7 Å. In the Bi_2O_2 bilayers, Bi has a very distorted octahedral coordination. The distance between Bi and O2 is 2 Å. The Bi-O3 bond, which joins adjacent sheets in Bi_2O_2 bilayers is larger than 3 Å. This long and weak Bi-O3 bond parallel to the c axis results in very weak interlayer bonding and mica-like mechanical behavior in all Bi superconductors. The subcell structure of Bi-based oxide superconductors is given in Figure 2.2.2.1. The Bi2201 phase (Fig. 2.2.2.1) has a pseudotetragonal symmetry with lattice parameters $a \approx b \approx 5.4$ Å and $c \approx 24.4$ Å [5,12]. The unit-cell of Bi2201 contains four formula units and is a stack of atomic planes in the sequence $(BiO)_2/SrO/CuO_2$ /SrO/ $(BiO)_2/SrO/CuO_2/SrO/(BiO)_2$. Bi2201 has only one CuO_2 plane and it is sandwiched between two SrO planes.

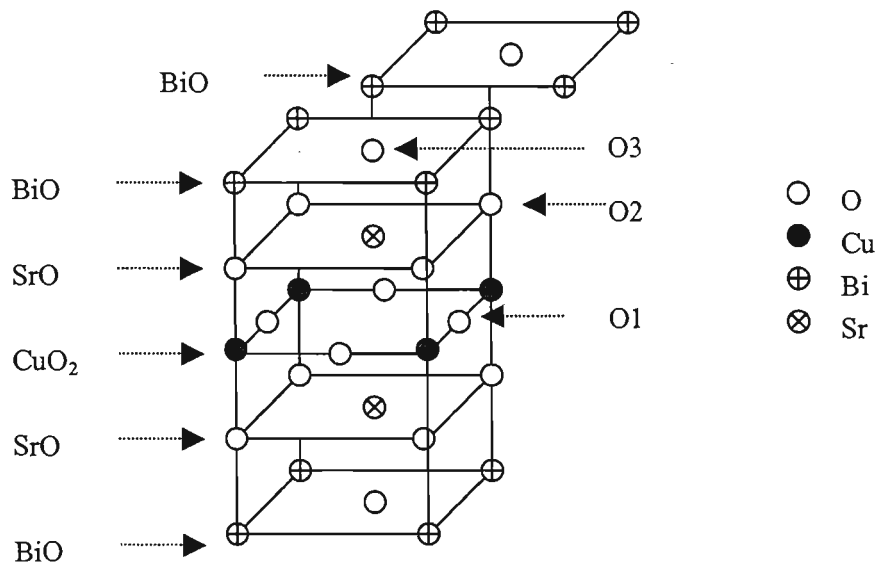

Fig. 2.2.2.1: Crystal structure of $Bi_2Sr_2CuO_{6+\delta}$ (Bi2201) [ref.5].

2.2.2.2 $Bi_2Sr_2CaCu_2O_{8+\delta}$ (2212)

The 2212 structure is similar to that of 2201 structure except that the CuO_2 plane is replaced by a set of three planes: $CuO_2/Ca/CuO_2$. Calcium adopts an eight-fold-coordination, similar to the Y in Y123. There is no oxygen in this plane, so Cu atoms have only five nearest neighbors in a square coordination, rather than the elongated octahedral coordination of 2201.The unit-cell of Bi2212 contains four formula units and is a stack of atomic planes in the sequence $(BiO)_2/SrO/CuO_2/Ca/CuO_2$ /SrO/$(BiO)_2$/ SrO /CuO_2/Ca/CuO_2/SrO. The Bi2212 phase (Fig. 2.2.2.2) has a pseudo-orthorhombic structure with lattice parameters $a \approx b \approx 5.4$ Å and $c \approx 30.8$ Å [5, 12]. Oxygen content in

the unit cell determines the T_c. Extra oxygen in the unit cell can be inserted into the BiO layers. In Bi2212 single crystal, the maximum T_c = 92 K has been reported for δ = 0.29, whereas for δ = 0.22, T_c = 70 K and for δ = 0.29, T_c = 87.5 K [13]. The authors have reported that the variation of the oxygen content results in structural distortion and change in the c-axis parameter. These effects are suggested for inducing the charge transfer to the CuO_2 planes, causing variation in T_c.

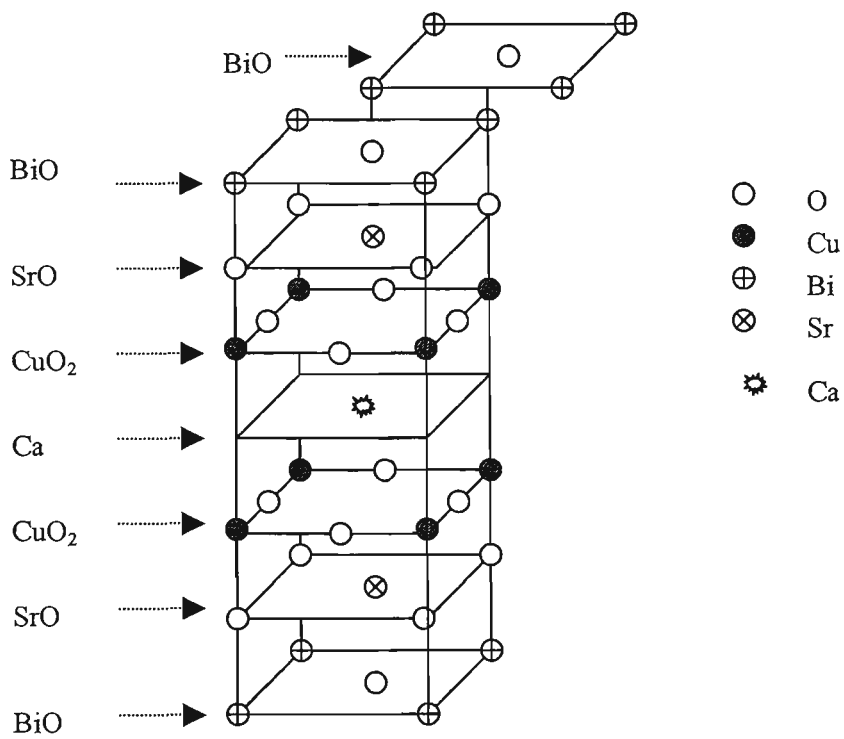

Fig. 2.2.2.2: Crystal structure of $Bi_2Sr_2CaCu_2O_{8+\delta}$ (Bi-2212) [ref.5].

2.2.2.3 $Bi_2Sr_2Ca_2Cu_3O_{10+\delta}$ (2223)

The Bi2223 structure has a simple relationship with Bi2212 structure. Additional Ca and CuO_2 layers are inserted within the CuO_2/Ca/CuO_2 layers, giving a CuO_2/Ca/CuO_2/Ca/CuO_2 sub-structure. The unit-cell of Bi2223 contains four formula units and is a stack of atomic planes in the sequence $(BiO)_2$/SrO/CuO_2/Ca /CuO_2/Ca/ CuO_2/SrO/$(BiO)_2$/SrO/CuO_2/Ca/CuO_2/SrO (Fig.2.2.2.3). Bi2223 has a pseudotetragonal symmetry with lattice parameters a ≈ b ≈ 3.9 Å and c ≈ 37 Å [5,12].

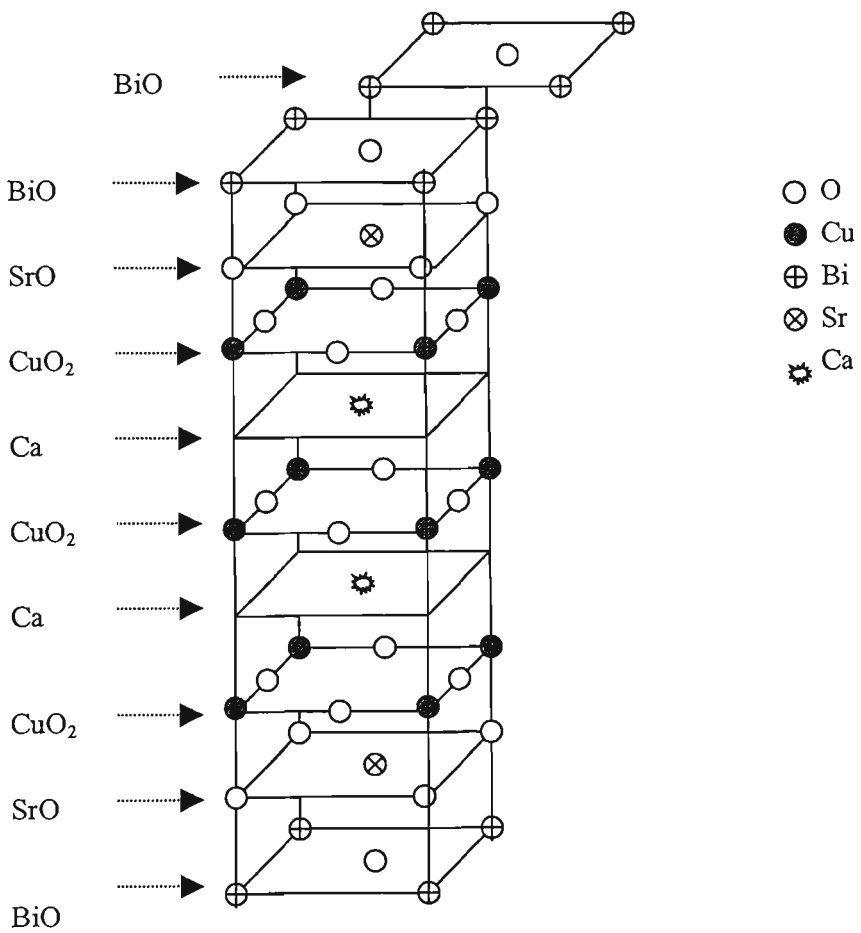

Fig. 2.2.2.3: Crystal structure of $Bi_2Sr_2Ca_2Cu_3O_{10+\delta}$ (Bi-2223) [ref.5].

2.1 Vortex Matter in High T_c Superconductors

All high temperature superconductors are Type II superconductors. In the absence of defects, a vortex lattice is observed. Distortions of the vortex lattice are caused by pinning defects, such as impurities, columnar defects, oxygen vacancies and stacking faults. The high transition temperature and small coherence lengths in these materials lead to large thermal activation of the vortex lines. The thermal fluctuations lead to the depinning of the vortex lines above a characteristic irreversibility line $T_{irr}(H)$. Generally speaking, the vortices below this line are in a vortex solid state. Above $T_{irr}(H)$, the magnetization of the sample is fully reversible. The vortices above the melting line $T_m(H)$ are in the vortex liquid state.

2.3.1 Types of Vortices

2.3.1.1 Abrikosov Vortices

In 1957, Abrikosov proposed that magnetic fields penetrate the bulk of Type II superconductors in tubes or cylinders called Abrikosov vortices [14]. The internal structure of an isolated Abrikosov vortex line is shown in Fig.2.3.1.1. At large distances, the magnetic induction field $\boldsymbol{B}$ falls off exponentially with the radial distance from the center of the flux line and has a characteristic decay length, λ. The Abrikosov vortex line has a core with a radius approximately equal to the superconducting coherence length, ξ. In this inner core, the superconducting order parameter, $|\psi|$, is suppressed, see Fig. 2.3.1.1. In comparison to this, $|\psi| = 0$ for $r < \xi$ in the London approximation. In high temperature superconductors (HTS), Abrikosov vortices are obtained when the field is applied parallel to the c axis. The value of λ_{ab} in HTS is

1000-2000 Å and ξ_{ab} is 10-20 Å [15]. Here, λ_{ab} and ξ_{ab} are the London penetration depth and coherence length along *ab*- plane, respectively.

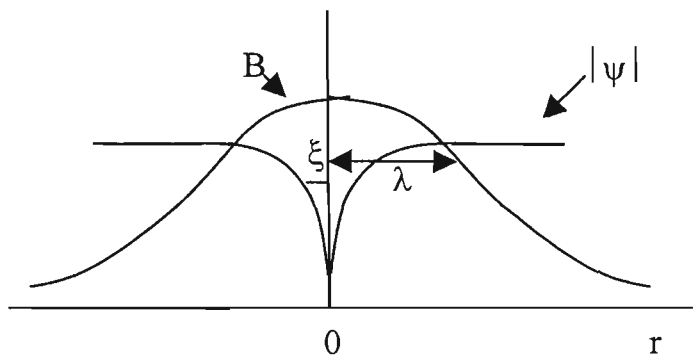

Figure 2.3.1.1: Illustration of the internal structure of an isolated Abrikosov vortex line. Here λ is the penetration depth and ξ is the coherence length. In the figure, $|\psi|$ varies continuously from r = 0 to a constant value at r >ξ and B decreases exponentially as r decreases with a characteristic length scale, λ [ref.15].

2.3.1.2 Josephson Vortices

When a magnetic field ***H*** is applied parallel to the *ab*-planes in a strongly layered superconductor, Josephson vortices are obtained [15,16]. Figure 2.3.1.2 shows the Josephson vortices in a strongly layered superconductor. In the figure, the vertical lines between the layers are Josephson currents and the horizontal arrows are supercurrent inside the CuO_2 layers. The Josephson current in *z*-direction is determined by the phase difference $J_z = J_{c0}\ sin\ (\varphi_{n+1} - \varphi_n)$. Here j_{c0} is the critical Josephson current density. The thickness of Josephson vortices is t_J and their width is $\Lambda = t_J.\Gamma$, where $\Gamma = \xi_{ab} / \xi_c$. Here,

ξ_{ab} , ξ_c are the coherence lengths along the *ab*-plane and *c*-axis, respectively. Josephson vortices have no cores [15,16]. Dashed lines are CuO_2 layers

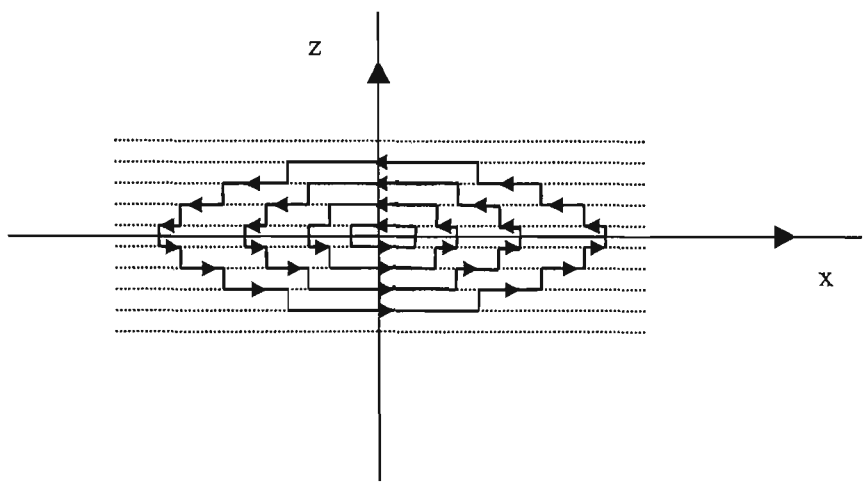

Figure 2.3.1.2: Sketch of the supercurrent distribution around a single Josephson vortex in a strongly layered superconductor [ref.16].

2.3.2 Types of Vortex Matter

In high temperature superconductors, due to their high critical temperatures and large anisotropy, magnetic vortex matter can have four main configurations [15]. These are the three dimensional (3D) vortex solid phase (Fig. 2.3.2.1a), the three dimensional (3D) vortex liquid phase (Fig.2.3.2.1b,c), the two dimensional (2D) vortex solid phase (or 2D pancake vortex phase) (Fig. 2.3.2.1d) and the two dimensional (2D) vortex liquid phase [15, 17, 18]. It is also observed that the 3D vortex phase can have two configurations: the disentangled (Fig. 2.3.2.1b) and entangled vortex phases (Fig.2.3.2.1c).

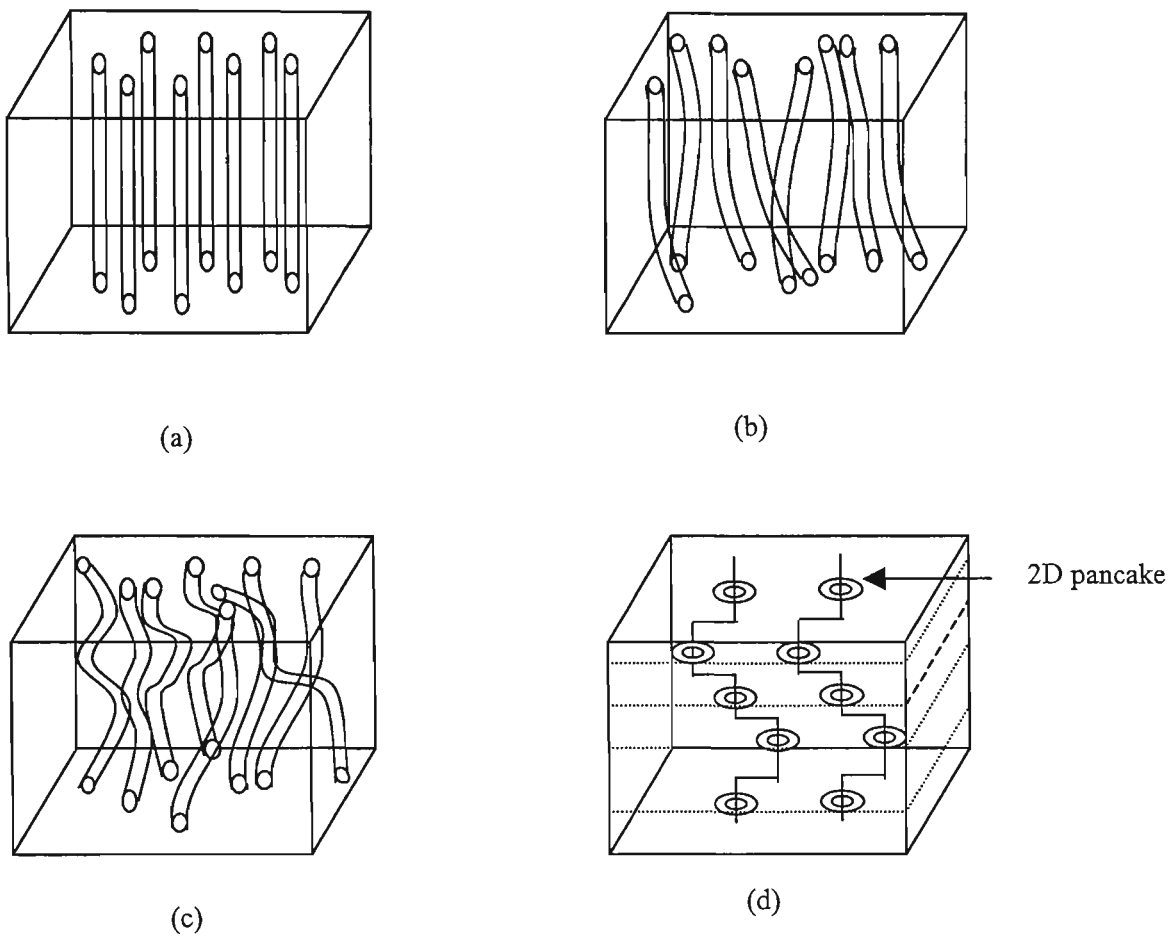

Fig. 2.3.2.1: Various equilibrium phases for a vortex system: (a) 3D vortex solid phase (b) 3D disentangled vortex liquid phase (c) 3D entangled liquid phase (d) 2D pancake solid phase [ref.15].

Fig. 2.3.2.1d describes the vortex structure in a strongly layered high T_c superconductor when a magnetic field H is applied perpendicular to the CuO_2 planes. The 2D pancake vortices directed along the c axis are coupled by Josephson vortices whose axes thread through the junctions between the superconducting layers.

2.3.3 Irreversibility and Melting of Vortex Solid

One of the extensively studied characteristic features of high T_c superconductivity is the irreversibility line, *IL* [19-21]. The irreversibility line divides the magnetic (*H-T*) phase diagram into two parts: above the irreversibility line, magnetization of the sample is fully reversible, whereas below the *IL*, a hysteresis effect is observed. The field cooled magnetization (M_{FC}) measured upon cooling coincides with the zero field magnetization (M_{ZFC}) measured upon warming above $T_{irr}(H)$. In M_{ZFC}, the sample is first cooled in a zero field from above the critical temperature. Then a field is applied and the magnetic moment as a function of slowly increasing temperature is measured. In M_{FC}, the magnetic moment as a function of decreasing temperature is measured with a constant field from above T_c.

The vortex-lattice melting line is defined as a line that separates a vortex solid phase from a vortex liquid phase. Extensive research work has been done to study vortex melting in Bi2212 single crystals by using different techniques [19-24]. The simplest melting criterion for the vortex lattice can be stated in terms of the Lindemann criterion [25], which predicts a melting transition as the thermal fluctuations of its constitutive vortex lines as the mean squared amplitude of the fluctuations $\langle u^2 \rangle_{th}^{1/2}$ increases beyond a certain fraction of the lattice constant a_0:

$$\langle u^2 \rangle_{th}^{1/2} \approx c_L^2 a_0^2 \qquad (2.3.3.1)$$

where the Lindemann number c_L = 0.1 –0.02. The shape of the melting line over a broad range of magnetic fields can also be estimated with the use of the Lindemann criterion [15].

2.3.4 Elastic Constant of the Vortex Lattice

Distortion of the vortex lattice can be described within the framework of elastic continuum theory and characterized by elastic modulii for tilt (C_{44}), shear (C_{66}), uniaxial compression (C_{11}) and isotropic compression (C_{11}-C_{66}). In collective pinning theory, the elastic moduli are important, determining correlated volume $V_c = R_c^2 / L_c$[see, section 2.7.1]. Here, $R_c \cong \sqrt{(C_{44}C_{66}^3)}\xi^2 / W$ and $L_c \cong R_c\sqrt{C_{44}/C_{66}}$ are respectively the longitudinal and transverse correlation length, and W is the averaged pinning force. The theory of elasticity of the vortex lattice in Type II superconductors was obtained by Brandt [26-31]. He has shown that in the theory of elasticity, nonlocal effects play an important role. He has estimated the dependence of elastic constants on the wave vector '$\boldsymbol{k}$'. The $\boldsymbol{k}$ dependence of the elastic modulii was derived from the following expression of the elastic free energy:

$$F_{el} = \frac{1}{2}\int \frac{d^3k}{(2\pi)^3} u_\alpha(\boldsymbol{k})\Phi_{\alpha\beta}(\boldsymbol{k})u_\beta(-\boldsymbol{k}) \text{ with } \alpha,\beta = \text{x,y,x,} \qquad (2.3.4.1)$$

Here $\Phi_{\alpha\beta}(\boldsymbol{k})$ is the elastic matrix of the vortex lattice and $u_\alpha(\boldsymbol{k})$ is the Fourier transform of displacement. Within the non-local continuum limit, the elastic matrix can be written as; $\Phi_{\alpha\beta}(\boldsymbol{k}) = [c_{11}(\boldsymbol{k}) - c_{66}]k_\alpha k_\beta + \delta_{\alpha,\beta}[c_{66}k_\perp^2 + c_{44}(\boldsymbol{k})k_z^2]$

with $k_\perp^2 = k_x^2 + k_y^2$. The moduli $c_{11}(\boldsymbol{k})$, $c_{44}(\boldsymbol{k})$ and $c_{66}(\boldsymbol{k})$ are temperature and field dependent. The shear modulus $c_{66}(\boldsymbol{k}) = \frac{\Phi_0 \boldsymbol{H}}{(8\pi\lambda_{ab})^2}(1-b_1)^2$, where $b_1 = H/H_{c2}$, with H_{c2} as the upper critical field and λ_{ab} as the penetration depth along the *ab*-plane. The shear modulus determines the stability of the flux lines within a single plane. For small fields, the shearing modulus can be used to determine the melting temperature T_m of the two dimensional (2D) vortex lattice of strongly anisotropic high T_c superconductors

($c_{66}(k) = 0$ indicates the vortex liquid phase). The tilt modulus $c_{44}(\boldsymbol{k}) = \frac{H^2}{4\pi}\frac{1}{\left(1+k_\perp^2\lambda_c^2+k_z^2\lambda_{ab}^2\right)}+\frac{H\Phi_0}{32\pi^2\lambda_c^2}\ln\bar{k}$ where $\bar{k}=\frac{1+\varepsilon^2\kappa^2+\lambda_{ab}^2k_z^2}{1+b_1\varepsilon^2\kappa^2+\lambda_{ab}^2k_z^2}$, λ_c is the penetration depth along c axis, $\varepsilon=\lambda_c/\lambda_{ab}$ and κ = Ginzburg-Landau parameter. The tilt modulus, for small fields, depends strongly on the anisotropic axis of high T_c superconductors. For example, an estimate of the Josephson and magnetic coupling field contributions to the interlayer coupling of a high T_c superconductor at low temperature can be obtained from $c_{44}(\boldsymbol{k})$ for small fields (a straight vortex line has no Josephson coupling) [32]. The compression modulus $c_{11}(\boldsymbol{k})=\frac{H^2}{4\pi}\frac{1+k^2\lambda_c^2}{(1+k^2\lambda_{ab}^2)(1+k_\perp^2\lambda_c^2+k_z^2\lambda_{ab}^2)}$ originates from vortex-vortex interaction.

2.3.5 Lawrence and Doniach Model

For strongly anisotropic HTS materials like Bi2212, the flux line lattice is two-dimensional over a wide range of the *H-T* phase diagram. In order to describe the 2D flux line lattice, Lawrence and Doniach (L-D) have proposed a model based on the modified version of Ginzburg-Landau theory [15]. The L-D model describes 2D superconducting layers which, depending on spacing, field and temperature, may couple to one another through the Josephson current. In this model, the thickness of the superconducting layer d is comparable to the coherence length $\xi(T)$, leading to a homogenous current J_s (Josephson current) and field distribution in the z-direction within layers.

The GL free energy has been modified in two aspects:

(a) The effective mass in this model is m* = 2m, M* = 2M for the electron moving parallel and perpendicular to the plane respectively.

(b) The order parameter $\Psi(r)$ with coordinates r = (ρ,z) in GL theory is replaced by $\Psi_n(\rho) = |\Psi_n(\rho)|\exp[i\varphi_n(\rho)]$, where n is the number of superconducting layers. The kinetic energy term $|\nabla_z \Psi|^2$ is also described in the form $d\Psi/dz \approx 1/d(\Psi_{n+1} - \Psi_n)$.

One of the interesting results in this modified G-L model is that it gives an understanding of Josephson intercoupling of the vortices by the Josephson current obtained as $J_z(\rho,z_n) \approx J_{co}\sin(\varphi_{n+1} - \varphi_n)$, where J_{co} is the critical Josephson current density.

2.2 Vortex Pinning in High T_c Superconductors

2.4.1 Intrinsic Pinning Barrier

The High Tc Superconductors (HTS) have strong anisotropic layered crystal structures with two-dimensional conducting CuO_2 planes. In Bi2212 single crystals, the CuO_2 planes are separated by insulating layers of thickness d = 15 Å. Bi2212 single crystals have the mass anisotropy parameter $\varepsilon = m_i / M \sim 1/50 - 1/100$. Here m_i is the effective mass along the a or b axis of the crystal and M is the effective mass along the z axis of the crystals. In HTS-oxide superconductors, strong superconductivity resides in the CuO_2 planes and only weak or vanishing superconductivity resides in between these planes [15]. The vanishing superconductivity in between the CuO_2 planes implies that the superconducting order parameters may be sufficiently depressed between the planes so as to act as pinning centers for vortices. Such pinning induced by the crystal structure of these materials leads to the term "intrinsic pinning" [33]. The intrinsic pinning appears only for the magnetic fields applied parallel to the *ab*-plane. In this situation, vortex cores lie in between the strongly superconducting CuO_2 planes. With a current density j applied parallel to the *ab*-plane and perpendicular to H, the vortices try to move in a perpendicular direction to the *ab*-plane due to a Lorentz force. However, the motion of the vortices in this direction is prevented due to the strongly superconducting CuO_2 layers. This is because the normal vortex cores have to overcome a large condensation energy as they cross the CuO_2 layers, and therefore, they are pinned between the layers. The intrinsic pinning of the vortices can be considered to have a profound influence on the critical current density. The concept of intrinsic pinning has been extended to describe the notion of a "lock-in transition [15,34,35]. The idea of the lock-in transition is that for low and intermediate fields, the vortex lattice can maintain

its minimum energy by aligning itself with the superconducting planes, thereby creating a pure lattice of Josephson vortices so as to take advantage of the intrinsic pinning between the CuO_2 planes.

2.4.2 Surface and Geometrical Barrier Pinning

The surface of the sample can be considered as a pinning site since there is an energy barrier for flux to enter or exit the sample [36-41]. This barrier is called the Bean-Livingston (BL) surface barrier. The BL surface barrier arises as a balance between two forces, one is a vortex image force that attracts a vortex towards the surface of the sample, and the other is a Lorentz force from the Meissner shielding currents that drives vortices inside the sample [41]. Therefore, the surface barrier is defined by the surface of the sample. The BL surface barrier is observed at high temperatures, *i. e.* just below T_c, where other pinning mechanisms are relatively inoperative.

A geometrical barrier arises from a competition between the elongation energy of a vortex penetrating into the sample through the corners of the sample and the Lorentz force [41-45]. The geometrical barrier is determined by the shape of the sample. In platelet shaped Bi2212 single crystals, a pronounced geometrical barrier has been observed to dominate at low field and high temperature [42]. However, prism shaped and semi-ellipsoidal-shaped crystals are observed to have larger geometrical barrier effects than platelet shaped crystals at lower temperatures [42].

2.4.3 Core Pinning: δT_c and δl Pinning

The most common type of pinning is called core pinning. In core pinning, a vortex line can be pinned as a result of an inhomogeneity in the superconducting material by a

variation in the core energy of the vortex. The energy per unit length associated with the vortex line having a cylindrically shaped normal core is $E_{core} = (H_c^2 \pi \xi^2) / 8\mu_0$, where the thermodynamic critical field $H_c = \Phi_0 / (2\sqrt{2}\pi \xi \lambda_L)$ [46,47]. If the normal region in the superconducting material is described as a spherical cavity of radius r_a ($r_a > \xi$), then the maximum pinning force associated with this cavity is [46]:

$$f_{pin}^{core} = -\frac{H_c^2 \xi^2}{4\sqrt{2}} \sqrt{\frac{r_a}{\xi}} \qquad (2.4.3.1)$$

Two types of vortex core pinning are reported: (1) δT_c pinning and (2) δl pinning. The δT_c pinning is caused by local variations in the superconducting order parameter due to regions with depressed T_c [15]. The δl pinning arises from local variations in the superconducting length scales λ_L and ξ, resulting in fluctuation in the G-L parameter k [15].

2.4.4 Magnetic Pinning

A vortex line can be pinned as a result of a change in its magnetic energy. The magnetic energy per unit length of the vortex line is $E_{mag} = (H_c^2 4\pi \xi^2 \ln k) / 8\mu_0$. The pinning centers consisting of normal inclusions or vortices in the superconducting materials change the magnetic energy due to a variation in the redistribution of supercurrent circulating about the vortex core and associated magnetic field [46,47]. The maximum pinning force for a cylindrical cavity of radius r_a in a superconductor is

$$f_{pin}^{mag} = -\frac{H_c^2 \pi \xi^2}{\lambda_L^2} \sqrt{\frac{r_a}{\xi}} \qquad (2.4.4.1)$$

2.5. Introduction of Pinning Centers in High T_c Superconductors

2.5.1. Pinning by Irradiation Induced Defects

Irradiation produces two types of pinning centers: point disorders and correlated defects. Point disorders are usually produced by electron or neutron irradiation, and correlated defects (such as columnar defects) are produced by heavy ion irradiation [48-51]. Proton irradiation produces randomly oriented tracks [52]. The effects of irradiation on flux pinning have been investigated for a variety of high T_c superconducting materials such as Y123, Bi2212, Bi2223, Hg1223 and Tl1223 [48-50,54-57]. The flux pinning depends upon the size of the defects introduced by irradiation and also on the irradiation dose (i. e. number of defects per cm^3). In Bi2212 single crystals, a number of papers have reported improved flux pinning after irradiation [48,49,51-55]. A significant enhancement in the critical current density and irreversibility field has been observed in Bi2212 single crystal after heavy ion irradiation [55,56]. This improvement is reported to arise from a better correlation between pancake vortices pinned along a columnar defect [50,57]. The pinning of the pancake vortices by columnar defects in Bi2212 single crystals is shown in Fig. 2.5.1. The figure shows a columnar track of diameter ~ 2R (comparable to the diameter of the vortex core ~ 2ξ). The vortices along the track are strongly pinned due to the core pinning mechanism (see section 2.4.3). Here vortices are pinned as a result of the variation in the core energy of the vortices at the boundary of the non superconducting track.

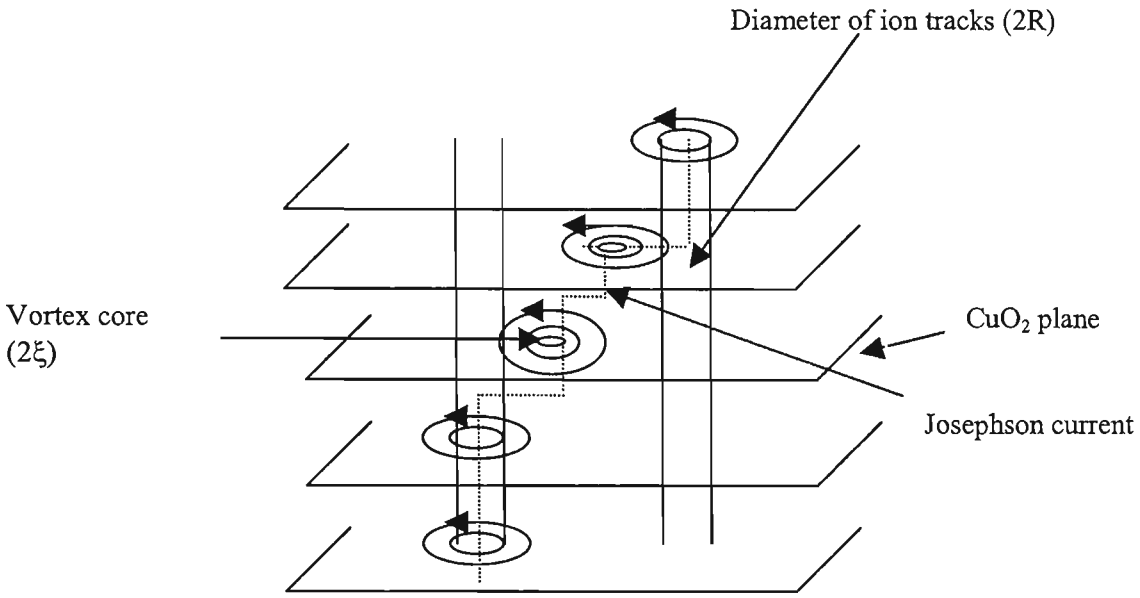

Fig. 2.5.1: Schematic view of the vortex pinning on an ion track crossing the CuO_2 planes [ref.15].

A further improved flux pinning in Bi2212 single crystals has been reported with columnar defects tilted from the *c*-axis [56]. The enhancement is explained by an increase in the individual pinning energy resulting from the larger damaged area in the *ab*-plane. In this case, the vortices are pinned by the large normal core present in the *ab*-plane as a result of the tilting of columnar defects.

2.5.2. Pinning by Atomic Doping Induced Defects

One of the purposes of atomic doping in Bi2212 single crystal is to create effective pinning centers to pin vortex lines and improve the critical current density (J_c). Light lead doping in the Bi-based superconductors plays a very important role in the phase formation mechanism [58]. With Pb doping the desired superconducting compounds (such as Bi2223), are stabilized, inter-growth defects are reduced, and electrical

conductivity between the grains is increased. A large enhancement in vortex pinning has been reported with heavy Pb doping in Bi2212 single crystals, [59-65]. The critical current density and irreversibility fields are reported to be much higher in heavily Pb doped Bi2212 single crystals than in Pb free Bi2212 single crystals [59,60,63]. The critical current density and irreversibility field depend upon the Pb concentration in $Bi_{2.2-x}Pb_xSr_{1.8}CaCu_2O_{8+\delta}$. Single crystals with x = 0.6 have a larger critical current density and irreversibility field than for x = 0.4 [59,60,63]. Scanning Tunneling Microscopy (STM) has shown two microstructures: Pb-poor (α-phase) and Pb-rich (β-phase) in heavily Pb-doped Bi2212 single crystal [62]. The thickness of the alternating lamellar plates of each phase amounts to about two tens of nanometers. The structural modulation with Pb doping is reported only for the α-phase [62]. Further improvement in vortex pinning has been reported in heavily Pb-doped single crystals after irradiation [63]. The resistivity anisotropy ($\gamma^2 \equiv \rho_c/\rho_{ab} = \rho_c / (\rho_a \rho_b)^{1/2}$) is observed to decrease dramatically in Bi2212 single crystals with Pb doping [64]. For doping level x = 0.6, $\gamma^2 = 1.2 \times 10^3$, whereas in Pb free oxygen overdoped Bi2212 crystal $\gamma^2 = 8.5 \times 10^3$.

The resistivity anisotropy is obtained using the relation $\gamma^2 = \rho_c / \rho_{ab}$. The in-plane resistivity (ρ_{ab}) as a function of temperature in the sample was measured by using a standard *dc*-four probe technique. Electrical contacts of less than 2Ω resistance were established by attaching the gold wires to the evaporated -silver stripes onto the sample with silver epoxy. The out of plane resistivity ρ_c of the sample was measured using a dc four probe method with current electrodes consisting of angular rings. The voltage V_c across the sample was measured by applying the current from the top to the bottom of the sample through the angular rings [64].

The mass anisotropy parameter, $\gamma_m^2 = {}^{m_c}/_{m_{ab}}$, can be obtained using torque magnetization measurements. The torque sensor (cantilever) was used for the detection of magnetic torque $\vec{\tau} = \vec{m} \times \vec{B}$ arising from a transverse component of the magnetization $\vec{m}$ of the sample. From the symmetry of the torque with respect to the angle θ between the field and *ab*-plane, the orientation of the sample *ab*-plane with respect to the magnetic field with an accuracy better than 0.05° can be estimated. The torque shows a maximum for a small angle ($\theta = \theta_p < 2.4^\circ$) and becomes zero for an applied field parallel to *ab*-plane ($\theta = 0^\circ$). The torque decreases for $\theta > \theta_p$ and becomes again zero for $\theta = 90^\circ$. The angular dependence of the reversible torque $\tau(\theta)$ of an anisotropic superconductor with volume V is given by [65]

$$\tau(\theta) = \frac{\Phi_0 VH}{16\pi\mu_0\lambda_{ab}^2}\frac{\gamma_m^2 - 1}{\gamma_m}\frac{\sin 2\theta}{\varepsilon(\theta)}\ln\frac{\gamma\eta H_{c2}}{H\varepsilon(\theta)} \qquad (2.5.2.1)$$

where $\varepsilon(\theta) = \sqrt{\gamma_m^2 \sin^2(\theta) + \cos^2(\theta)}$ is the angular scaling function, μ_0 is the vacuum permeability, H_{c2} is the upper critical field and the parameter η is of the order of unity.

For a fixed applied field $H > H_{\text{IIT}}$, the normalized torque $\tau_{norm} = \tau(\theta) / \tau(\theta_p)$ depends only on γ_m and H_{c2} [65]. For a highly anisotropic superconductor, the angle θ_p depends very sharply on γ_m and only weakly on H_{c2} [65]. Therefore measuring θ_p, one obtains γ_m as $\gamma_m \cong 1/\theta_p$ [65].

Iron doping has also been used for the creation of point defects in Bi2212 single crystals [66-69]. Iron, being a 3d element, replaces Cu atoms in the CuO_2 planes. The critical temperature is reported to be strongly reduced with increasing Fe-doping. This reduction is explained in terms of the pair breaking scattering mechanism introduced by magnetic impurities in the CuO_2 planes [67,70]. In other words, the superconducting order parameter is suppressed with Fe-doping. The London penetration depth (λ_L) is reported to be increased with increasing Fe concentration whereas the coherence length (ξ) is reported to decrease [67]. The G-L parameter (κ) is found to increase strongly upon doping. The decrease in the coherence length (ξ) with doping has been employed to explain the decrease of the critical current density and the irreversibility line [67].

Oxygen over-doped Bi2212 single crystals have larger critical current densities than under-doped or optimally doped crystals [65]. This suggests that the excess oxygen content in the crystal enhances the flux pinning process [65, 71-73]. The out-of-plane resistivity (ρ_c) in Bi2212 single crystals is strongly influenced by the oxygen content in the crystals. In the oxygen under-doped regime, the c axis resistivity has non -metallic temperature dependence whereas in the over-doped regime the crystal shows a metallic behaviour [73]. In oxygen over-doped crystals, the excess oxygen has been suggested to distort the CuO_2 layers [71]. Distortion of the CuO_2 layers can behave as pinning centers since the coherence length is close to the atomic scale in HTSC.

2.5.3 Pinning by Dislocations

Dislocations present in the BSCCO system can act as strong pinning centers for the vortices. The order parameters are suppressed in the dislocation, creating the pinning

centers. In the Bi2212 single crystals, dislocations such as stacking faults originate as a consequence of accommodation of lattice mismatch. In Bi2212 single crystals, stacking faults are proposed as effective pinning centers for 2D pancake vortices [74]. The screw dislocation densities associated with spiral growth in Bi2212 single crystals are also reported to improve vortex pinning [75]. In B2223 tapes, dislocations such as micro- and nano-cracks are introduced by mechanical deformation [76]. These cracks remain unhealed even after prolonged sintering. The imperfect by healed micro- and nano-cracks are suggested to aid in enhancing flux pinning in Bi2223 tapes [76].

2.6 Critical State Model

In the critical state model, the critical current density is defined as the transport current density at which the Lorentz force (F_L) on the vortices is in equilibrium with the pinning force (F_p).This model was first introduced by Bean (1962), without taking into account thermal excitations [77-78]. For a finite temperature, the Bean critical state model was modified by Anderson and Kim in 1964 [79,80]. Here we will present both of these two models.

2.6.1 Bean Critical State Model

The Bean critical state model is a local electrodynamic model and it describes an irreversible magnetic process in Type II superconductors. The basic premise of this model is that in a Type II superconductor with homogenously distributed defects, the irreversible magnetization $\boldsymbol{M}_{irr}$ is related to the critical current density $\boldsymbol{J}_c$ through a modified Ampere's law $\nabla \times \boldsymbol{B} = \left(\frac{4\pi}{c}\right)\boldsymbol{J}_c$, where $\boldsymbol{B}$ is the magnetic induction inside the superconductor. Here the gradient in $\boldsymbol{B}$ (or $\nabla \times \boldsymbol{B}$) is determined by flux pinning. Bean critical state model makes the assumption that the flux distribution is linear in a superconductor, (see Fig. 2.6.1). The gradient of B is associated with a single value of the critical current density. For a flux density profile in a completely penetrated sample, the local and average values of the critical current density are precisely equal. Upon application of the magnetic field $\boldsymbol{H}$, flux enters the sample from the surface of the superconductor with its gradient constant and equal to $\boldsymbol{J}_c$. As the field increases, the field penetration also increases (Fig.2.6.1.). The value of external field at which the field fully penetrates the sample is called the full penetration field $\boldsymbol{H}^*$. For a slab of half-

width d, it is given by: $H^* = (2\pi J_c d)/c$ [77]. The Bean model predicts hysteretic magnetic response and remanent magnetization for $H = 0$.

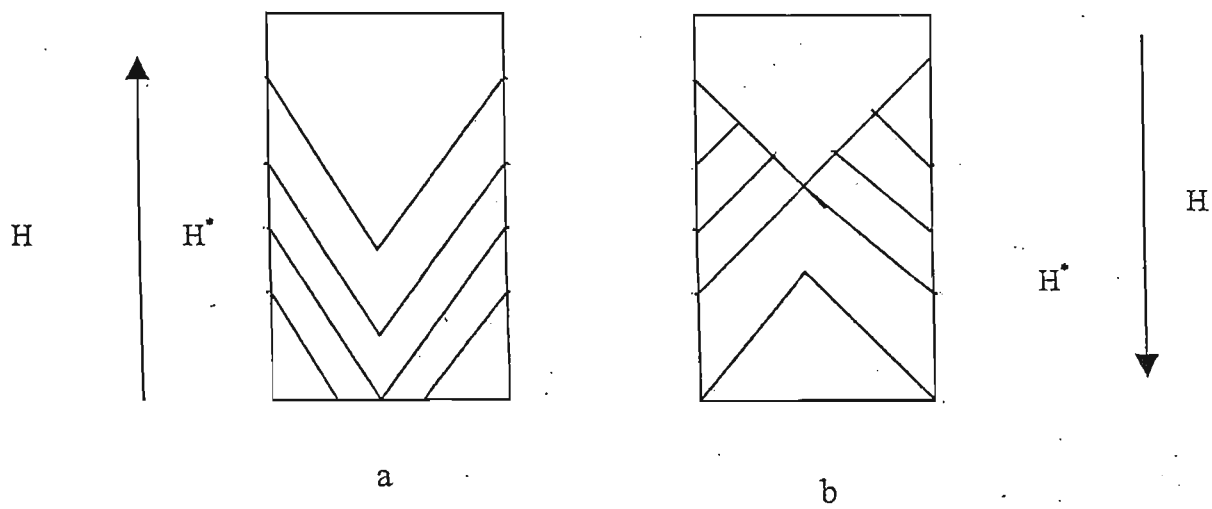

Fig. 2.6.1: Bean model flux profiles for (a) increasing fields and (b) decreasing fields.

For a slab of thickness d, $J_c = \frac{20\Delta M}{d}$ (H // slab surface), where ΔM is the height of the magnetic hysteresis loop.

For a cylinder of radius R, $J_c = \frac{15\Delta M}{R}$ (H // c axis)

The Bean model has been employed to obtain critical current densities of HTSC materials [81]. The critical current density for a flat plate sample with an applied field along c-axis and shielding currents in the ab plane is defined as $J_c = \frac{20\Delta M}{a(1-a/3b)}$, where a and b are the lateral dimensions of the slab.

2.6.2 Anderson and Kim Model

The Anderson and Kim model was the first to describe the phenomenology of thermally activated flux motion over pinning barriers in Type II superconductors. As we discussed earlier, in the critical state model at $T = 0$, the fluxoids in the bulk of a Type II superconductor can move only if the Lorentz force F_L acting on the fluxoids exceeds the maximum pinning force F_P. However, Anderson and Kim suggested that at temperatures greater than zero, fluxoids can move with the help of thermal activation over a potential barrier U, even if the Lorentz force F_L is smaller than the pinning force F_P [79]. The motion of the fluxoids with the thermal activation is called flux creep (classical flux creep).

The Bean critical state model assumes a B-independent critical current density J_c. The Bean critical state model also disregards spatial variation in the vortex density B (r). However, the Anderson - Kim critical state model takes into account spatial variation in the vortex density. Thus, this model considers a functional form for $J_c(B(r))$, which arises from a spatial variation in the vortex density. Expressions for $J_c(B(r))$ have been presented in [82,83]. A typical flux profile for the Anderson and Kim model is shown in the Fig.2.6.2.

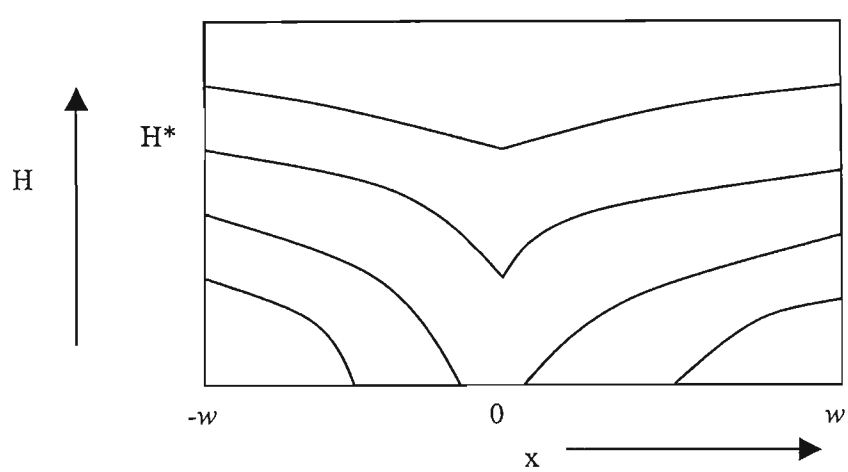

Fig. 2.6.2: An illustration of the Anderson-Kim flux profile for an increasing field [refs.82, 83].

2.7 Models for Vortex Pinning in High T_c Superconductors

2.7.1 Collective Pinning Model

In the collective pinning model, each vortex line is pinned by many randomly distributed pinning centers such as oxygen vacancies. For perfectly rigid vortex lines and randomly distributed pinning centers, the pinning force F_p would be zero. However, vortex lines can be distorted as they meander from one pinning center to another and the net pinning force is not zero. The concept of collective pinning can be applied in the case of weak pinning where the local displacement of the vortices is smaller than lattice constant. In Type II superconductors, it has been suggested that the long range order of the vortex lattice can be destroyed in the presence of weak pinning centers [84]. The vortices can retain their periodicity within a correlated volume, V_c. For a current density 'J' less then the critical current density 'J_c'in the superconductor, the correlated regions are displaced due to the Lorentz force F_L for a distance less than the scale of the random pinning potentials. The resulting volume pinning force then acts to balance the Lorentz force. The expression for the volume pinning force is given as $F_p = f_p(n/V_c)^{1/2}$, where f_p is the force exerted by an individual pinning center on the vortex lattice, n is the number of the pinning centers in the volume V_c.

In HTSC materials, the collective pinning model has been used to study magnetic relaxation [85-89]. The basic mechanism for magnetic relaxation is that a configuration of vortices is in a non-equilibrium state because of the flux pinning, and it will try to relax to a state with a minimum energy. This relaxation process will lead to a redistribution of currents in the superconductor and hence to a change in the magnetic moment with time. The measured magnetic relaxation can also be thought of as being caused by the spontaneous motion of magnetic vortices out of their pinning centers.

Such motion usually arises from thermal fluctuations and quantum fluctuations (at very low temperature) over the activation energy barrier. Magnetic relaxation in high T_c superconductors (HTSC) has been the subject of intensive experimental studies because it helps us to understand the physical properties of HTSC such as the magnetic phase diagram, pinning mechanisms and thermodynamic properties [87-89]. From the technical point of view, it is also used to calculate the limits to the stability of high T_c superconductor devices, such as persistent mode magnets, since it determines the temperature and time dependence of the current density [87,89].

The phenomenon of magnetic relaxation was first described by P.W. Anderson in 1964 to explain Kim's experimental relaxation data (1994) [79,80]. He proposed a thermally activated flux creep model to explain the relaxation phenomenon. According to the Arrhenius relation, the hopping time of the flux lines is given in terms of the potential energy barrier height $U(J)$:

$$t = t_0 \exp\left(-\frac{U(J)}{k_B T}\right) \qquad (2.7.1.1)$$

where t_0 is the effective hopping time of the flux line and k_B is the Boltzmann constant:

The hopping process is supported by a driving force; $\boldsymbol{F_L} = (1/c)\, \boldsymbol{J} \times \mathbf{H}$. Therefore, U must be a decreasing function of J:

$$U = U_0\left[1-\frac{J}{J_{c0}}\right] \qquad (2.7.1.2)$$

where U_0 is the barrier height in the absence of the driving force, and J_{c0} is the critical current density in absence of thermal activation. Using equations (2.7.1.1) and (2.7.1.2), we obtain the Anderson classical flux creep equation, which is logarithmic with time

$$J = J_{c0}\left[1-\frac{k_B T}{U_0}\ln\left(\frac{t}{t_0}\right)\right] \qquad (2.7.1.3)$$

Beasley et al. in 1969, while elucidating experimentally the mechanism of Anderson's proposed thermally activated flux-creep process, observed a non-linear *U-j* relationship leading to a non-logarithmic decay of magnetization [90].

Beasley et al. summarized their research work as follows:

1. A logarithmic time dependence of the creep process prevails in the critical state, due to exhaustion of the excess driving force over the pinning barrier. The linear approximation $U = U_0 - F_L VX$ made by Anderson and Kim is justified in the limit $k_B T << U$, where V is the volume of the flux bundle and X is the pinning length.

2. A non-logarithmic time dependence of the creep process prevails in the sub-critical state. They further suggested that, on departing from the critical state to the subcritical state, the creep rate becomes exponential by decreasing temperature and applied field. When the thermal activation takes place near the top of an energy barrier, U becomes a non-linear function of F_L ($\sim \nabla H$), and therefore the parameters U_0 and VX used by Anderson-Kim are not trivially related to the height and width of the activation barrier.

Fig.2.7.1 shows that the apparent value of the effective activation barrier $U_{eff}(J)$ is always smaller than the true pinning potential U_0. The value of $U_{eff}(J)$ strongly varies with J since it depends upon the curvature of $U(J)$.

The full impact of the non-linear $U(J)$ dependence has become apparent only after the development of vortex glass theory by Fisher [91-93] and collective pinning theory by Feigel'mann [15,85,86]. In these theories, the pinning barrier diverges as the current J approaches zero.

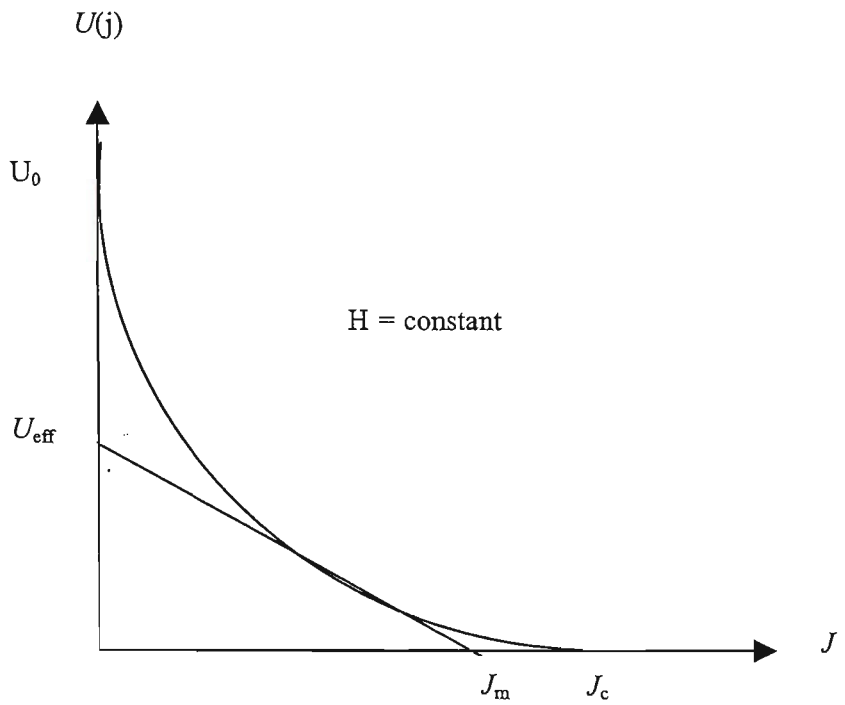

Fig. 2.7.1: A schematic illustration of a nonlinear functional form of $U(J)$ at a constant magnetic field H. The linear approximation defined by $U = U_0 [\ 1 - J/J_{c0}\ ]$ is used to obtain the effective pinning potential $U_{eff}(J)$ which is smaller than the true potential U_0 ($J = 0$). Here J_c is the critical current density and J_m is the current density corresponding to $U_{eff}(J)$ [ref.87].

Feigel'mann, in his collective pinning theory, showed that at an applied current $J \rightarrow 0$, the activation barrier $U(J)$ between different metastable states grows with a power law

$$U(J) = U_0\left(\frac{J_c}{J}\right)^{\alpha} \qquad (2.7.1.4)$$

where U_0 is the characteristic energy scale and the exponent α depends on the dimensionality and on the particular regime of the flux creep. In the three dimensional case, $\alpha = 1/7$ in the weak field, low temperature regime where creep is dominated by the motion of the individual flux lines. For $\alpha = 3/2$, the collective creep of small vortex bundles takes place (at higher fields) and for $\alpha = 7/9$, the collective creep of large bundles takes place (at very large fields). For the two dimensional collective creep process, $\alpha = 9/8$.

If current relaxation is due to a thermal activation process, then Geshkenbein proposed a relation for the activation barrier U_α and the persistent current $J(t)$ given by [94]:

$$U_\alpha(J) = T \ln\left(\frac{t}{t_0}\right) \tag{2.7.1.5}$$

where t_0 is the attempt time.

Using equations (2.7.1.4) and (2.7.1.5), a relation for the current relaxation law has been obtained:

$$J(t) = J_c\left[\left(\frac{U_0}{k_B T}\right)\ln\left(\frac{t}{t_0}\right)\right]^{-1/\alpha} \tag{2.7.1.6}$$

A classical theory for the flux creep can also be developed by using the Maxwell electrodynamic equation [15]. The second Maxwell's equation gives:

$$\nabla \times \boldsymbol{B} = \frac{4\pi}{c}\boldsymbol{J} \tag{2.7.1.7}$$

where $\boldsymbol{B}$ is the magnetic induction and $\boldsymbol{J}$ is the transport current density.

Using equation (2.1.1.7), the decay of the current density is also obtained from the forth Maxwell equation:

$$\nabla \times \boldsymbol{E} = -\frac{1}{c}\frac{d\boldsymbol{B}}{dt} \tag{2.7.1.8}$$

where $\boldsymbol{E}$ is the electric field and c is the velocity of light.

The gradient of the field (vortex density) defined by a relation $\nabla \times \boldsymbol{B} = (4\pi / c)\boldsymbol{J}$ induces a driving force so that the vortex motion is set up. The electric field $\boldsymbol{E}$ (i. e dissipation) generated by the vortex motion is given by $\boldsymbol{E} = \frac{1}{c}\boldsymbol{B} \times \boldsymbol{v}''$, where $\boldsymbol{v}''$ is the velocity of the vortices. With a magnetic field B parallel to the z-axis and electric field E parallel to the y-axis (or current J parallel to the y-axis), the relation for E becomes (for the vortices moving along the x-axis):

$$\mathrm{E}_y = \frac{1}{c} B_x v''_x = \frac{1}{c} B v'' \qquad (2.7.1.9)$$

Substituting (2.7.1.9) in (2.7.1.8), we get

$$\frac{d\Phi}{dt} = \frac{d}{dx}(v'' B) \qquad (2.7.1.10)$$

With equation (2.7.1.7), the equation (2.7.1.10) becomes

$$\frac{dJ}{dt} = \frac{c}{4\pi}\frac{d^2}{dx^2}(v'' B) \qquad (2.7.1.11)$$

Assuming thermal activation over the pinning barrier, the velocity $\boldsymbol{v}''$ associated with the flux bundles is given by [79]:

$$v'' = v''_0 \exp[-U(J)/k_B T] \qquad (2.7.1.12)$$

Substituting the value of v'' in equation (2.7.1.11), we have

$$\frac{dJ}{dt} \approx \frac{J_c}{\tau_0} e^{U(J)/k_B T} \text{ where } t_0 = \frac{k_B T \tau_0}{J_c |dU/dJ|} \text{ is the attempt time.}$$

The above equation can be solved with logarithmic accuracy (Geshkenbein and Larkin) [94].

$$U[J(t)] \cong k_B T \ln\left[1+\frac{t}{t_0}\right] \qquad (2.7.1.13)$$

As described earlier in the Anderson and Kim model, the thermally activated motion will be strongly assisted by the Lorentz force (i.e current density), so that the activation energy should be a decreasing function of the current density.

To account for the fact that U is a decreasing function of the Lorentz force, U is defined as

$$U(J) \cong U_c\left[1-\frac{J}{J_c}\right]^{\mu} \qquad (2.7.1.14)$$

with a condition that for $J = J_c$ the activation energy should vanish.

Now, substituting (2.7.1.14) into (2.7.1.13) , we get

$$J(t) = J_c\left[1-\left\{\frac{k_B T}{U_c}\ln\left(1+\frac{t}{t_0}\right)\right\}\right]^{1/\mu} \qquad J \to J_c \qquad (2.7.1.15)$$

For $\mu = 1$, the above equation gives the Anderson and Kim relation. This relation is very good for conventional Type II superconductors, where $J \to J_c$. However, in high T_c superconductors where $J << J_c$ is already reached in laboratory times, the collective pinning theory and vortex glass theory predict an activation barrier that should diverge as $J \to 0$:

$$U(J) \cong U_c\left[\frac{J}{J_c}\right]^{-1/\mu} \qquad (2.7.1.16)$$

Inserting equation (2.7.1.16) into equation (2.7.1.13), we obtain a non-purely-logarithmic time dependent current density.

$$J(t) = J_c\left[\frac{k_B T}{U_c}\ln\left(\frac{t}{t_0}\right)\right]^{-1/\mu} \qquad J << J_c \qquad (2.7.1.17)$$

Equations (2.7.1.15) and (2.7.1.17) can be combined in one to obtain an interpolation formula.

$$J(t) = J_c\left[1+\left\{\frac{\mu k_B T}{U_c}\ln\left(1+\frac{t}{t_0}\right)\right\}\right]^{1/\mu} \text{ where } \mu=1 \qquad (2.7.1.18)$$

and the activation barrier is defined as

$$U(J) \cong \frac{U_c}{\mu}\left[\left(\frac{J_c}{J}\right)^{\mu} - 1\right] \qquad (2.7.1.19)$$

For the single vortex pinning regime, the exponent $1/\mu$ becomes 7, such that for $\left(\mu k_B T/U_c\right)\ln\left(1+t/t_0\right) << 1$ the interpolation formula (2.7.1.18) for the current density becomes

$$J(t) = J_c\left(1+t/t_0\right)^{-k_B T/U_c} \qquad (2.7.1.20)$$

The activation barrier is reduced to:

$$U(J) = U_c \ln\left[J_c/J\right] \qquad (2.7.1.21)$$

Here $U(J)$ is a logarithmic potential.

2.7.2 Pinning Regimes in Strongly Layered High T_c Superconductors

For high anisotropy materials (such as Bi2212 materials), depending upon the applied field and pinning strength γ_p, the collectively pinned vortices can take any pinning regimes from the zero-dimensional pancake vortex pinning regime to the 3-dimensional vortex pinning regimes [15, 95]. In the zero dimensional pinning regimes the vortices are individually pinned. This is because the interplanar interaction energy between the pancake vortices is smaller than the pinning energy, $U_{pc} \approx \varepsilon_0 s (J_c / J)$ of the individual pancake vortices and also because the collective pinning length along the c axis, $L_c \approx (\varepsilon^4 \xi^2 \varepsilon_0^2 / \gamma_p)^{1/2}$, of the pancake vortices is smaller than the inter-layer distance s. Here 'ε_0' is the energy of the isolated vortices and ε is the mass anisotropy factor. In Bi2212 single crystals $U_{pc} = 20$K. The zero-dimensional pinning regime in Bi2212 single crystal is observed below 20K [95]. For a weak magnetic field H and pinning strength γ_p such that $L_c < \varepsilon a$ and $L_c > s$, the collectively pinned object is a vortex line. Here a is the lattice constant and s is the distance between two CuO_2 planes. If we neglect the interaction between vortex lines, the vortices are said to be in the one-dimensional pinning regime. In Bi2212 single crystals, the 1D pinning regime has been observed and reported to lie between 20K and 40K [95]. With an increased magnetic field such that $L_c > \varepsilon a$, the collectively pinned vortices are described by the 3D pinning regime. With further increases in the magnetic field H such that $a < \xi (s\varepsilon_0 / U_{pc})^{1/2}$ and $L_c < s$, the 2D pinning regime appears. In this case, all the neighboring pancake vortices are within the collective pinning radius (R_c) from each other. Qualitative low-field phase diagram of the vortex states in Bi2212 for magnetic field H perpendicular to the superconducting layers is given in Fig. 2.7.2.1.

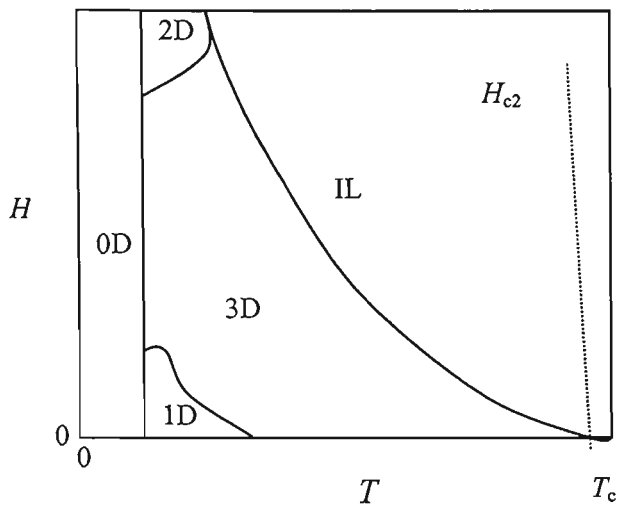

Fig.2.7.2.1: A qualitative low-field phase diagram of the vortex states in Bi2212 single crystal for the applied field perpendicular to the CuO_2 plane. Here, IL is the irreversibility line [ref.95].

2.7.3 The Vortex Glass Model

The vortex glass model investigates the effect of disorder introduced by randomly distributed point defects on the vortex matter [15, 91-93,96]. The vortex glass model predicts a glass transition temperature T_g (H), below which the vortices freeze into the vortex glass phase, which is a resistive state in the absence of thermal activation ($T = 0$ K). Above T_g the flux flow state is associated with a vortex liquid for which the resistivity approaches the normal (ohmic) state value. The evidence of such a glass transition has been observed in the scaling behaviour of E (J) characteristic. The introduced disorder leads to pinning of vortex lines and therefore produces a highly non-linear E (J). This non-linear behaviour of the vortex system has been considered in the study of the vortex glass phase as a function of temperature and magnetic field.

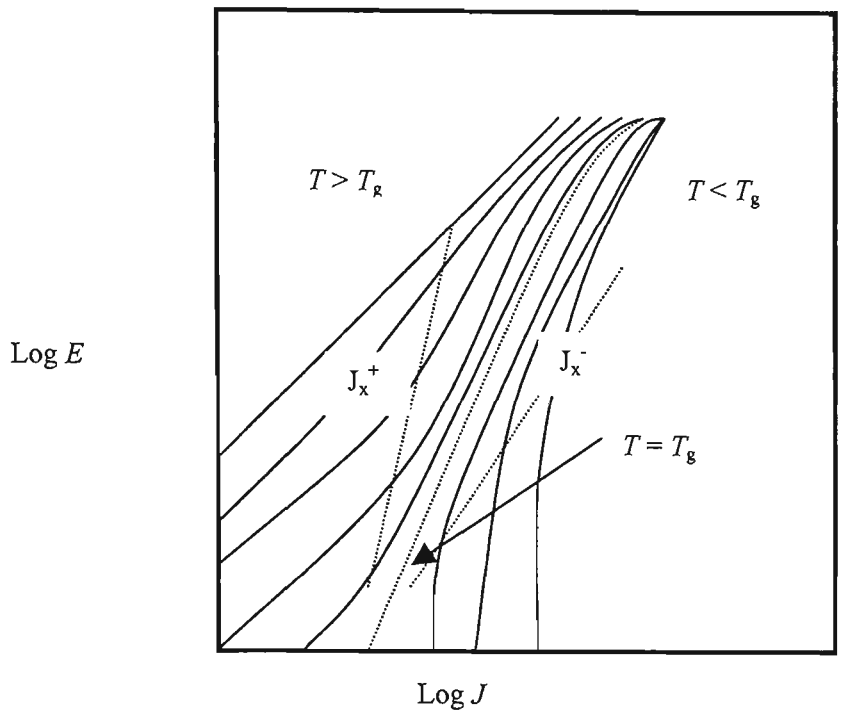

Fig. 2.7.3.1: Current-voltage characteristic of high T_c superconductors [ref.15].

The relationship between the voltage and the current density in the vortex glass state ($T < T_g$) has been predicted to be $E(J) \propto \exp(-J/J_c)^{-\mu}$,with exponent $0 < \mu < 1$. Above the transition ($T > T_g$), the system is in a liquid phase, has no translational order and exhibits a linear resistive E (J) characteristic. Scaling laws for the resistive transition in the vortex glass model predict that the behaviour above and below the glass transition temperature can be scaled to universal curves. The scaling laws are of the form: $E/J \propto (T_g - T)^{\upsilon(d-1)}$, where $J \propto (T_g - T)^{2\upsilon}$. For a 3D transition, it is expected that $d > 4$ and $1 < \nu < 2$. Above T_g, there is a transition from ohmic behavior, with $\rho(T) \propto (T - T_g)^{\nu(z+2-d)}$ at small current densities ($J < J_x^+$) to power law behaviour at large current densities ($J > J_x^+$). The crossover between the low-current regime and the power-law regime occurs around current density J^- for $T < T_g$ and J^+ for $T > T_g$ [15]. The

crossover current vanishes according to $J^{+} \propto \left(T - T_g\right)^{2\upsilon}$ at $T = T_g$. Below T_g, the crossover between small and large current density regimes separated by J_x^{-} changes the glassy behavior $E \propto exp[-c(J_c/J)^{\mu}$ at small current densities to a power law behavior at large current densities. The crossover current again vanishes according to $J^{-} \propto \left(T_g - T\right)^{2\upsilon}$ at $T = T_g$. The first experimental evidence of a continuous transition into a vortex glass phase was performed by Koch, who carried out experiments on YBCO films [91,92]. The exponents were $\nu \approx 1.7$ and $d \approx 4.8$ for YBCO films. The plot shown in Fig. 2.7.3.1 gives all the relevant information on the dynamic response of a vortex glass phase.

2.7.4 The Normalized Relaxation Rate

The normalized relaxation rate is obtained from the following relation:

$$S \equiv \frac{1}{M_{irr}} \frac{dM_{irr}}{d\ln t} = \frac{d\ln M_{irr}}{d\ln t} \qquad (2.7.4.1)$$

where M_{irr} is the irreversible component of magnetization M and M_{irr} is proportional to the current density. With $U(j) = U_0\,[1 - J/J_{c0}]$ from the Anderson and Kim Model, the relaxation rate S becomes:

$$S = \frac{d\ln M_{irr}}{d\ln t} = \frac{d\ln J}{d\ln t} = \frac{-k_B T}{U_0 - k_B T \ln(t/t_0)} \qquad (2.7.4.2)$$

In the limit in which the value for U_0 is very large compared to $k_B \ln(t / t_0)$, S reduces simply to:

$$S \cong \frac{-k_B T}{U_0} \qquad (2.7.4.3)$$

Using J from the interpolation relation (2.7.1.18), the value for S is:

$$S \cong \frac{k_B T}{U_0 + \mu k_B T \ln(t/t_0)} \qquad (2.7.4.4)$$

The above relation is different from Anderson and Kim's relation for S. Equation 2.6.1.4 shows that the normalized relaxation rate S decreases with time. For large enough temperatures, $\mu k_B T \ln(t/t_0) >> U_0$, and S is:

$$S \cong \frac{1}{\mu \ln(t/t_0)} \qquad (2.7.4.5)$$

The above equation predicts that S will have a plateau at high temperatures [97].

2.7.5 Experimental Determination of $U_{eff}(J)$: Maley Method

A linear dependence of the activation energy on the magnetic moment gives a logarithmic decay of the persistent current, with a simple relationship between the activation energy U_0 and the measurable logarithmic creep rate, S (see equation 2.7.4.3). In general, as discussed in section 2.7.1, U (J) is a non-linear function of J and may diverge at $J = 0$. There are different models and theories that have been developed to describe U (J) [98-112]. Maley et al. proposed a technique, based on the analysis of flux creep measurements, for experimental determination of U(J) [100]. In order to elucidate the explicit dependence of U on M or J for various temperatures, Maley specified a suitable form of the rate equation for thermally activated flux motion, given as:

$$\frac{U_{eff}}{k_B} = -T \ln\left|\frac{d(M - M_{eq})}{dt}\right| + \ln\left(\frac{H\gamma_0 a_d}{\pi d}\right) \qquad (2.7.5.1)$$

where k_B is the Boltzmann constant, γ_0 is the attempt frequency of the vortices, a_d is the hopping distance of the vortices, and d is the sample thickness.

The above relation was obtained from Beasley's flux diffusion equation [90, 100]

$$\frac{dH}{dt} = \nabla\left|Ha_d\gamma_0 \exp\left(-\frac{U_{eff}(J)}{k_BT}\right)\right| \tag{2.7.5.2}$$

The differential equation for the averaged magnetic induction is

$$\frac{d\langle H\rangle}{dt} = 4\pi\frac{dM_{irr}}{dt} = \left[\frac{4Ha_d\gamma_0}{d}\right]\exp\left(-\frac{U_{eff}(J)}{k_BT}\right) \tag{2.7.5.3}$$

Thus, we have

$$\frac{dM_{irr}}{dt} = \left[\frac{Ha_d\gamma_0}{d\pi}\right]\exp\left(-\frac{U_{eff}(J)}{k_BT}\right) \tag{2.7.5.4}$$

By taking the logarithm of both sides of the equation, (2.7.5.4) becomes

$$\ln\left|\frac{dM_{irr}}{dt}\right| = \ln\left[\frac{Ha_d\gamma_0}{d\pi}\right] - \frac{U_{eff}(J)}{k_BT} \tag{2.7.5.5}$$

and

$$\frac{U_{eff}(T)}{k_B} = -T\ln\left|\frac{dM_{irr}}{dt}\right| + T\ln\left[\frac{Ha_d\gamma_0}{d\pi}\right] \tag{2.7.5.6}$$

where it is assumed that $\ln\left(\frac{Ha_d\gamma_0}{d\pi}\right) = C = \text{constant}$

By choosing a constant term C =18 for each of the sets of relaxation data for different temperatures, a smooth dependence of U_{eff} on M was obtained. This value of constant C gives the physically acceptable value $\gamma_0 a_d \cong 25\text{cm s}^{-1}$, consistent with an hopping distance $\cong 1000$ Å and an attempt frequency of 2.5×10^7 Hz [100]. All these are measurable values, comparable to those commonly referred to in the literature.

2.8. Second Magnetization Peak Effect

One of the intriguing effects observable in high T_c superconductors (HTS) is the anomalous increase in the measured magnetization with increasing applied magnetic field (see Fig. 2.8.1). This phenomenon is called the second peak effect. The second magnetization peak is mostly observed in layered superconductors such as Bi2212 and Y123. The peak effect in Y123 is much stronger than that in Bi2212. The peak effect in Y123 samples appears over a wide range of temperatures ($0.2 < T/T_c < 1$). In Bi2212 single crystal, it appears between 20 and 40 K. In the literature, various interpretations have been proposed to explain the origin of the second peak in HTS [95, 113-122]. The peak in pure Bi2212 single crystals is observed due to the presence of oxygen vacancies. The extended defects induced by irradiation can introduce the peak effect into Bi2212 or Y123 single crystals. The irradiation may also enhance the peak present before irradiation or even destroy it. H. Kupfer et al. have suggested that statistically distributed uncorrelated defects are responsible for the occurrence of the second peak since the vortex pinning strength of these defects is weak [120]. However, for strong pinning centers such as correlated twins and the large clusters introduced by fast neutron irradiation, the peak will be suppressed or will vanish [120].

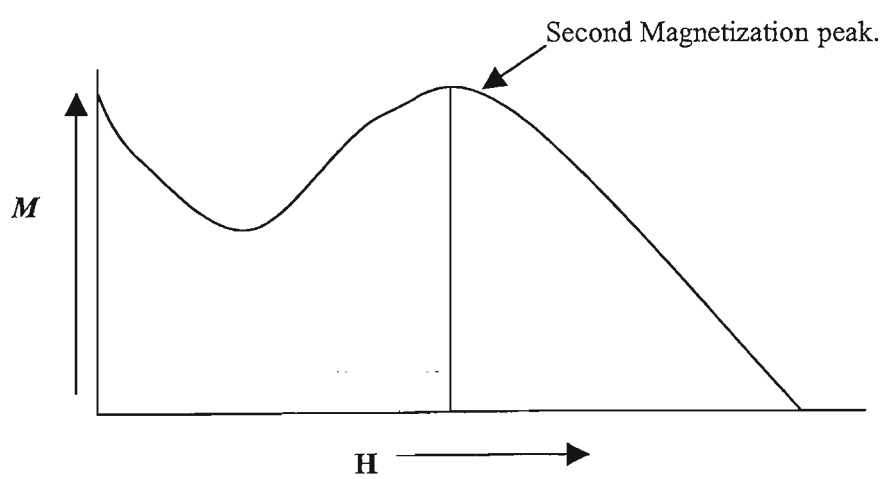

Fig. 2.8.1: A schematic diagram of the second magnetization peak (peak effect)

In the static collective pinning model, weak elementary pinning forces are proposed to be responsible for the peak. Oxygen vacancies can cause point like weak pinning centers of the appropriate type. Weak elementary pinning forces cause an elastic collective interaction of the vortex lattice. This interaction is characterized by the size of the correlated volume $V_C = R_C^2 L_c$ within which the short-range order of the vortex lattice is preserved. Here R_c and L_c represent the longitudinal and transverse correlation lengths, respectively. The field dependence of the current density is determined by the field dependence of V_C i. e. $J \sim V_C^{-1/2}$. In collective pinning theory, $V_C = R_C^2 L_C$ depends on the elastic moduli of the vortex line lattice: the tilt modulus C_{44} and the shear modulus C_{66} since $R_C \approx (C_{44}C_{66}^3)^{1/2}\xi^2/W$ and $L_C \approx R_C(C_{44}/C_{66})^{1/2}$, where W is the mean-square value of the random force produced by defects [85]. A discussion of elastic moduli as the origin of the second magnetization peak can be found in V. F. Solovyov et al. [119]. These authors have reported that the dimensional 3D to 2D crossover results in the second magnetization peak.

In the context of the vortex dynamic model, the vortex elastic to plastic transition has been suggested as the origin of the peak effect. It is well known that, over a wide range of vortex dynamics in high temperature superconductors, magnetic relaxation can be described in terms of collective vortex creep based on the concept of the elastic motion of the vortex lattice. However, it has also been suggested that plastic deformation dominates the vortex lattice motion in the creep regime at elevated temperatures at fields above the characteristic field H_{peak}, corresponding to the second peak in the magnetization [121]. The plastic vortex motion is classified into three main categories [116]: (a) Vortex channeling along easy paths in the pinning relief regime in between rather stationary vortex lattice islands; (ii) Vortex motion that resembles an ice flow in

which large pieces of vortex-lattice slide with respect with each other; (iii) Dislocation mediated plastic creep of the vortex lattice similar to diffusion of dislocations in atomic solids. In order to determine the crossover separating the elastic and plastic creep regimes, the collective pinning theory for $J << J_c$ has been used, where the activation energy is defined as:

$$U(H, J) = U_0(H)(J_c/J)^{\mu} \propto H^{\nu} J^{-\mu}$$

Here μ and ν are the critical exponents and determine the vortex pinning regimes. For $J << J_c$, $J \propto H^{\nu/\mu}$ [116, 123]. Using the above relation in Y123, the value of $\mu = 1$ has been estimated from the magnetic relaxation at low fields and $\mu = 2$ at fields just below the second peak field H_{peak}. Collective pinning theory gives $\mu = 1$ in the intermediate bundle regime and $\mu = 5/2$ in the small bundle regime [116, 123]. This shows that the vortices below H_{peak} are described by the collective pinning theory. However, at fields above H_{peak} $\mu = 0.2$ has been reported [123]. In collective pinning theory, $\mu = 1/7$ corresponds to a single vortex pinning regime (which is expected only for low fields and below H_{peak}). Thus, the value of $\mu = 0.2$ is inconsistent with the collective pinning theory; this implies that the vortices above the peak are not elastic but rather plastic.

2.9 References for Chapter Two

1. J. H. Schrieffer, *Theory of Superconductivity*, W.A.Benjamin, New York, pp. 10-23(1964).
2. D. R. Tilley and J. Tilley, *Superfluidity and Superconductivity* (3rd ed.), Institute of Physics, Bristol, Philadelphia, pp 206-210 (1986).
3. P. G. D. Gennes, *Superconductivity of Metals and Alloys*, W. A. Benjamin, Inc., New York, pp 55-63 (1966).
4. M. K. Wu, T. R. Ashburn, C. J. Torng, P. H. Hor, R. L. Meng, L. Gao, Z. J. Huang, Y. Q. Wang and C. W. Chu, *Phys. Rev. Lett.* **58,** 908 (1987).
5. C. C. Torardi, *Chemistry of superconductor materials*, T. A. Vanderah, ed., Noyes Publications, Oark Ridge, New Jersey, U.S.A, pp 485-490 (1992).
6. C. Michel, M. Hervieu, M. M. Borel, A.. Grandin, F. Deslandes, J. Provost and B. Raveau, *Z. Phys. B* **68,** 421 (1987).
7. H. Maeda, Y. Tanaka, M. Fukutomi and T. Asano, *Jpn. J. Appl. Phys.* **27,** L209 (1998).
8. H. Yan, Z. Mao, G. Xu and Y. Zhang, *Phys. Rev. B* **59,** 8459 (1999).
9. H. Jiang, F. H. Li, W. Liu, Y. Zhang and Z. Q. Mao, *Physica C* **305**, 202 (1998).
10. X. Sun, X. Zhao, W. Wu, X. Fan, X. G. Li and H. C. Ku, *Physica C* **307**, 67(1998).
11. H. Yan, Z. Mao, G. Xu, L. Shi, M. Tian and Y. Zhang, *Physica C* **309**, 263 (1998).
12. Hazen R M, *Physical properties of high temperature superconductors II*, D. M. Ginsberg ed., World Scientific, Singapore, p. 121-198 (1990).

13. X. Zhao, X. Sun, X. Fan, W. Wu, X. G. Li, S. Guo and Z. Zhao, *Physica C* **307**, 265 (1998).

14. A. A. Abrikosov, *Soviet Phys. JEPT* **5**, 117 (1957).

15. G. Blatter, M. V. Feigel'man, V. B. Geshkenbein, A. I. Larkin and V. M. Vinokur, *Rev. of Mod. Phys.* **66**, 1125 (1994).

16. K. H. Fischer, *Supercond. Rev.* **1,** 153 (1995).

17. D. R. Nelson, *Phys. Rev. Lett.*, **60,** 1973 (1988).

18. D. R. Nelson and H. S. Seung, *Phys. Rev. B* **39,** 9153 (1989).

19. C. D. Dewhurst and R. A. Doyle, *Phys. Rev. B*, **56** 10832 (1997).

20. D. Majer, E. Zeldov and M. Konczykowski, *Phys. Rev. Lett.* **75,** 1166 (1995).

21. D. E. Farrell, E. Johnston-Halperin, L. Klein, P. Fournier, A. Kapitulnik, E. M. Forgan, A. I. M. Rae, T. W. Li, M. L. Trawick, R. Sasik and J. C. Garland, *Phys. Rev. B* **53,** 11807 (1996).

22. T. Tsuboi, T. Hanaguri and A. Maeda, *Phys. Rev. B* **55,** R8709 (1997).

23. C. D. Keener, M. L. Trawick, S. M. Ammirata, S. E. Hebboul and J. C. Garland, *Phys. Rev. Lett.* **78,** 1118 (1997).

24. K. Kadowaki and K. Kimura, *Phys. Rev. B* **57,** 11674 (1998).

25. F. Lindemann, *Phys. Z.* **11,** 69 (1910).

26. E. H. Brandt, *Phys. Stat. Solidi* (b), **77.** 551 (1976).

27. E. H. Brandt, *J. Low. Temp. Phys.* **26,** 709 (1977).

28. E. H. Brandt, *J. Low. Temp. Phys.* **26,** 735 (1977).

29. E. H. Brandt, *Phys. Rev. B* **34,** 6514 (1986).

30. A. Sudbo and E. H. Brandt, *Phys. Rev. B* **43,** 10482 (1991).

31. A. Sudbo and E. H. Brandt, *Phys. Rev. Lett.* **66,** 1781 (1991).

32. A. Houghton, R. A. Pelcovits and A. Sudbo, *Phys. Rev. B* **40,** 6763 (1989).

33. M. Tachiki and S. Takahashi, *Solid St. Comm.* **70**, 291 (1989).

34. D. Feinberg and C. Villard, *Phys. Rev. Lett.* **65**, 919 (1993).

35. R. W. Giannetta, N. H. Tea, F. A. B. Chaves, S. Rao, M. B. Salamon, A. M. Kini, H. H. Wang, U. Geiser, J. Schlueter, M. W. Trawick and J. C. Garland, *Physica C* **321** 207 (1999).

36. D. T. Fuchs, R. A. Doyle, E. Zeldov, S. F. W. R. Rycroft, T. Tamegai, S. Ooi, M. L. Rappaport and Y. Myasoedov, *Phys. Rev. Lett.* **81**, 3944 (1998).

37. A. Mazilu, H. Safar, D. Lopez, W. K. Kwok, G. W. Crabtree, P. Guptasarma and D. G. Hinks, *Phys. Rev. B* **58**, R8913 (1998).

38. M. Benkraouda and J. R. Clem, *Phys. Rev. B* **58**, 15103 (1998).

39. L. Burlachkov, A. E. Koshelev and V. M. Vinokur, *Phys. Rev. B* **54**, 6750 (1996).

40. N. Chikumoto, M. Konczykowski, N. Motohira and A. P. Malozemoff, *Phys. Rev. Lett.* **69**, 9071 (1992).

41. N. Morozov, E. Zeldov, M. Konczykowski and R. A. Doyle, *Physica C* **291**, 113 (1997).

42. R. A. Doyle, S. F. W. R. Rycroft, C. D. Dewhurst, E. Zeldov, I. Tsabba. S. Reich, T. B. Doyle, T. Tamegai and S. Ooi, *Physica C* **308**, 123 (1998).

43. G. Yang, J. S. Abell and C. E. Gough, *Physica C* **282**, 2007 (1997).

44. R. A. Doyle, S. F. W. R. Rycroft, T. B. Doyle, E. Zeldov, T. Tamegai and S. Ooi, *Phys. Rev. B* **58**, 135 (1998).

45. M. Benkraouda and J. R. Clem, *Phys. Rev. B* **53**, 5716 (1996).

46. J. Horvat, *Hand book of advanced Elecronic and Photonic Materials and Devices*, H. S. Nalwa, ed, Academic Press, New York, p.158 **3** (1998).

47. S. Sengupta and D. Shi, *High Temperature Superconducting Materials Science and Engineering: New Concepts and Tchnology,* D. Shi, ed, Pergamon, Elmsford, New York, p 131(1995).

48. J. T. Totty, G. K. Perkins, H. J. Jensen, R. A. Doyle and L. F. Cohen, *Supercond. Sci. Technol.* **11** 866 (1998).

49. C. Goupil, A. Ruyter, V. Hardy and Ch. Simon, *Physica C* **278**, 23 (1997).

50. A. K. Pradhan, G. D. Gu, K. Nakao, N. Koshizuka and D. Kanjilal, *Phys. Rev. B* **61**, 14374 (2000).

51. P. Fisher, R. Busch, H. W. Neumuller, G. Ries and H. F. Braun, *Supercond. Sci. Tech.* **5**, S440 (1992).

52. J. R. Thompson, L. Krusin-Elbaum, D. K. Christen, K. J. Song, M. Paranthaman, J. L. Ullmann, J. Z. Wu, Z. F. Ren, J. H. Wang, J. E. Tkaczyk and J. A. DeLuca, *Appl. Phys. Lett.* **71**, 536 (1997).

53. J. R. Thompson, L. Krusin-Elbaum, L. Civale, G. Blatter and C. Field, *Phys. Rev. Lett.* **78**, 3181 (1997).

54. H. W. Neumuller, W. Gerhause, G. Ries, P. Kummeth, W. Schmidt, S. Klaumunzer and G. Saemann-Ischenko, *Cryogenics* **33**, 14 (1993).

55. J. H. Cho, H. Safar, M. P. Maley, J. O. Willis, J. Y. Coulter, D. G. Steel and K. E. Gray, *Physica C* **302,** 113 (1998).

56. S. Hebert, V. Hardy, G. Villard, M. Hervieu, Ch. Simon and J. Provost, *Physica C* **299**, 259 (1998).

57. M. Kosugi, Y. Matsuda, M. B. Gaifullin, K. Kumagai, N. Chikumoto, J. Shimoyama, K. Kishio, K. Hirata and M. Konczykowski, *Physica C* **293**, 208 (1997).

58. C. H. Chen, *Physical properties of high temperature superconductors II*, D. M. Ginsberg ed., World Scientific, Singapore, p. 199-260 (1990).

59. I. Chong, Z. Hiroi, M. Izumi, J. Shimoyama, Y. Nakayama, K. Kishio, T. Terashima, Y. Bando and M. Takano, *Science* **276** 770 (1997).

60. Z. Hiroi, I. Chong and M. Takano, J. *Solid State Chem.* **138** 98 (1998).

61. J. Horvat, X. L. Wang and S. X. Dou, *Physica C* **324** 211 (1999).

62. M. Nishiyama, K. Ogawa, I. Chong, Z. Hiroi and M. Takano, *Physica C* **314** 299 (1999).

63. K. Kishio, J. Shimoyama, Y. Nakayama, K. Kitazawa, Z. Hiroi, I. Chong and M. Takano *Proc. 3rd Joint ISTEC/MRS Int'l Workshop on Superconductivity co-sponsored by ISTEC, Tokyo, 1997, pp 105-107, Big, Island, HI, USA, July 1997.*

64. T. Motohashi, Y. Nakayama, T. Fujita, K. Kitazawa, J. Shimoyama and K. Kishio, *Phys. Rev. B* **59**, 14080 (1999).

65. D. Zech, J. Hofer, H. Keller, C. Rossel, P. Bauer and J. Karpinski, *Phys. Rev. B* **53**, R6026 (1996).

66. G. D. Gu, K. Takamuku, N. Koshizuka and S. Tanaka, *J. of Cryst. Growth* **137,** 472 (1994).

67. B. vom Hedt, W. Lisseck, K. Westerholt and H. Bach, *Phys. Rev. B* **49,** 9898 (1994).

68. X. L. Wang, J. Horvat, G. D. Gu, K. K. Uprety, H. K. Liu and S. X. Dou, *Physica C* **337,** 221 (2000).

69. G. D. Gu, G. J. Russell and N. Koshizuka, *Physica C* **282-287,** 2107 (1997).

70. O. V.Misochko and G.Gu, *Phys. Rev. B* **59,** 11183 (1999).

71. S. Ooi, T. Shibauchi and T. Tamegai, *Physica C* **302,** 339 (1998).

72. B. Khaykovich, E. Zeldov, D. Majer, T. W. Li, P. H. Kes and M. Konczykowski, *Phys. Rev. B* **76,** 2555 (1996).

73. X. H. Chen, M. Yu, K. Q. Ruan and S. Y. Li, Z. Gui, G. C. Zhang and L. Z. Cao, *Phys. Rev. B* **58,** 14219 (1998).

74. G. Yang, P. Shang, S. D. Sutton, I. P. jones, C. E. Gough and J. S. Abell, *Phys. Rev. B* **48,** 4054 (1993).

75. X. L. wang, J. Horvat, H. K. Liu, J. N. Li, and S. X. Dou, *Phys. Rev. B* **55,** R3402 (1997).

76. J. Horvat, R. Bhasale, Y. C. Guo, H. K. Liu and S. X. Dou, *Supercond. Sci. Technol.* **10,** 409 (1997).

77. C. P. Bean, *Phys. Rev. Lett.* **8,** 250 (1962).

78. C. P. Bean, *Rev. Mod. Phys.***36,** 31 (1962).

79. P. W. Anderson, *Phys. Rev. Lett.* **9,** 309 (1962).

80. P. W. Anderson and Y. B. Kim, *Rev. Mod. Phys.* **36,** 39 (1964).

81. E. M. Gyorgy, R. B. VanDover, L. F. Schneemeyer, A. E. White, M. M. O'Bryan, R. J. Felder, J. V. Waszczak and W. W. Rodes, *Appl. Phys. Lett.* **55**, 283 (1989).

82. W. A. Fietz, M. R. Beasely, J. Silcox and W. W. Webb, *Phys. Rev.* **136**, A335 (1964).

83. W. A. Fietz and W. W. Webb, *Phys. Rev.* **178**, 657 (1969).

84. A. I. Larkin and Y. N. Ocvchinnikov, *J. Low Temp. Phys.* **34,** 409 (1979).

85. M. V. Feigel'man, V. B. Geshkenbein, A. I. Larkin and V. M. Vinokur, *Phys. Rev. Lett.* **63**, 2303 (1989).

86. M. V. Feigel'man, V. B. Geshkenbein, A. I. Larkin and V. M. Vinokur, *Phys. Rev. B* **43**, 6263 (1991).

87. Y. Yeshurun, A. P. Malozemoff and A. Shaulov, *Rev. Mod. Phys.* **68,** 911 (1996).

88. S. Sengupta, D. Shi, S. Sergeenkov and P. J. McGinn, *Phys. Rev. B* **48,** 6736 (1993).

89. G. A. Levin, C. C. Almasan, D. A. Gajewski and M. B. Maple, *Appl. Phys. Lett.*, **72** 11 (1997).

90. M. R. Beasley, R. Labusch and W. W. Web, *Phys. Rev.* **181**, 682 (1969).

91. R. H. Koch, V. Foglietti and M. P. A. Fisher, *Phys. Rev. Lett.* **64,** 2586 (1990).

92. R. H. Koch, V. Foglietti, W. J. Gallgher, G. Koren, A. Gupta and M. P. A. Fisher, *Phys. Rev. Lett.* **63,** 1511 (1989).

93. D. S. Fisher, M. P. A. Fisher and D. A. Huse, *Phys. Rev. B* **43,** 130 (1991).

94. V. M. Geshkenbein and A. I. Larkin, *Sov. Phys. JETP* **68,** 639 (1989).

95. M. Niderost, A. Suter, P. Visani, A. C. Mota and G. Blatter, *Phys. Rev. B* **53**, 9286 (1996).

96. H. Safar, P. L. Gammel, D. J. Bishop, D. B. Mitzi and A. Kapitulnik, *Phys. Rev. Lett* **68,** 2673 (1992).

97. H. Safar, P. L. Gammel, D. J. Bishop, D. B. Mitzi and A. Kapitulnik, *Phys. Rev. Lett.* **68,** 2672 (1992).

98. S. SenGupta, D. Shi, Z. Wang, M. E. Smith and S. Salem-Sugui and P. J. McGinn, *Phys. Rev. B* **49,** 5414 (1993).

99. Y. Abulafia, A. Shaulov, Y. Wolfus, R. Prozorov, L. Burlachkov, Y. Yeshurum, D. Majer, E. Zeldov and V. M. Vinokur, *Phys. Rev. Lett.* **75,** 2404 (1995).

100. M. P. Maley, J. O. Willis, H. Lessure and M. E. McHenry, *Phys. Rev. B* **42,** 2639 (1990).

101. M. Tinkham, *Phys. Rev. Lett.* **61,** 1658 (1988).

102. M. E. McHernry, S. Simizu, H. Lessure, M. P. Maley, J. Y. Coulter, I. Tanaka and H. Kojima, *Phys. Rev. B.* **44,** 7614 (1991).

103. S. Sengupta, D. Shi, Z. Wang, M. E. Smith, S. Salem-Sugui, P. J. McGinn and K. DeMoranville, *J. Appl. Phys.* **72,** 592 (1992).

104. S. Sengupta, D. Shi, Z. Wang, M. E. Smith and P. J. McGinn, *Phys. Rev. B* **47,** 5165 (1993).

105. S. Sengupta, D. Shi, S. Sergeenkov and P. J. McGinn, *Phys. Rev. B* **48,** 6736 (1993).

106. P. J. Kung, M. P. Maley, M. E. McHenry, J. O. Wills, M. Murakami and S. Tanaka, *Phys. Rev. B* **46,** 6427 (1992).

107. P. J. Kung, M. P. Maley, M. E. McHenry, J. O. Wills, M. Murakami and S. Tanaka, *Phys. Rev. B* **48,** 13923 (1993).

108. M. Reissner and J. Lorentz, *Phys. Rev. B* **56,** 6273 (1997).

109. Y. G. Xiao, B. Yin, J. W. Li, Z. X. Zhao, X. K. Fu, H.T. Ren and L. Xiao, *J. Appl. Phys.* **81,** 2309 (1997).

110. H. Darhmaoui and J. Jung, *Phys. Rev. B* **57,** 8009 (1998).

111. J. Jung and H. Darhmaoui, *Supercond. Sci. and Technol.* **11**, 973 (1998).

112. H. H. Wen, P. Ziemann, H. A. Radovan and T. Herzog, *Physica C* **305,** 186 (1998).

113. L. Krusin-Elbaum, L. Civale, V. M. Vinokur and F. Holtzberg, *Phys. Rev. Lett.* **69,** 2280 (1992).

114. B. Horovitz, *Phys. Rev. B* **57,** 8009 (1998).

115. M. Daeumling, J. M. Seuntjens and D. C. Larbalestier, *Nature* **346,** 332 (1990).

116. J. Abulafia, A. Shaulov, Y. Wolfus, R. Prozorov, R. Burlackhov, Y. yeshurun, D. Mayer, E. Zeldov, H. Wuhl, V. G. Geshkenbein and V. M. Vinokur, *Phys. Rev. Lett.* **77,** 1596 (1996).

117. T. Aouaroun, V. Hardy and C. Simon, *Physica C* **294**, 42 (1998).

118. Y. Yeshurun, N. Bontemps, L. Burlachkov and A. Kapitulnik, *Phys. Rev. B* **49,** 1548 (1994).

119. V. F. Solovyov, V. M. Pan, H. C. Freyhardt, M. H. Ionescu and S. X. Dou, *Supercond. Sci. Technol.* **11,** 935 (1998).

120. H. Küpfer, Th. Wolf, C. Lessing, A. A. Zhukov, X. Lancon, R. Meier-Hirmer, W. Schauer and H. Wuhl, *Phys. Rev. B* **58,** 2886 (1998).

121. T. Aouaroun and C. Simon, *Phys. Rev. B* **58,** 11692 (1998).

122. E. H. Brandt, *Phys. Rev. B* **34,** 6514 (1986).

123. Krusin-Elbaum, L. Civale, V. M. Vinokur and F. Holtzberg, *Phys. Rev. Lett.* **69**, 2280 (1992).

CHAPTER THREE: EXPERIMENTAL PROCEDURE

3.1 Sample Preparation

3.1.1 Fabrication of Bi-2212 Single Crystals

The following are the standard methods used for the growth of Bi2212 single crystals [1-6]: Self-flux growth, Alkali-halide flux growth and Traveling Solvent Floating Zone (TSFZ) growth. The most commonly used methods among them are the self-flux growth method and the traveling solvent floating zone method. For our samples, we used the self-flux growth method and the floating zone method.

3.1.1.1 Fabrication of Bi2212 Single Crystals by the Self-Flux Growth Method

The Self-flux growth technique is a high temperature solution growth method. The crystal size and quality depend strongly upon the different starting compositions. The chemical composition of the powders is very important in order to get the best result for the critical temperature. The T_c dependence on the stoichiometric values of the nominal composition of the powder based on the formula $Bi_{2+x}Sr_{2+y}Ca_{1+z}Cu_{2+w}O_{8+\delta}$, is given by Micheal et al. [2]. A mixture of high purity (99.9%) powders of Bi_2O_3, $SrCO_3$, $CaCO_3$ and CuO was used to grow Bi2212 single crystals. The mixed powder of stoichiometric starting ratio 2:2:1:2 was loaded into a high purity Alumina (Al_2O_3) crucible. Fig.3. 1.1.1a shows a schematic diagram of a cross section of the configuration of a Muffle furnace for the crystal growth. The temperature of the furnace was raised to 1050°C, which is above the melting temperature of the powder sample, and held at this temperature for 4 hours to reach thermodynamic equilibrium. The temperature was then

lowered to 980°C (just above onset of solidification) at a cooling rate of 400°C per hour and then slowly lowered down to 840°C at a rate of 0.8°C per hour. The sample was then rapidly cooled down to 550°C (200°C per hour) and held at this temperature for approximately 8 hours. The crucible was then quenched in air. A temperature profile for the crystal growth is shown in Figure 3.1.1.1b. After the thermal heat treatment, the crucible was crushed mechanically to obtain a matrix of crystals. The single crystals were extracted from the matrix by cleaving exposed crystals with an adhesive tape. The adhesive tape was removed from the crystal by dissolving it in hexane.

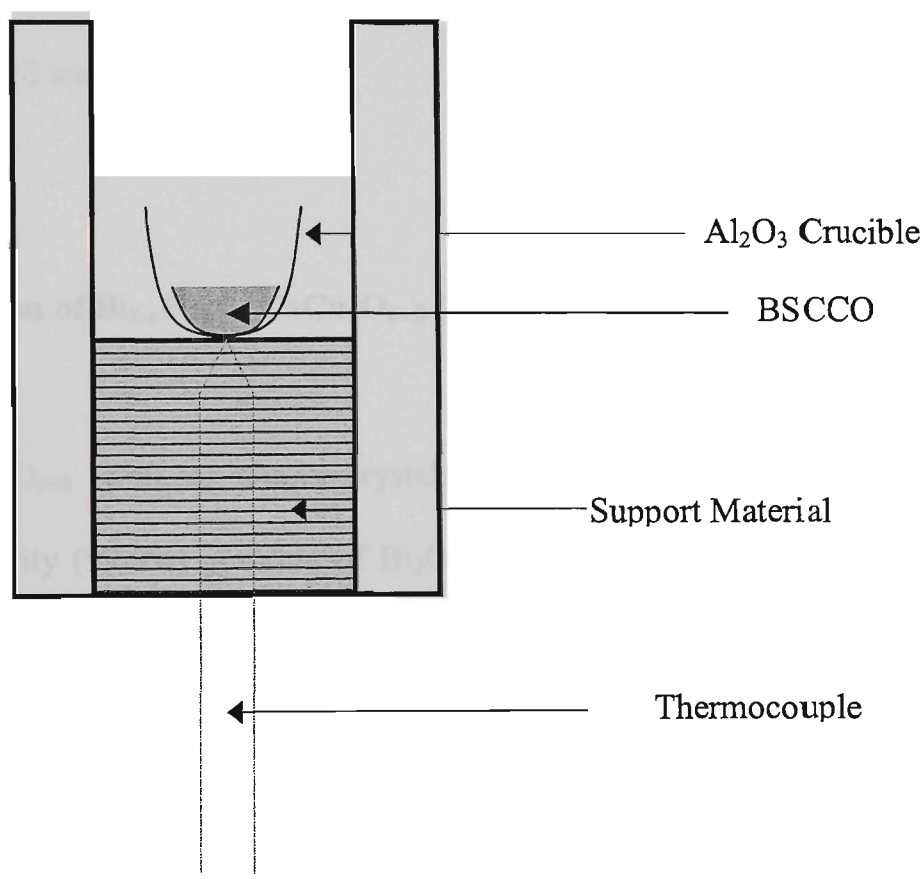

Fig. 3.1.1.1a: Configuration of the Muffle furnace for Bi-2212 crystal growth by the self–flux method.

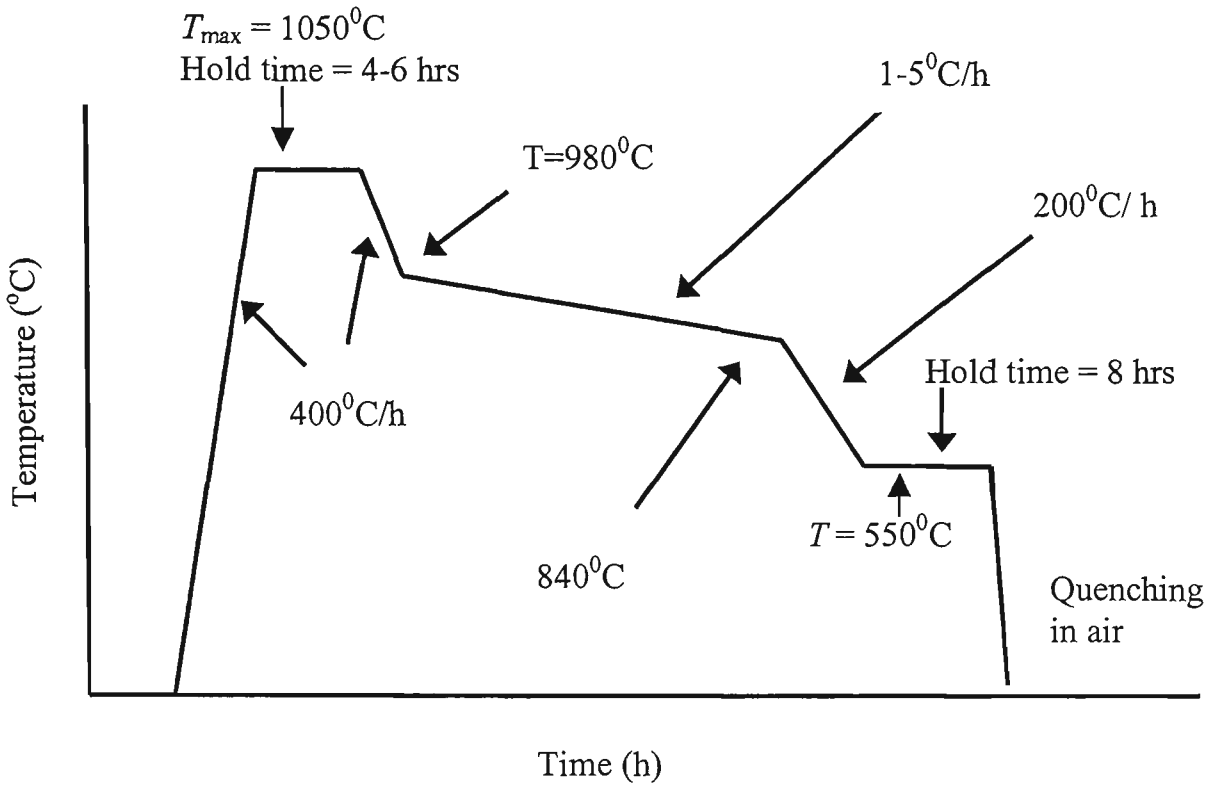

Fig. 3.1.1.1b: Schematic drawing of the thermal treatment used in the growth of Bi-2212 single crystal.

3.1.1.2 Fabrication of $Bi_{2-x}Pb_xSr_2CaCu_2O_{8+\delta}$ (x = 0.34) Single Crystals by Self-Flux Growth Method:

$Bi_{2-x}Pb_xSr_2CaCu_2O_{8+\delta}$ (x=0.34) single crystals were grown by a self-flux growth method. High purity (99.9%) powders of Bi_2O_3, PbO, $SrCO_3$, $CaCO_3$ and CuO were mixed well according to the atomic ratios Bi:Pb:Sr:Ca:Cu = 4:2:4:2:2 [7,8]. About 50 grams of the mixture was placed into an Al_2O_3 crucible. The crucible was placed inside box furnace in such a way as to obtain a natural temperature gradient in the crucible. The thermal treatment for this growth is almost the same as that for pure Bi2212 single crystal. However, due to significant evaporation of Pb at high temperatures (due to the low melting point and high vapour pressure of PbO), there are some modifications in the procedures described for the fabrication of Bi2212 single crystals.

The first modification is that the maximum temperature and holding time is made 50°C lower and 2 hours shorter for the growth of Pb doped Bi2212 single crystals than for pure Bi2212 single crystals, see Figs. 3.1.1.1b and 3.1.1.2. This prevents a significant loss of Pb through evaporation at high temperatures. The second modification is that a faster cooling rate of 20-50°C per hour (1-5°C for pure Bi 2212) was employed. After the crystal growth, the crucible was crushed mechanically, and crystals were obtained by cleaving from the matrix of as-grown bulk crystal.

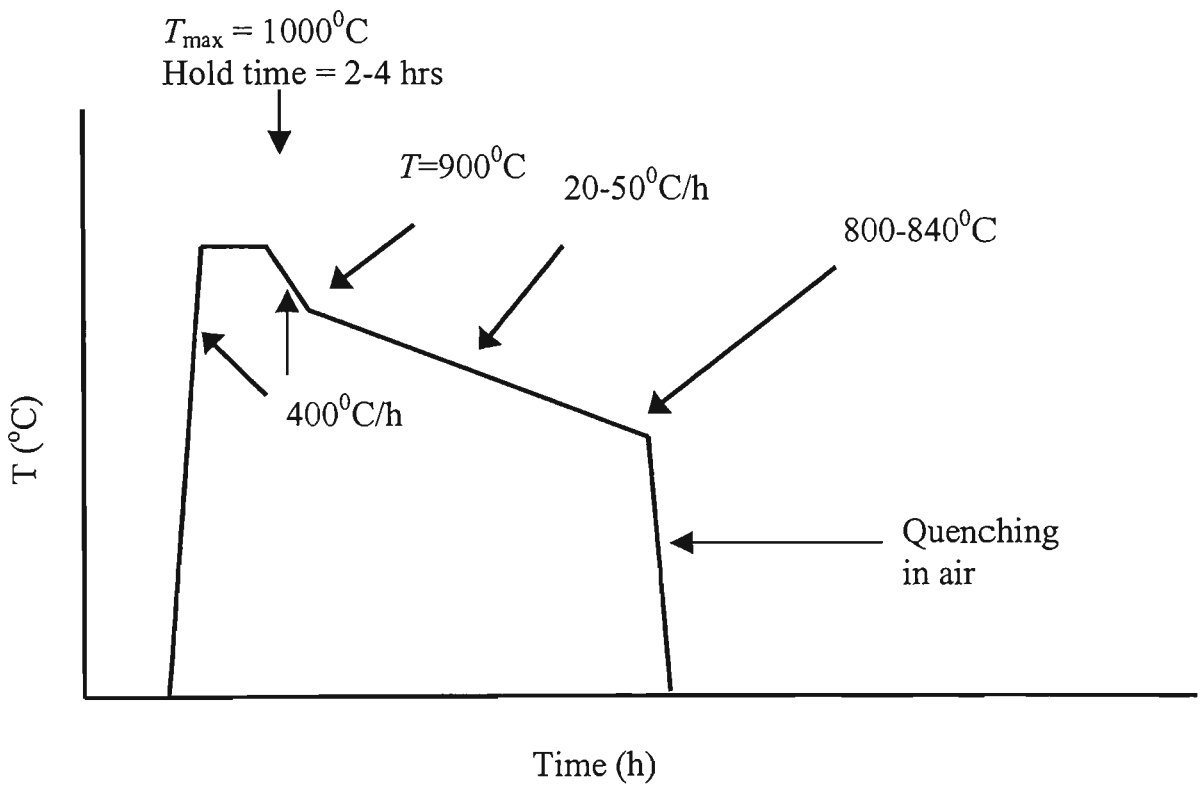

3.1.1.2. Schematic drawing for the temperature profile used in the growth of heavily Pb doped Bi-2212 single crystals.

3.1.1.3 Fabrication of $Bi_{2.1}Sr_{1.9}Ca_{1.0}(Cu_{1-y}Fe_y)_2O_{8+\delta}$ Single Crystals by Floating Zone Method

Fe-doped single crystals were grown from a starting composition of $Bi_{2.1}Sr_{1.9}Ca_{1.0}(Cu_{1-y}Fe_y)_2O_{8+\delta}$ (y = 0, 0.005,0.016, 0.022) by a conventional floating zone (FZ) method using an infrared radiation furnace [9]. The furnace was equipped with two ellipsoidal mirrors and two 500 W halogen lamps. The powders of Bi_2O_3, $SrCO_3$, $CaCO_3$ and CuO (all with purity > 99.99%) were mixed in their stoichiometric ratios, ground in an agate mortar and calcined for 48 hours at 810°C. The calcined powders were reground, calcined for 72 hours at 840°C, and then again reground. The reground powders were placed in a tube and hydrostatically pressed into a rod under 2000kg/cm^2. The pressed rods were sintered at 860°C for 72 hrs in air to form a feed rod and a seed rod, and 840°C to provide solvent materials. The sintered rods were then mounted in the FZ furnace and pre-melted at a velocity of 25mm/h to keep the molten zone stable. The molten zone was quenched by turning off the halogen lamps to obtain the single crystals.

3.2 Sample Characterizations:

3.2.1 X-Ray Diffraction Pattern (XRD) Technique:

The X-ray diffraction pattern technique has been employed for phase analysis, to study texture and to calculate the lattice parameters of our Bi2212 crystals. In X-ray investigations, monochromatized CuK_{α}-radiation from a normal focus X-ray tube, having wavelengths $\lambda = 1.5405$ Å and 1.5443 Å was used. Fig. 3.2.1.1 shows the X-ray diffraction pattern of the $Bi_{2.1}Sr_{1.9}Ca_{1.0}(Cu_{1-y}Fe_y)_2O_{8+\delta}$ single crystals with iron content $y = 0$ and $y = 0.016$, as well as a heavily Pb doped $Bi_{2-x}Pb_xSr_2CaCu_2O_{8+\delta}$ ($x = 0.34$) single crystal. The diffraction peaks are indicated by the Miller indices, h, k, l. It can be seen from Figure 3.2.1.1 that the peaks corresponding to the (00 l) Miller indices ($l = 2$, 6, 8, 10, 12) are very strong and narrow. The strong diffraction peaks show a high degree of preferred orientation of the crystallographic planes. The peak positions in the lead doped and iron doped samples were shifted by a small amount from that in the pure single crystal. In heavily Pb doped single crystal, the peak positions are shifted to higher values of angle 2-theta. However, in Fe doped single crystals, the peak positions are shifted to lower values. The peak positions for these crystals are described in Table 3.2.1.1.The lattice parameters were calculated from the XRD patterns, by indexing the peaks using Rietveld Analysis. The lattice parameters for pure (y = 0) Bi2212, iron doped Bi2212 (y = 0.016) and Pb doped Bi2212 (x = 0.34) single crystals are given in Table 3.2.1.2.

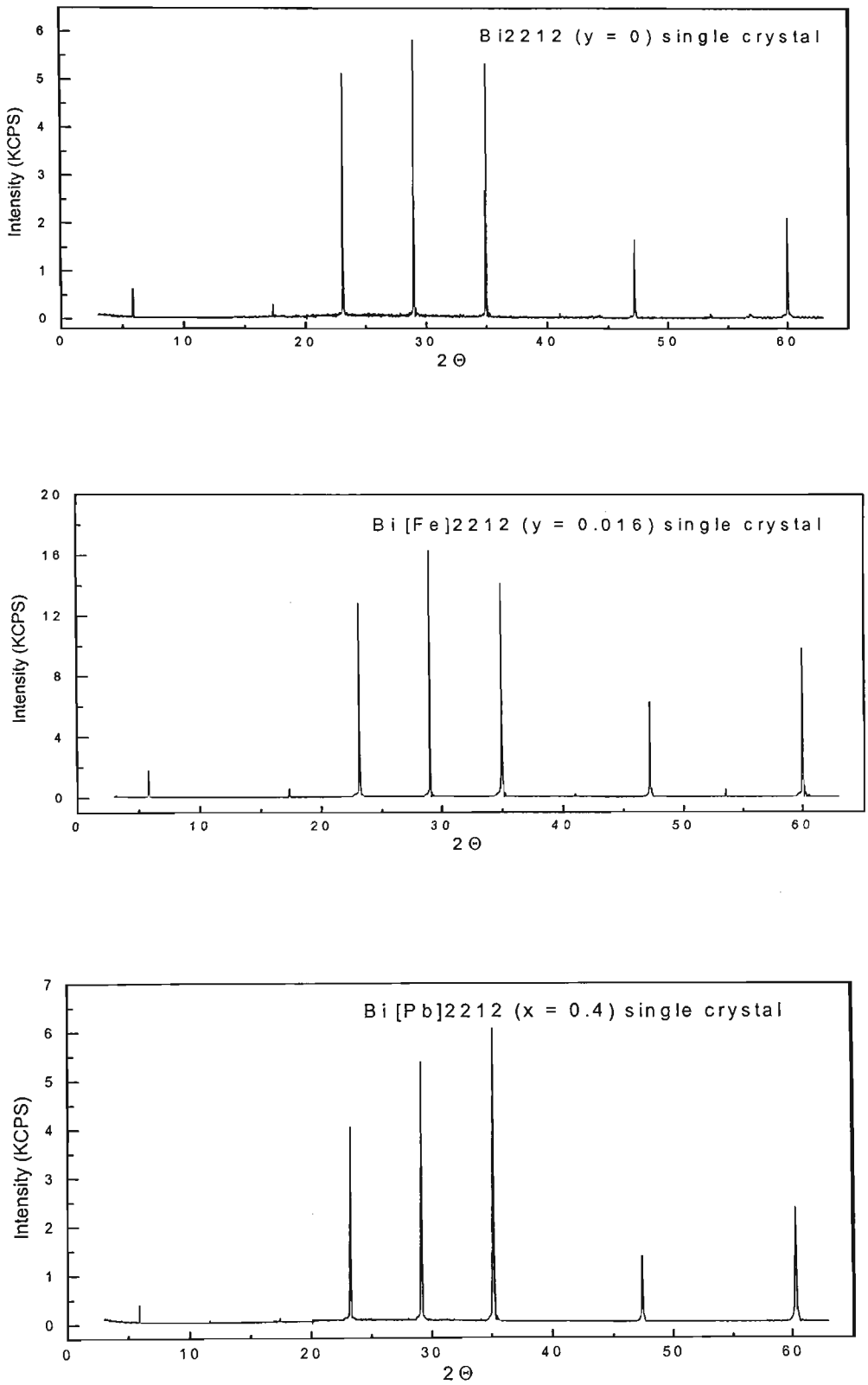

Figure 3.2.1.1: XRD patterns of (1) Pure Bi2212 ($y = 0$) single crystal (b) iron doped Bi2212 ($y = 0.016$) single crystal and (c) heavily Pb doped Bi2212 ($x = 0.34$) single crystal.

Miller Indices (00*l*)	Bi2212 (y = 0) Peak position in angle 2θ	Bi2212 (y = 0.016) Peak position in angle 2θ	Heavily Pb doped Bi2212 (x=0.34) Peak position in angle 2θ
002	5.84	5.808	5.901
006	17.318	17.315	17.428
008	23.137	23.132	23.248
0010	29.005	28.996	29.145
0012	34.96	34.949	35.12
0016	47.193	47.183	47.412

Table 3.2.1.1: Peak positions for pure Bi2212 ($y = 0$), iron doped Bi2212 ($y = 0.16$) and lead doped Bi2212 ($x = 0.34$) single crystals.

Name of Crystals	Lattice parameter a (Å)	Lattice parameter b (Å)	Lattice parameter c (Å)
$Bi_{2.1}Sr_{1.9}Ca_{1.0}(Cu_{1y}Fe_y)_2O_{8+\delta}$ (y = 0)	5.128 ± 0.002	5.811 ± 0.003	30.80 ± 0.07
$Bi_{2.1}Sr_{1.9}Ca_{1.0}(Cu_{1y}Fe_y)_2O_{8+\delta}$ (y = 0.016)	5.128 ± 0.002	5.811 ± 0.003	30.80 ± 0.05
$Bi_{2-x}Pb_xSr_2CaCu_2O_{8+\delta}$ ($x = 0.34$)	5.131 ± 0.001	5.778 ± 0.002	30.67 ± 0.01

Table 3.2.1.2: Lattice parameters for pure Bi2212 ($y = 0$), iron doped Bi2212 ($y = 0.16$) and lead doped Bi2212 ($x = 0.34$) single crystals.

The Pb content in our single crystals was determined by using energy dispersive X –ray diffraction spectra (EDS). Fig. 3.2.1.2 shows the EDS profile for a heavily Pb doped Bi2212 single crystal. The Pb content was determined to be 0.34.

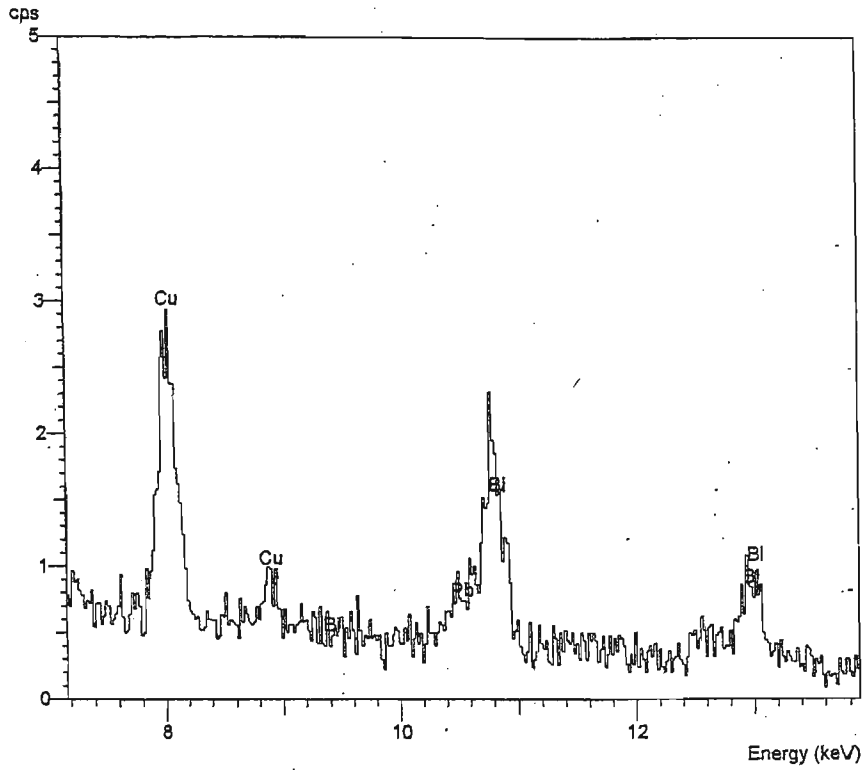

Fig. 3.2.1.2: Energy dispersive X ray diffraction spectra for heavily Pb doped Bi2212 single crystal.

3.2.2 Atomic Force Microscopy

The surface morphology of the Bi2212 single crystals was studied by Atomic Force Microscopy (AFM). For heavily Pb doped single crystal, Fig. 3.2.2.1 shows a pattern of lines. These lines were observed for different tip scan angles (0°, 90°, and 45°). Therefore, they are not an artifact of scanning the tip over the sample surface. A high-resolution electron microscope study of the heavily Pb doped Bi2212 single crystals has reported the presence of lamellae, consisting of Pb-rich and Pb-poor regions in the crystal [10]. We therefore believe that the lines in Fig. 3.2.2.1 are the consequence of this lamellar structure. As the crystal was cleaved, the differences in the mechanical properties between the Pb-rich and Pb-poor lamellae probably led to the observed lines. Fig. 3.2.2.2 shows a three-dimensional AFM image of the same crystal. These lines were not observed in Bi2212 single crystal with Fe concentration y = 0, 0.005, 0.016 and 0.022 (See Fig. 3.2.2.3 for a three-dimensional AFM image of the y = 0.016 single crystal). All the crystals display very regular surface morphology.

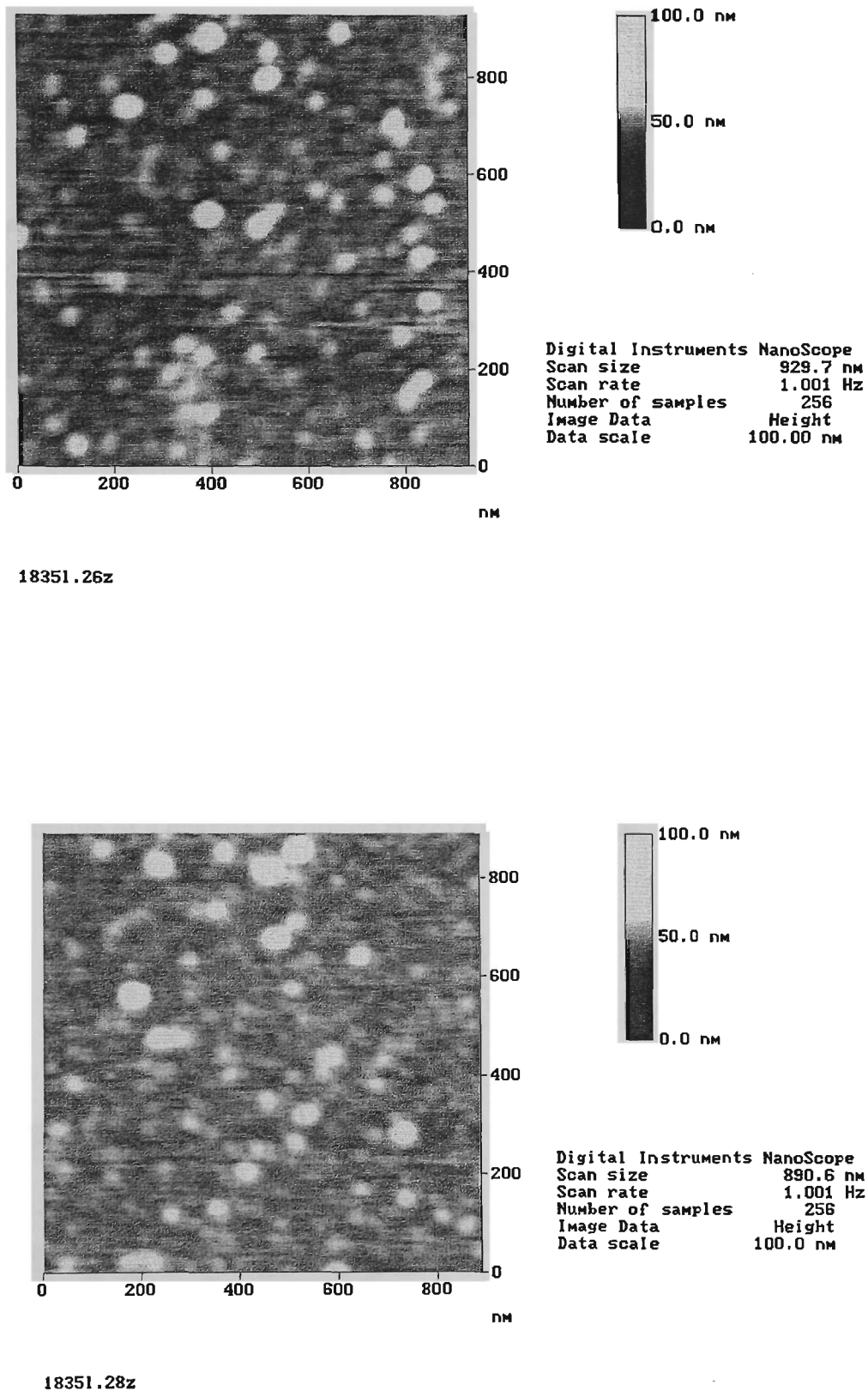

Fig. 3.2.2.1: AFM 2D image of a heavily Pb doped Bi2212 single crystal showing lines with an approximate thickness of 20 nm. The upper image is obtained with a tip scan angle = 90°, and the lower image is obtained with a scan angle = 0°.

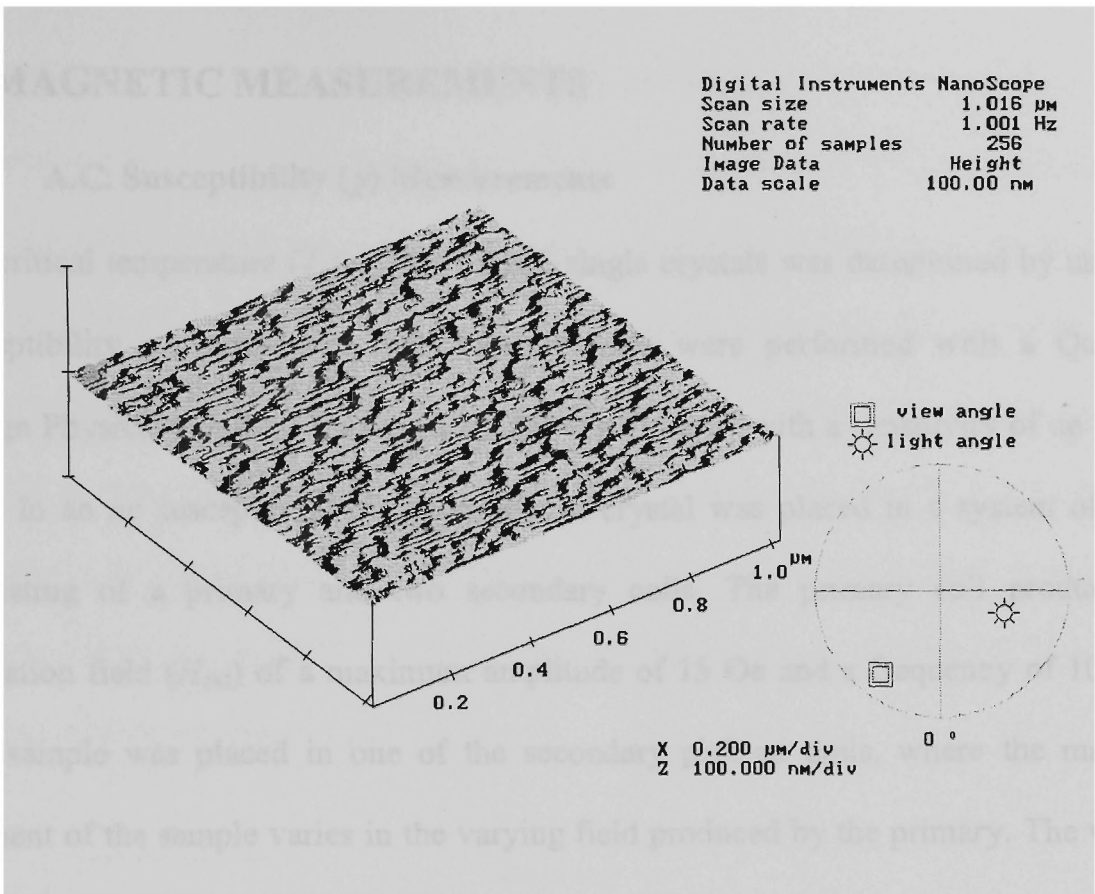

Fig. 3.2.2.2: AFM 3D image of a heavily Pb doped Bi2212 single crystal.

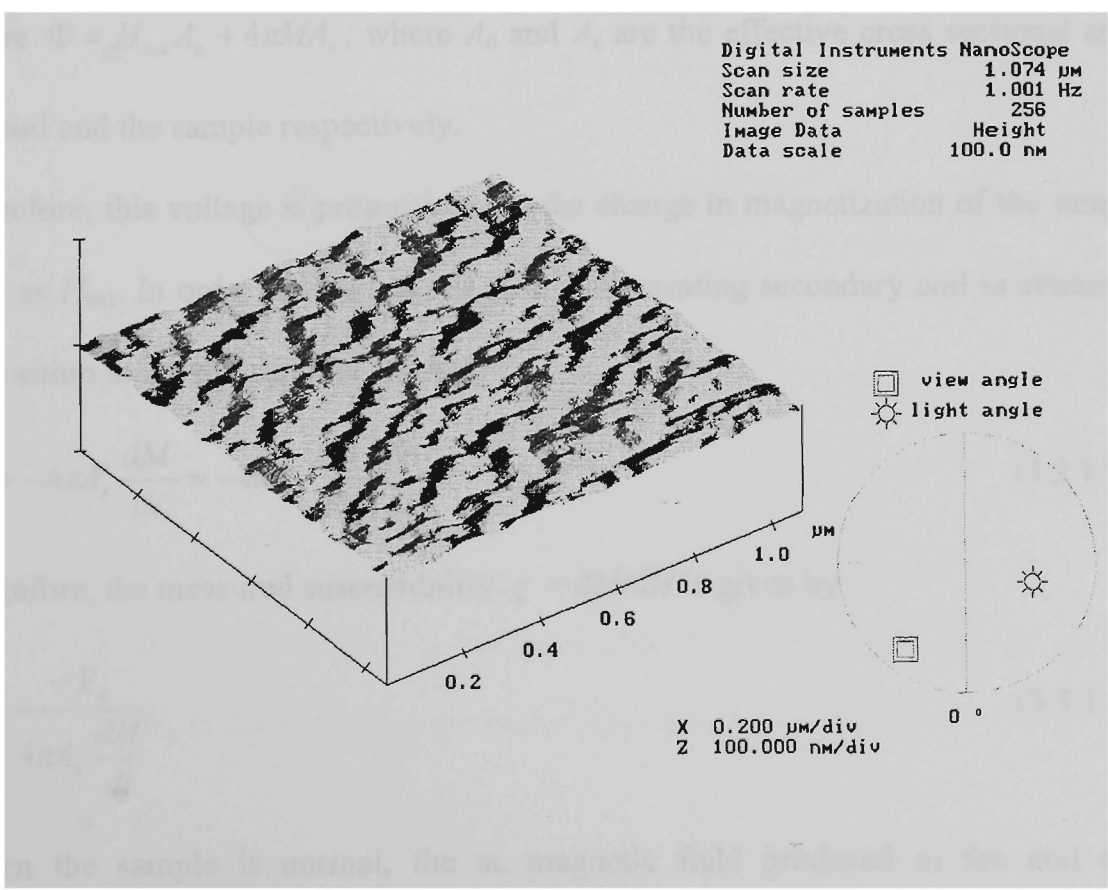

Fig. 3.2.2.3: Three-dimensional AFM image of an Fe doped Bi2212 (y = 0.016) single crystal.

3.3 MAGNETIC MEASUREMENTS

3.3.1 A.C. Susceptibility (χ) Measurements

The critical temperature (T_c) of the Bi2212 single crystals was determined by using *ac* susceptibility measurements. The measurements were performed with a Quantum Design Physical Property Measurement System (PPMS) with a sensitivity of up to 10^{-8} emu. In an *ac* susceptibility measurement, a crystal was placed in a system of coils, consisting of a primary and two secondary coils. The primary coil produces an excitation field (H_{ext}) of a maximum amplitude of 15 Oe and a frequency of 10 KHz. The sample was placed in one of the secondary pick-up coils, where the magnetic moment of the sample varies in the varying field produced by the primary. The voltage of the pick up coil varies as:

$$V_\phi = -\frac{d\Phi}{dt} \qquad (3.3.1.1)$$

where $\Phi = H_{ext}A_c + 4\pi MA_s$, where A_c and A_s are the effective cross sectional areas of the coil and the sample respectively.

Therefore, this voltage is proportional to the change in magnetization of the sample, as well as H_{ext}. In order to eliminate H_{ext}, a compensating secondary coil is connected in opposition to the pick up coil, so that

$$V_\phi = -4\pi A_s \frac{dM}{dt} = -4\pi A_s \frac{dM}{dH}\frac{dH}{dt} \qquad (3.3.1.2)$$

Therefore, the measured susceptibility $\chi = dM/dH$ is given by

$$\chi = \frac{-V_\phi}{4\pi A_s \dfrac{dH}{dt}} \qquad (3.3.1.3)$$

When the sample is normal, the ac magnetic field produced in the coil extends throughout the sample. As the sample becomes superconducting, the *ac* field is

excluded from the interior by superconducting shielding currents that produce a field in the direction opposite to the applied field. This drastic change in the field profile gives a very significant change in the voltage across the coil, and this change can be detected by a Lock-In Amplifier. A schematic diagram of the apparatus for the *ac* susceptibility measurements is given in Fig.3.3.1.1. The temperature at which this change occurs is the critical temperature of the sample (T_c). With this procedure, T_c = 69 K was obtained for heavily Pb doped single crystal, see Fig. 3.3.1.2a. The Bi2212 single crystals with iron content $y = 0$, $y = 0.005$, $y = 0.016$ and $y = 0.022$ had T_c = 88.5, 82.25, 73 and 65.5 K, respectively, see Fig. 3.3.1.2.

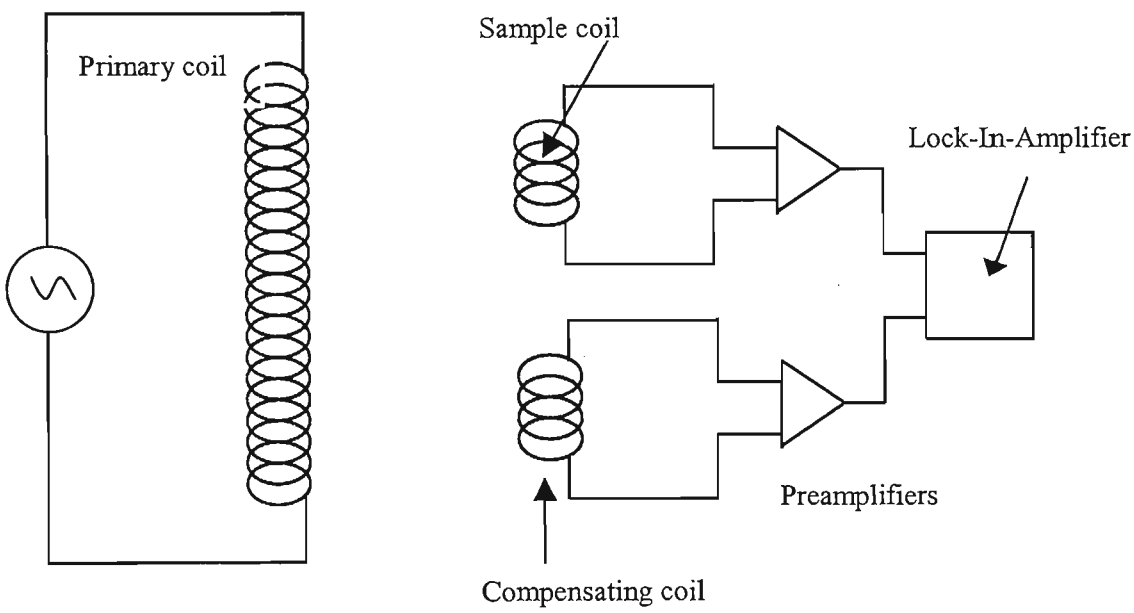

Fig. 3.3.1.1: Schematic diagram showing a mutual inductance technique for measuring the superconducting transition temperature.

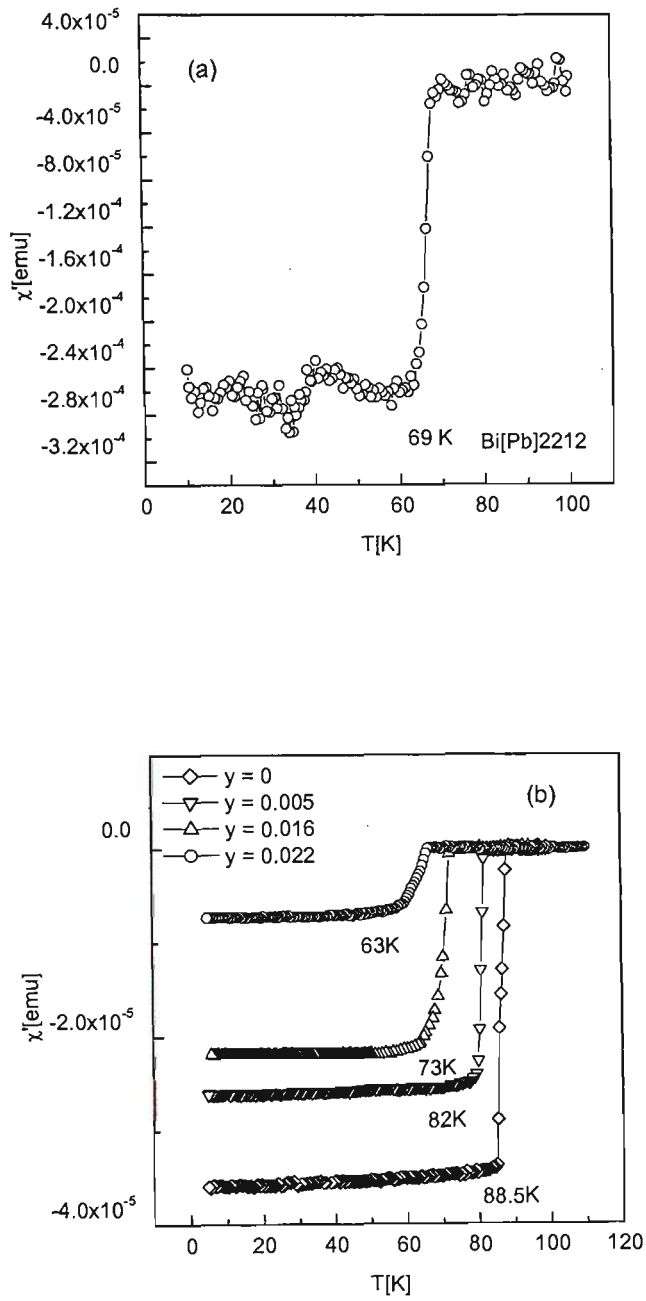

Fig.3.3.1.2: The real part of the *ac* susceptibility χ as a function of temperature for (a) heavily Pb doped Bi2212 single crystal and (b) Bi2212 single crystals with iron content y = 0, y = 0.005, y = 0.016 and y = 0.022.

3.3.2 DC Magnetization Measurement

Two magnetometers were employed to measure the *dc* magnetization for the crystals. They were a Quantum Design Physical Property Measurement System (PPMS) and an Vibrating Sample Magnetometer (VSM). In the *dc* magnetization measurements, the sample moves in a constant magnetic field through the entire detection coil. The detection coil picks up a waveform signal from the sample, as the voltage of the pick-up coil versus the position of the sample. The signal is then fitted with the known waveform signal (voltage versus position) of the calibration sample. One type of the fitting parameters is the magnetic moment of the sample.

In the *dc* magnetization measurements, magnetic hysteresis loops, magnetic relaxation measurements and Field Cooled and Zero Field Cooled (ZFC) magnetization versus temperature measurements were performed on our Bi2212 single crystals. The hysteresis loops of the crystals were recorded at different temperatures. From each hysteresis loop, the field of minimum magnetization (H_{min}) between the first and second peaks, the second peak field (H_{peak}), the inflection field (H_{infl}), the irreversibility field (H_{irr}) and the critical current density (J_c) were obtained. Here H_{irr} is defined as the field above which the ascending and descending branches of the magnetization coincide (see Fig. 3.3.2.1), H_{min} is the field at which a minimum magnetization between the first and second peak occurs in the $M(H)$ curve, and H_{infl} is the field at which an inflection in $M(H)$ curve occurs on the low-field side of the peak.. The irreversible component of the magnetization $M_{irr}(H)$ was obtained from the hysteresis loop, since $M_{irr} = M - M_{eq}$, where M_{eq} was calculated from the ascending M^+ and descending M^- branches of the hysteresis loop using the relation $M_{eq} = (M^+ + M^-)/2$, see Fig. 3.3.2.1. Here, pinning due to surface barrier is not considered otherwise $M_{eq} \neq (M^+ + M^-)/2$. M_{irr} is proportional to the critical current density J_c.

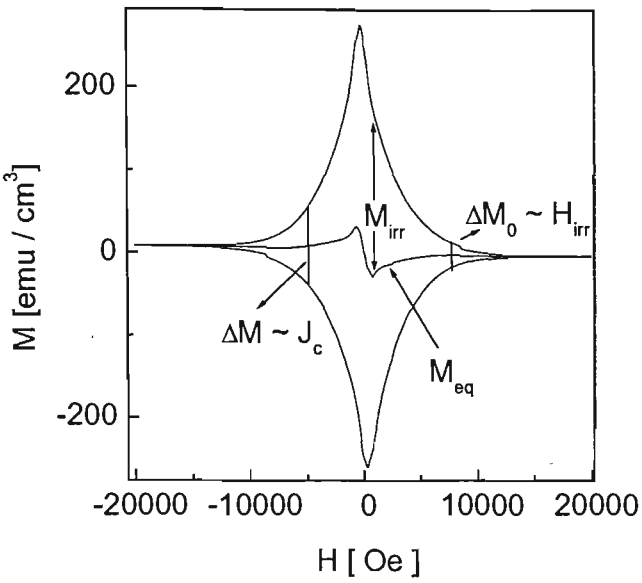

Fig. 3.3.2.1: Magnetic hysteresis loop showing equilibrium magnetization (M_{eq}), height of the magnetic hysteresis loop (ΔM), irreversibility field (H_{irr}) and irreversible magnetization (M_{irr}). H_{irr} was estimated from a height of the magnetic hysteresis loop (ΔM_0).

From the relaxation measurements, the current voltage curve (I-V), normalized relaxation rate (S) and effective activation energy (U_{eff}) were obtained. In the relaxation measurements, a magnetic field (H) several times larger than the first penetration field (H_p) was applied in order to ensure a homogenous flux distribution. The sample magnetization has to be homogeneous because the magnetometer measures an averaged magnetic moment of the crystals. With inhomogeneous magnetization where the geometric and surface barriers are significant, the decay rates vary locally (depending on the local flux gradients), and it is highly questionable what such a relaxation measurement would represent.

In the Zero Field Cooled (ZFC) measurement, the sample was first cooled in zero field from above the critical temperature, then a magnetic field was applied, and the moment as a function of increasing temperature was recorded at a constant applied field. In the Field Cooled (FC) measurement, a magnetic field was first applied above the critical temperature, and the moment as a function of decreasing temperature was measured at a constant applied field.

3.4 Post-Annealing Methods

Oxygen inhomogeneity is always observed in as grown single crystals created using the flux growth method. The oxygen stoichiometry in Bi2212 single crystals plays a major role in determining the critical temperature T_c of the sample [11]. Therefore, in order to get a sharp transition temperature, post-annealing of the crystals at different temperatures and different atmospheres is very important, because it helps oxygen redistribution in the sample. Fig. 3.4.1 shows the critical temperature of pure (y = 0) Bi2212 single crystals with and without heat treatment. The figure shows a wide transition temperature (ΔT = 10K) before heat treatment in y = 0 single crystals. It was found that the temperature and atmosphere of the sample during the heat treatment were very important. For Bi2212 single crystal, the best annealing temperature and atmosphere was 550^0C - 600^0C and 7.5 % oxygen in Argon, where we have obtained a sharp transition.

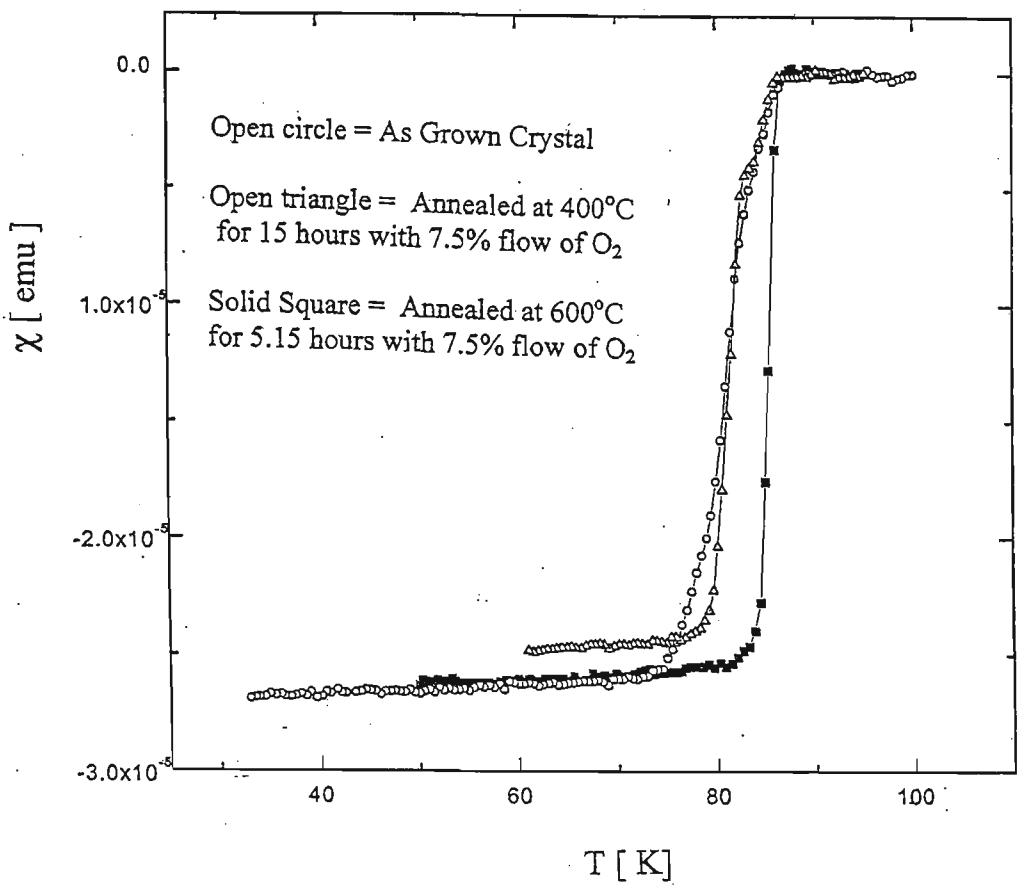

Fig. 3.4.1: Effect of annealing on T_c for Bi2212 single crystal.

3. 5 References for Chapter Three

1. J. Blow, *Chemistry of Superconductor Materials*, T. A. Vanderah ed., Noyes Publications, Park Ridge, NJ, U. S. A., p. 224 (1992).
2. M. Ionescu, V. Murashov and S. X. Dou, *Physica* C **282**, 437 (1997).
3. R. K. Panday, M. Hannan and K. K. Raina, *J. Crystal Growth* **137**, 268 (1994).
4. X. L. Wang, Z. P. Ai, S. X. Shang, H. Wang, M. H. Jiang, H. C. Chen, X. Z. Wang and D. Bauerle, *J. Crystal Growth* **139,** 86 (1994).
5. P. D. Hanad, D. A. Payne, *J. Crystal Growth* **104,** 201 (1990).
6. K. Shighematzu, H. Takei, I. Higashi, K. Hoshino, H. Takahara and M. Aono, *J. Cryst. Growth* **100,** 661 (1990).
7. J. Horvat, X. L. Wang and S. X. Dou, *Physica* C **324,** 211 (1999).
8. X. L. Wang, Ph.D thesis, University of Wollongong (2000).
9. G. D. Gu, G. J. Russell and N. Koshizuka, *J. Crystal Growth* **137,** 472 (1994).
10. Z. Hiroi, I. Chong and M. Takano, *J. Solid State Chem.* **138,** 98 (1998).
11. S. T. Johnson, P. D. Hatton, A. J. S. Chowdhury, J. Gardner, G. Balakrishnan, D. McK. Paul and J. Hodby, *Physica* C **299,** 240 (1998).

CHAPTER FOUR: EXPERIMENTAL RESULTS

4. Experimental Results

$Bi_{2.1}Sr_{1.9}Ca_{1.0}(Cu_{1-y}Fe_y)_2O_{8+\delta}$ single crystals with Fe concentration y = 0, 0.005, 0.016 and 0.022 and $Bi_{2-x}Pb_xSr_2CaCu_2O_{8+\delta}$ single crystals with Pb concentration x =0.34 were used in the measurements. Here y = 0 was a pure Bi2212 single crystal. The dimensions of the Pb doped single crystal were 0.71 × 1.11 × 0.038 mm^3, and it was prepared by flux growth method [1,2]. The iron doped single crystals were prepared by using the floating zone method [3]. The sample's dimensions and critical temperatures are summarized in the table given below.

Sample	Sample's Dimensions (mm^3)	Critical Temperature T_c [K]
$Bi_{2.1}Sr_{1.9}Ca_{1.0}(Cu_{1-y}Fe_y)_2O_x$ [y = 0]	1.95 × 2.10 × 0.116	88.5
$Bi_{2.1}Sr_{1.9}Ca_{1.0}(Cu_{1-y}Fe_y)_2O_x$ [y = 0.005]	1.30 × 2.50 × 0.15	82.25
$Bi_{2.1}Sr_{1.9}Ca_{1.0}(Cu_{1-y}Fe_y)_2O_x$ [y = 0.016]	1.40 × 2.10 × 0.026	73
$Bi_{2.1}Sr_{1.9}Ca_{1.0}(Cu_{1-y}Fe_y)_2O_x$ [y = 0.022]	1.25 × 1.90 × 0.045	65.5
$Bi_{2-x}Pb_xSr_2CaCu_2O_y$ [x = 0.34]	0.71 × 1.11 × 0.038	69

Table 4.1: Dimensions and critical temperatures of pure (y = 0), Fe doped (y = 0.005, 0.016 and 0.022) and heavily Pb doped and Bi2212 single crystals.

The heavily Pb doped Bi2212 single crystal had a critical current density that was almost one order of magnitude larger than that of pure Bi2212 single crystal [4]. This indicated that the heavily Pb doped Bi2212 single crystal had a strong vortex pinning. The main objective of this thesis work is to study the mechanisms behind the strong vortex pinning in the heavily Pb doped Bi2212 single crystals. In this section, we present experimental results that suggest one of the possible reasons for the improved vortex pinning in heavily Pb doped Bi2212 single crystal. In heavily Pb doped Bi2212 single crystal, Pb replaces Bi in between the CuO_2 planes. An improved *c*-axis conductivity has been reported in heavily Pb doped Bi2212 single crystals [5]. For example, a *c*-axis resistivity (ρ_c) of the order of 0.2 Ωcm has been reported in heavily Pb doped single crystal, while $\rho_c \sim 5$ Ωcm has been reported for pure Bi2212 single crystal [5]. Thus, improved *c*-axis conductivity has been proposed as responsible for the enhanced vortex pinning in heavily Pb doped Bi2212 single crystals. Magnetic measurements in this thesis show that the vortex dynamics in heavily Pb doped Bi2212 single crystal is in agreement with the transport measurements. In order to support this argument further, a study of vortex pinning behaviour was also made in Fe doped Bi2212 single crystals. The Fe in Bi2212 single crystals replaces Cu in the CuO_2 plane and does not improve the c axis conductivity [6]. Unlike heavily Pb doped single crystals, the Fe doped Bi2212 single crystals have almost the same *c*-axis parameter as does the pure Bi2212 single crystal, see Table 3.2.1.2. This suggested that the vortex pinning mechanism for Fe doped crystals should be different from that for heavily Pb doped Bi2212 single crystals. The experimental results given below will show different vortex pinning behaviour in Fe and heavily Pb doped Bi2212 single crystals. In the following, magnetic hysteresis and magnetic relaxation measurements have been

presented for pure (y = 0), iron doped (y = 0.005, 0.016 and 0.022) and heavily Pb doped Bi2212 single crystals.

4.1 Magnetic Hysteresis Loop

Magnetic hysteresis loop measurements were performed using an Oxford Instruments Vibrating Sample Magnetometer (VSM) with applied field parallel to the c axis of the crystals. In the hysteresis loop measurements, the magnetic fields were changed at a rate of 20 Oe per second, and the data were recorded at different temperatures. All Bi2212 single crystals used in the measurements showed second magnetization peak (peak effect) in the hysteresis loop. Comparative studies of the second magnetization peak have been made for pure (y = 0), Fe doped (y = 0.005, 0.016, 0.022) and heavily Pb doped Bi2212 single crystals. A minimum field, H_{min}, (the field at which the magnetization attains a minimum, between the first and secondary magnetization peaks) and an inflection field, H_{infl}, (the field at which there is a peak in the derivative of magnetization with respect to field, dM/dH between the H_{min} and H_{peak}), were obtained from the hysteresis loop. The results for H_{min} and H_{infl} are presented for pure, iron doped and heavily Pb doped single crystals. The hysteresis loops are also used to obtain the critical current density J_c using the Bean relation [7,8]. J_c is proportional to the irreversible part of the magnetization $M_{irr} = |M-M_{eq}|$. The equilibrium magnetization M_{eq} is obtained as $M_{eq} = (M_- + M_+)/2$, where M_- and M_+ are the branches of the hysteresis loop corresponding to decreasing and increasing applied field, respectively. The irreversibility field H_{irr} at different temperatures for all four crystals is also obtained from the measured magnetization loop.

4.1.1 Critical Current Density

In this section, results on the field dependence of the normalized critical current density (J_c/J_{c0}) have been presented for pure (y = 0), iron doped (y = 0.005, 0.016 and 0.022) and heavily Pb doped Bi2212 single crystals. The critical current density J_c is obtained by using the Bean's relation, which for the crystals used in the measurements can be written as:

$$J_c = \frac{20\Delta M}{\left[a\left(1-\frac{a}{3b}\right)\right]}, \qquad (4.1.1)$$

where J_c is in A/cm^2, $\Delta M = |M^- - M^+|$ is the width of hysteresis loop measured in emu/cm^3 and a and b are the lateral dimensions of the sample ($b > a$), measured in cm.

Figure 4.1.1.1 shows the critical current density J_c as a function of temperature T at an applied field H = 1000 Oe for pure (y = 0) and heavily Pb doped Bi2212 single crystals. The magnetic field H was applied parallel to the c-axis. A dramatic upward shift of the $J_c(T)$ for the Pb doped single crystal indicates strong vortex pinning in the crystal, as compared with the pure Bi2212 single crystal. Fig. 4.1.1.2 shows quantitatively the same result for J_c at reduced temperature T/T_c. The normalized critical current density J_c/J_{c0} versus H at T = 30K for pure (y = 0) and heavily Pb doped Bi2212 single crystals has been presented in Fig. 4.1.1.3. The strong field dependence of J_c/J_{c0} in pure Bi2212 single crystal at higher temperatures (T = 30 K) and higher fields may be due to the large anisotropy of Bi2212, where thermal excitation easily unpins individual pancake vortices from the pinning sites. Fig. 4.1.1.4 also shows quantitatively the same result for the field dependence of J_c/J_{c0} at T/T_c = 0.3. However, at 20K, Fig. 4.1.1.5 shows that both pure and heavily Pb doped crystals have a weaker field dependence of J_c/J_{c0}, indicating strong vortex pinning in pure Bi2212 single crystals below 20K. The critical

current density for heavily Pb doped Bi2212 single crystal measured at $T = 0.3\ T_c$ and H = 1000 Oe is shown in Table 4.1.1.1.

Name of Sample	Critical current density (J_c [A/cm^2]) at H = 1000 Oe and $T = 0.3T_c$
$Bi_{2.1}Sr_{1.9}Ca_{1.0}(Cu_{1-y}Fe_y)_2O_x$ [y = 0]	3.9×10^4
$Bi_{2.1}Sr_{1.9}Ca_{1.0}(Cu_{1-y}Fe_y)_2O_x$ [y = 0.005]	3.0×10^4
$Bi_{2.1}Sr_{1.9}Ca_{1.0}(Cu_{1-y}Fe_y)_2O_x$ [y = 0.016]	1.9×10^4
$Bi_{2.1}Sr_{1.9}Ca_{1.0}(Cu_{1-y}Fe_y)_2O_x$ [y = 0.022]	1.3×10^4
$Bi_{2-x}Pb_xSr_2CaCu_2O_y$ [x = 0.34]	5.6×10^4

Table 4.1.1.1: Critical current density measured at $T = 0.3T_c$ and H = 1000 Oe for pure (y = 0), iron doped (y=0.005, 0.016 and 0.022) and heavily Pb doped Bi2212 single crystals.

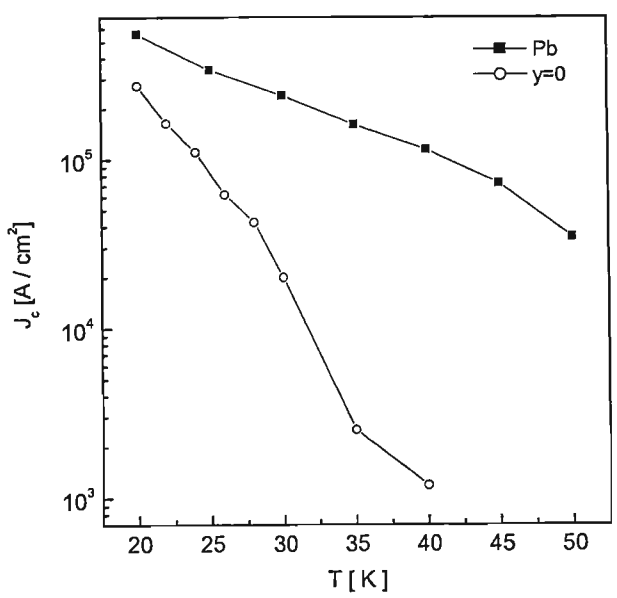

Figure 4.1.1.1: Critical current density J_c as a function of temperature T measured at H = 1000 Oe for pure (y = 0) and heavily Pb doped Bi2212 single crystals.

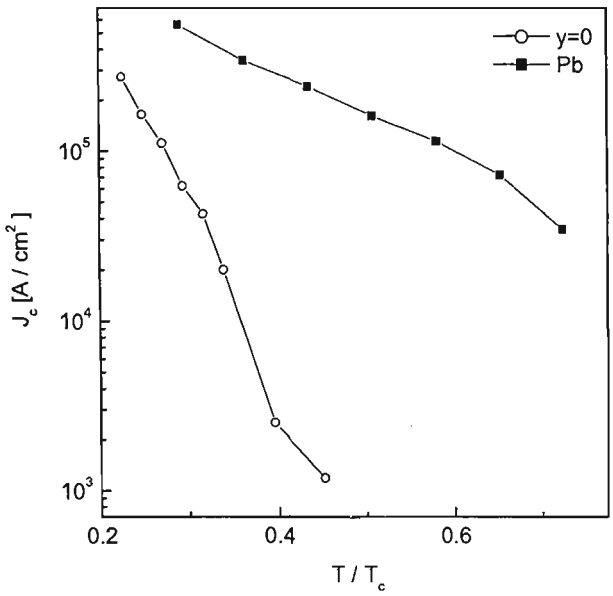

Figure 4.1.1.2: Critical current density J_c vs reduced temperature T/T_c measured at H = 1000 Oe for pure (y = 0) and heavily Pb doped Bi2212 single crystals.

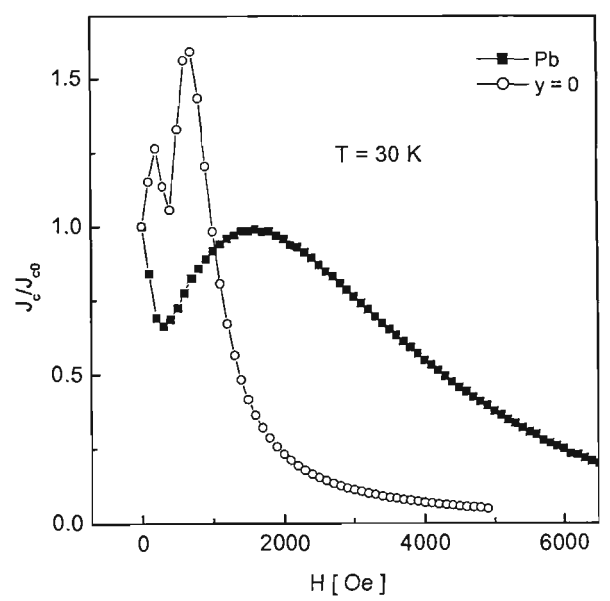

Figure 4.1.1.3: Normalized critical current density J_c/J_{c0} as a function of applied field H measured at T = 30 K for pure (y = 0) and heavily Pb doped Bi2212 single crystals.

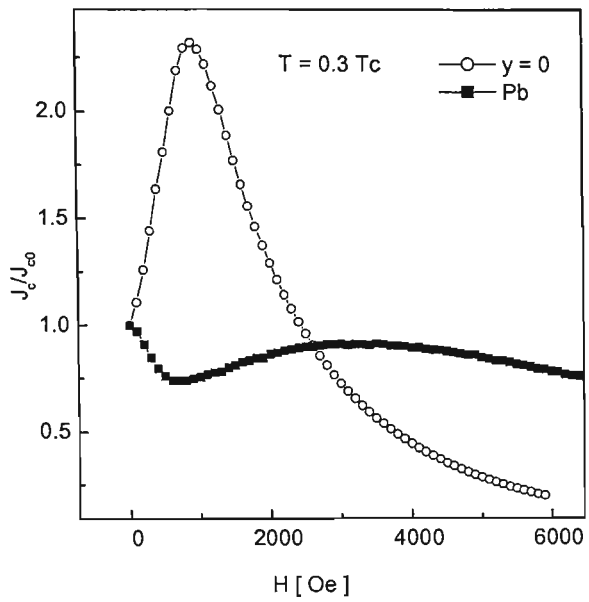

Figure 4.1.1.4: Normalized critical current density J_c/J_{c0} versus applied field H measured at reduced temperature $T = 0.3T_c$ for pure (y = 0) and heavily Pb doped Bi2212 single crystals.

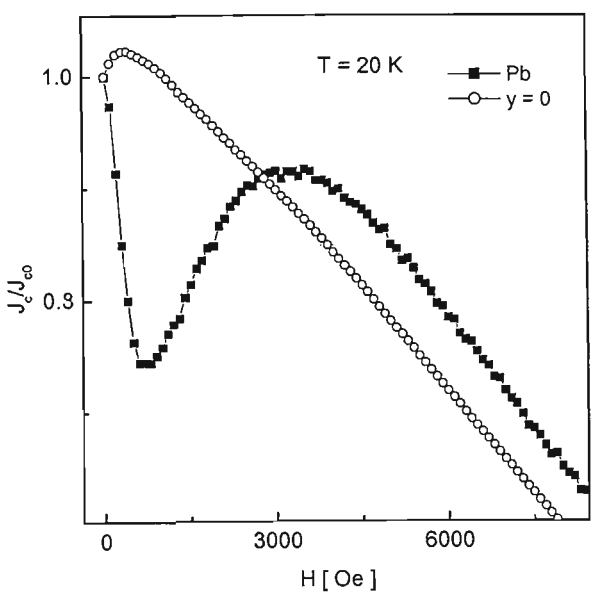

Figure 4.1.1.5: J_c/J_{c0} as a function of applied field H measured at $T = 20$K for y = 0 and heavily Pb doped Bi2212 single crystals.

The normalized critical density (J_c/J_{c0}) values at T = 24K for Bi2212 single crystal with Fe content y = 0, 0.005, 0.016 and 0.022 are shown in Fig. 4.1.1.6. The large J_c/J_{c0} for y = 0.005 crystal reflects an improved vortex pinning in the crystal. The enhanced pinning for y = 0.005 crystal was possibly due to the low concentration of Fe atoms that act as point-like pinning centers. However, the critical current density was not improved by doping Bi2212 single crystal with a large Fe concentration, see J_c/J_{c0} for y = 0.016 and 0.022 crystals in Fig. 4.1.1.6. Figure 4.1.1.7 also gives quantitatively the same result for J_c/J_{c0} at reduced temperature $T = 0.3T_c$ as for 24K (Fig. 4.1.1.6), suggesting that the different values of T_c for these samples do not affect the results. The J_c values for y = 0, 0.005, 0.016 and 0.022 Bi2212 single crystals at reduced temperature $T = 0.3T_c$ and applied field H = 1000Oe are given in the Table 4.1.1.1.

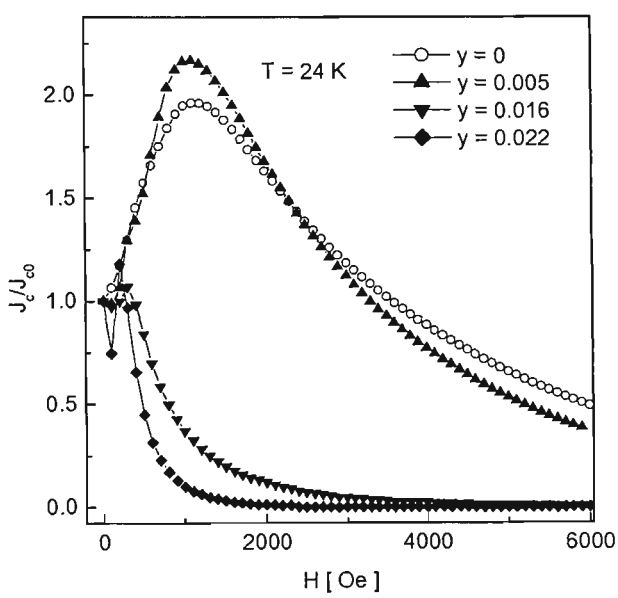

Figure 4.1.1.6: Normalized critical current density J_c/J_{c0} versus applied field H measured at T = 24K for pure (y = 0), and iron doped (y= 0.005, 0.016, 0.022) Bi2212 single crystals.

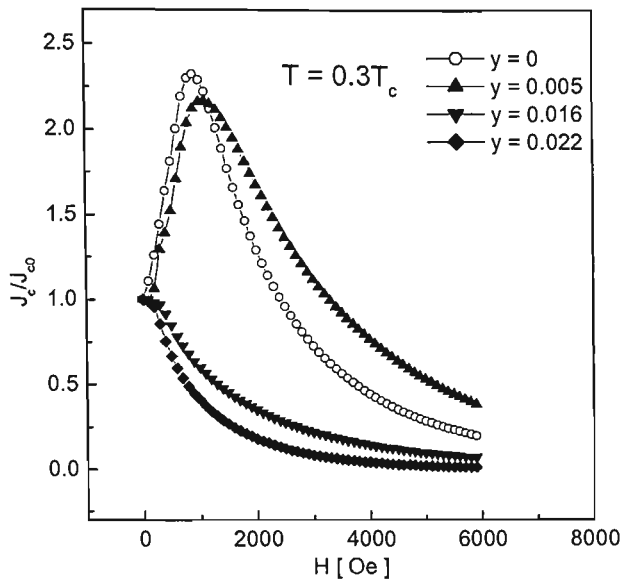

Figure 4.1.1.7: J_c/J_{c0} as a function of applied field H obtained at reduced temperature $T = 0.3T_c$ for pure (y = 0) and iron doped (y = 0.005, 0.016, 0.022) Bi2212 single crystals.

4.1.2 Irreversibility Line

If the magnetization is measured in increasing and decreasing fields, the two data sets in the hysteresis curve are observed to coincide above a field H_{irr}, known as the irreversibility field. The irreversibility field, H_{irr}, separates the irreversible magnetization from the reversible magnetization. For the crystals used in the measurements, the irreversibility field was derived from the hysteresis loop. The H_{irr} was estimated from a region where the two branches of hysteresis loop corresponding to the ascending and descending fields merged into one $M(H)$ curve. The magnetic hysteresis width (ΔM= 18 emu/cm^3), used for defining the irreversibility field, was the same for all the samples. This magnetization width was employed as a reference to estimate H_{irr} in other hysteresis loops measured at different temperatures. Figs. 4.1.2.1a and 4.1.2.1b show the irreversibility field for y = 0, 0.005, 0.016 and 0.22 single crystals and for heavily Pb doped Bi2212 single crystals. The irreversibility field, H_{irr}, for the y = 0 crystal at 22K was 25340 Oe and at 30K, it was 2081 Oe. This indicated a large reduction in the hysteresis loop with increasing temperatures. One of the reasons for the reduction of the hysteresis loop is due to the large anisotropy of pure Bi2212 single crystals, where thermal fluctuations easily unpin pancake vortices from pinning centers. The H_{irr} for y = 0.005 crystal at T = 22 K was 14587 Oe and at T = 30K, it was 990 Oe, also showing a large reduction of the hysteresis loop. The anisotropy is not improved in Bi2212 single crystals with Fe doping since Fe ions sit in the CuO_2 plane. However, in heavily Pb doped Bi2212 single crystal, anisotropy was reported to decrease significantly due to increased c axis conductivity [5]. The H_{irr} for heavily Pb doped single crystal at T = 25 K was 23000 Oe and at 30 K, it was 13928 Oe. The strong upward shift of the H_{irr} (or enlargement of the irreversible regime) with heavy Pb doping is related to the strong vortex pinning in the crystal. The improved c-axis

coupling is proposed for the improved vortex pinning in the heavily Pb doped single crystals.

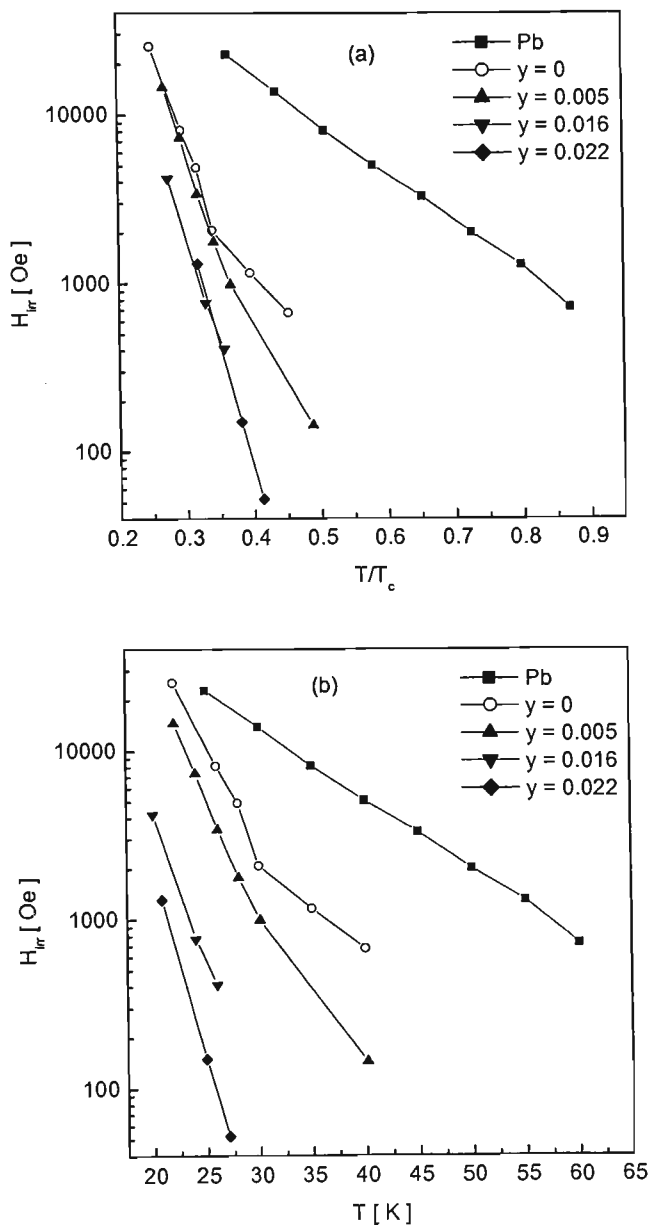

Figure 4.1.2.1: Top figure (a) shows irreversibility field, H_{irr}, as a function of reduced temperature for pure (y = 0), iron doped (y = 0.005, 0.016, 0.022) and heavily Pb doped Bi2212 single crystals (top). The same figure on an absolute temperature scale is shown in the bottom (b).

4.1.3 Second Magnetization Peak

The strong second magnetization peak (peak effect) in heavily Pb doped Bi2212 single crystal reflects enhanced vortex pinning in this material. Fig. 4.1.3.1 shows the second magnetization peaks for heavily Pb doped single crystal at temperatures T = 20, 25, 30, 35, 40, 45, 50, 55 and 60 K. The second peak in the heavily Pb doped single crystal was observed close to the critical temperature, see Fig. 4.1.3.2. However, the second magnetization peaks in pure and iron doped Bi2212 single crystals were observed only up to T = 40K. The height of the magnetic hysteresis loops for pure (y = 0) and iron doped (y = 0.005, 0.016, 0.022) single crystals measured at T = 24 K is shown in Fig. 4.1.3.3. At or below 20 K, the second peaks are not clearly seen in Bi2212 single crystals with y = 0, 0.005, 0.016 and 0.022 (see Fig. 4.1.3.4). Fig. 4.1.3.4 shows no clear peaks above 40 K in pure and iron doped single crystals. In Y123, a strong peak persisting up to T_c has been reported [9]. The magnetic phase diagram (H-T) for Y123 crystal showed a vortex solid phase over a wide range of fields and temperatures. This was because of the lower anisotropy of the materials where vortices are of the 3D type. In pure Bi2212 single crystals, most of the $H-T$ vortex phase diagram was dominated by the presence of the vortex liquid phase [10]. This was due to their large anisotropy, which was responsible for weak inter-layer 2D pancake vortex coupling [10]. The effects of thermal excitations on these 2D pancake vortices were very strong, as compared to 3D vortex lines, so that 2D vortices were easily unpinned. In order to reduce thermal fluctuations of the 2D vortices, a strong inter-layer coupling between them was desirable. It was pointed out that an observed increase in vortex pinning due to columnar defects in Bi2212 single crystals, introduced by heavy ion irradiation, was caused by the Josephson coupling between 2D pancake vortices [11]. Thus coupled vortices formed 3D vortex lines. Recently, T. Motohashi et al. have reported that lead in

Bi2212 single crystal increased c-axis conductivity by significantly reducing the resistivity anisotropy parameter $\gamma^2 = \rho_c/\rho_{ab} \approx 10^3$ [5]. This suggested that the enhanced pinning, as reflected from the strong second peak in the heavily Pb-doped single crystals, was due to improved c axis coupling where the vortices are of 3D type, similar to the vortices in Y123. It is believed that the vortex dimensionality plays an important role as the origin of the peak effect. In section 5.1, a relation between the peak effect and the vortex dimensionality has been presented.

Fig. 4.1.3.3 shows large peaks for single crystals with y = 0 and y = 0.005 at 24 K, as compared with those for y = 0.016 and 0.022 single crystals. Below H = 2500Oe, the y = 0.005 crystal has a large magnetization loop, indicating strong vortex pinning in comparison with pure Bi2212 crystals, see Fig. 4.1.3.3. One of the possible causes for this improved pinning is that a small Fe concentration might introduce point-like pinning centers in the crystals. However, for H > 2500Oe, Fig. 4.1.3.3 shows a strong field dependence of the magnetization for y = 0.005 crystals. This indicated that these defects are not strong enough to pin vortex bundles. Large Fe content crystals (y = 0.016 and 0.022) have a much narrower hysteresis loops than crystals with y=0.005, indicating weaker vortex pinning, see Fig. 4.1.3.3.

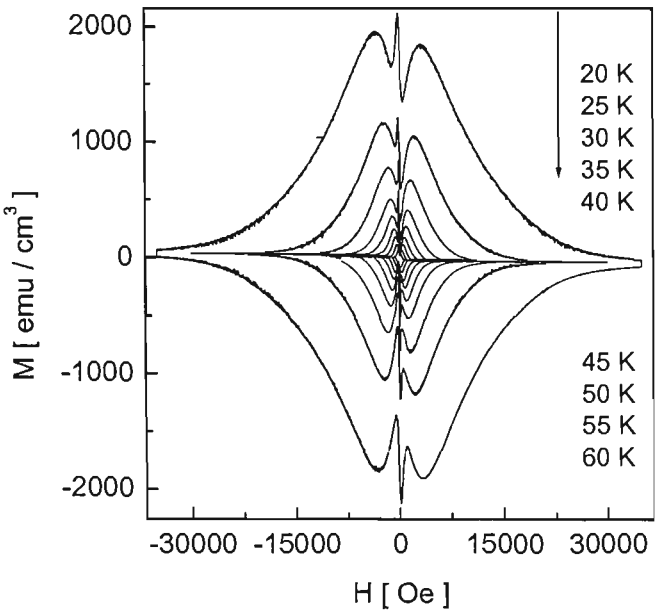

Fig. 4.1.3.1: The measured magnetization loops for a heavily lead doped single crystal at temperatures T = 20, 25, 30, 35, 40, 45, 50, 55 and 60 K with an applied field parallel to c axis.

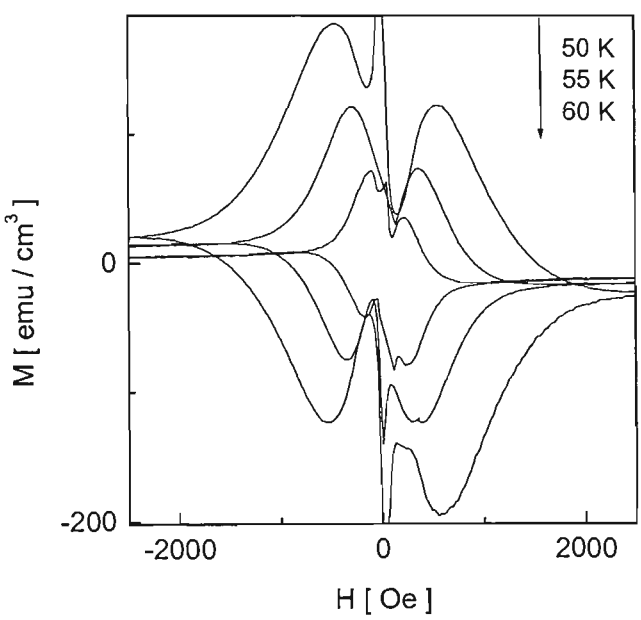

Fig 4.1.3.2: Magnetic hysteresis loops showing the second peak in heavily Pb doped single crystal at temperatures T = 50, 55 and 60 K.

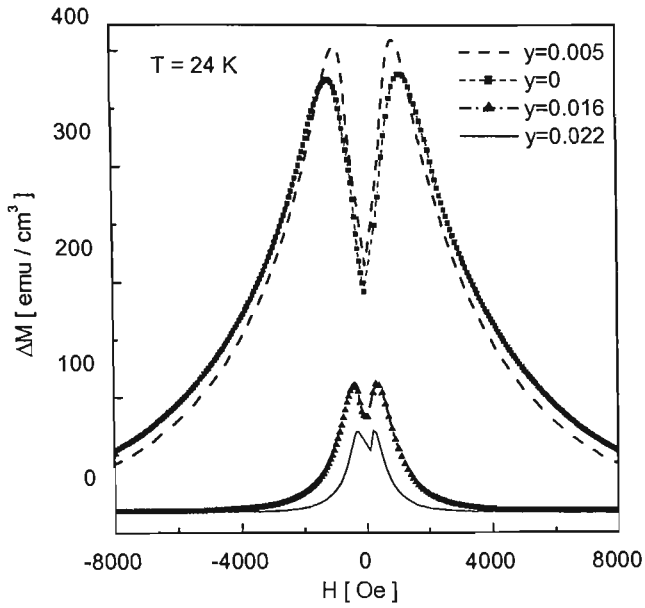

Fig. 4.1.3.3: Height of the magnetic hysteresis loop for pure (y = 0) and iron doped (y = 0.005, 0.016, 0.022) Bi2212 single crystal measured at temperature $T = 24$ K with an applied field parallel to the c axis.

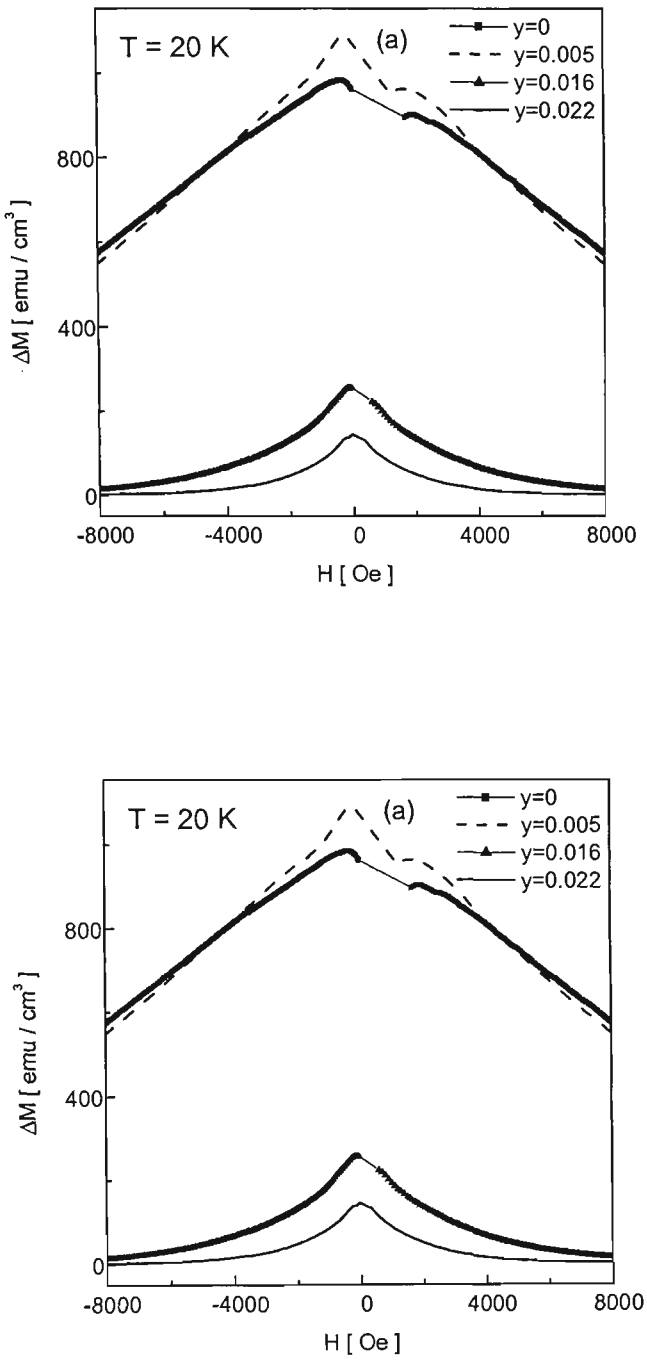

Fig. 4.1.3.4: The height of the hysteresis loops for y = 0, 0.005, 0.016 and 0.022 Bi2212 single crystal at (a) T = 20 K and (b) 40 K with an applied field parallel to the c axis.

In the vortex solid phase, the presence of quenched disorder and its interplay with thermal fluctuations appears to cause two distinctly resolved vortex solid phases: a weakly (elastically) disordered quasi-lattice (Bragg glass) and a highly (plastically) disordered solid phase. An order-disorder transition line, H_{dis}, separates these two different solid phases [12]. Generally, three characteristic fields: H_{peak}, H_{min} and H_{infl} have been reported to denote the order-disorder line in Y123 and Bi2212 single crystals [9, 12-17]. Here, H_{peak} is the field that corresponds to a maximum magnetization point in the second magnetization peak of an $M(H)$ loop, H_{min} is the field that corresponds to the minimum magnetization point between the first and second magnetization peaks, and H_{infl} is the field that corresponds to the inflection magnetization points on the low-field side of the second peak.

In this thesis, values for H_{peak} were estimated from the second magnetization peak of the magnetic hysteresis loops. It is difficult to choose an exact point for the H_{peak} because the second magnetization loop is broadly spaced in the hysteresis loop. Thus there is always an uncertainty in choosing the correct value for H_{peak}. The uncertainties were estimated by considering the shape of hysteresis loop around each peak in $M(H)$ loops. H_{infl} were estimated from the peak in dM/dH of $M(H)$ loop. H_{min} were estimated from a minimum magnetization point between the first and second magnetization peaks. Uncertainties were estimated also for H_{infl} and H_{min}.

Fig. 4.1.3.5a shows the temperature dependence of H_{peak}, for Bi2212 single crystals with iron content y = 0, 0.005, 0.016 and 0.022. A decrease of the H_{peak} with temperature is seen for all the crystals. H_{peak} for y = 0 and y = 0.005 single crystals is very large in

comparison with y = 0.016 and 0.022 crystals. A similar decrease of H_{peak} with temperature was observed for a heavily Pb doped single crystal, see Fig. 4.1.3.5b.

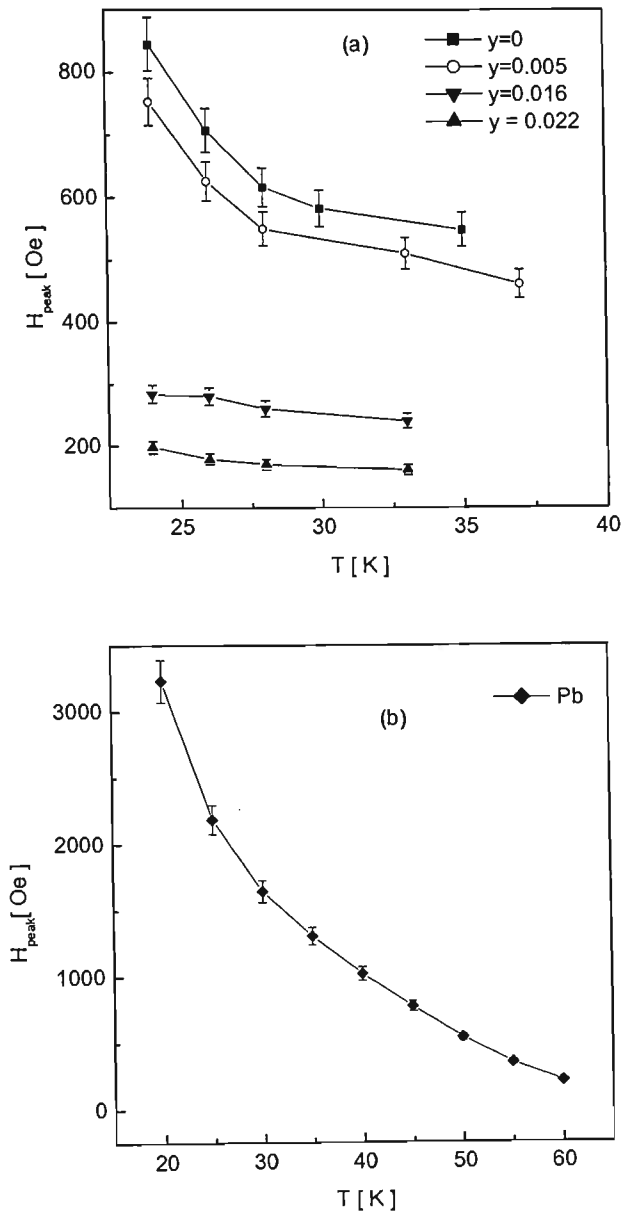

Fig. 4.1.3.5: The second magnetization peak as a function of temperature for (a) pure (y=0) and Fe doped (y = 0.005, 0.016, 0.022) single crystals and (b) heavily Pb doped Bi2212 single crystals. Vertical lines are uncertainties in choosing the second peak.

An increase of H_{min} was observed for all iron doped Bi2212 single crystals. Fig. 4.1.3.6 shows H_{min} as a function of T for y = 0 and y = 0.016 crystals. However, in heavily Pb doped single crystals, the figure shows a decrease of H_{min} with T.

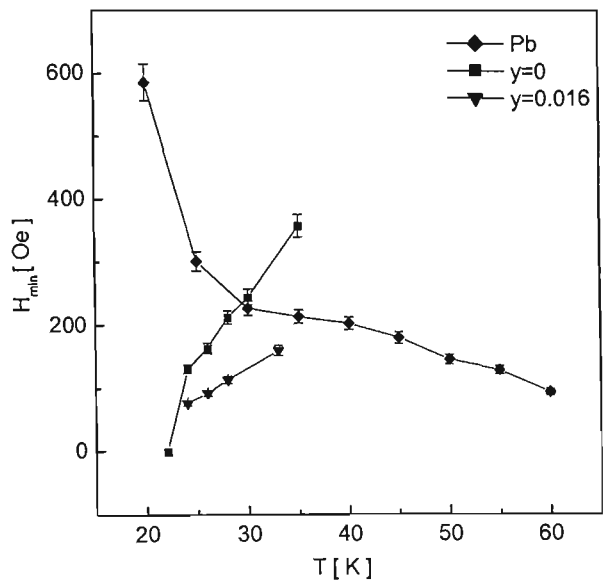

Fig.4.1.3.6: The minimum field H_{min} as a function of temperature T for pure (y = 0), iron doped (y = 0.016) and heavily Pb doped Bi2212 single crystals. The vertical line represents uncertainties of the value of H_{min}.

The remaining characteristic field, H_{infl}, has also been used to study H_{dis}. Figures 4.1.3.7a and 4.1.3.7b show dM/dH as a function of the applied field H for pure (y = 0) and iron doped (y = 0.016) single crystals. The peak in dM/dH occurs at a field H = H_{infl}, i. e. at an inflection point of the second peak in the hysteresis loop. Figures 4.1.3.7a and 4.1.3.9 show the temperature independence of H_{infl} for a pure single crystal. This agrees with the temperature independence of H_{dis} for pure Bi2212 single crystals. H_{infl} for y = 0 was observed at 420 Oe. A similar temperature independence of H_{infl} has been observed in all the iron doped Bi2212 single crystals. The values of H_{infl} for single crystals with y= 0.005, y = 0.016 and y = 0.022 were, respectively 350 Oe, 185 Oe and 170 Oe. However, in heavily Pb doped single crystal, H_{infl} was observed to decrease with temperature, see Fig. 4.1.3.8a,b and Fig. 4.1.3.9.

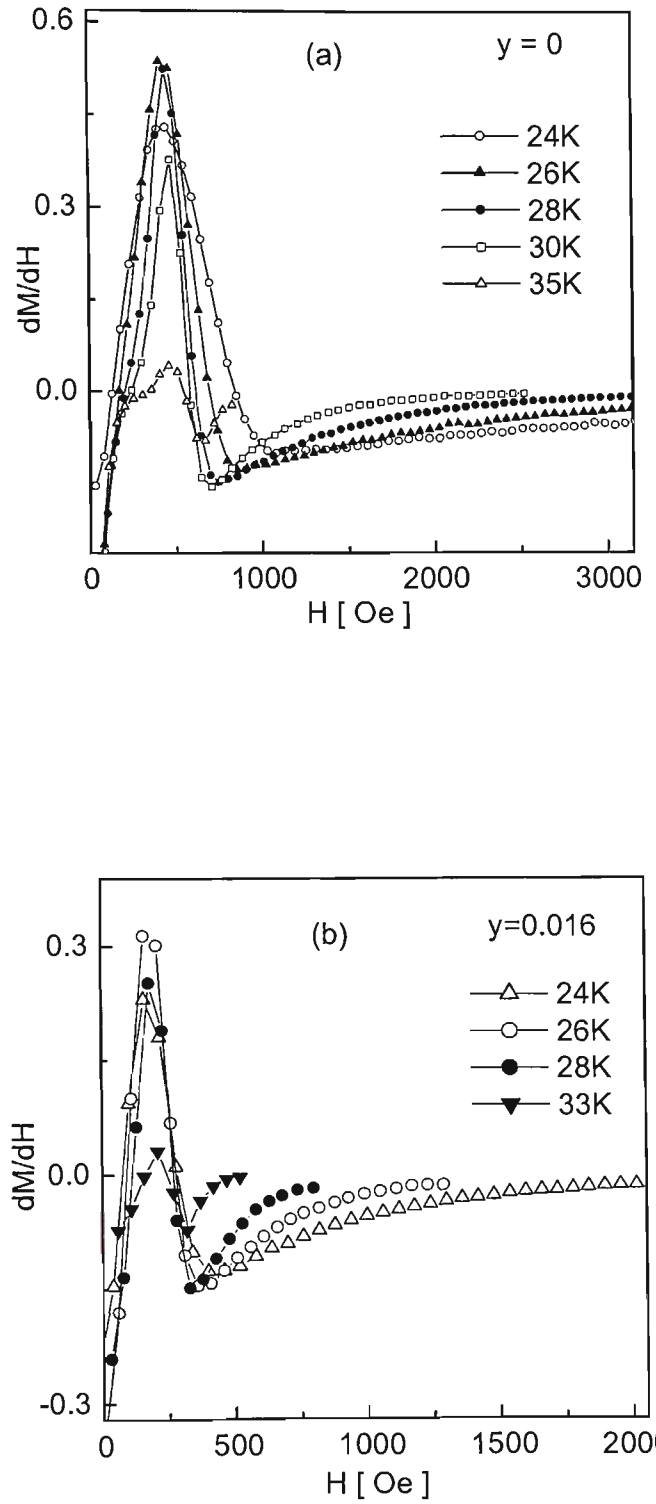

Fig. 4.1.3.7: H_{infl} vs temperature for (a) pure (y=0) Bi2212 single crystal (b) iron doped (y = 0.016) single crystals.

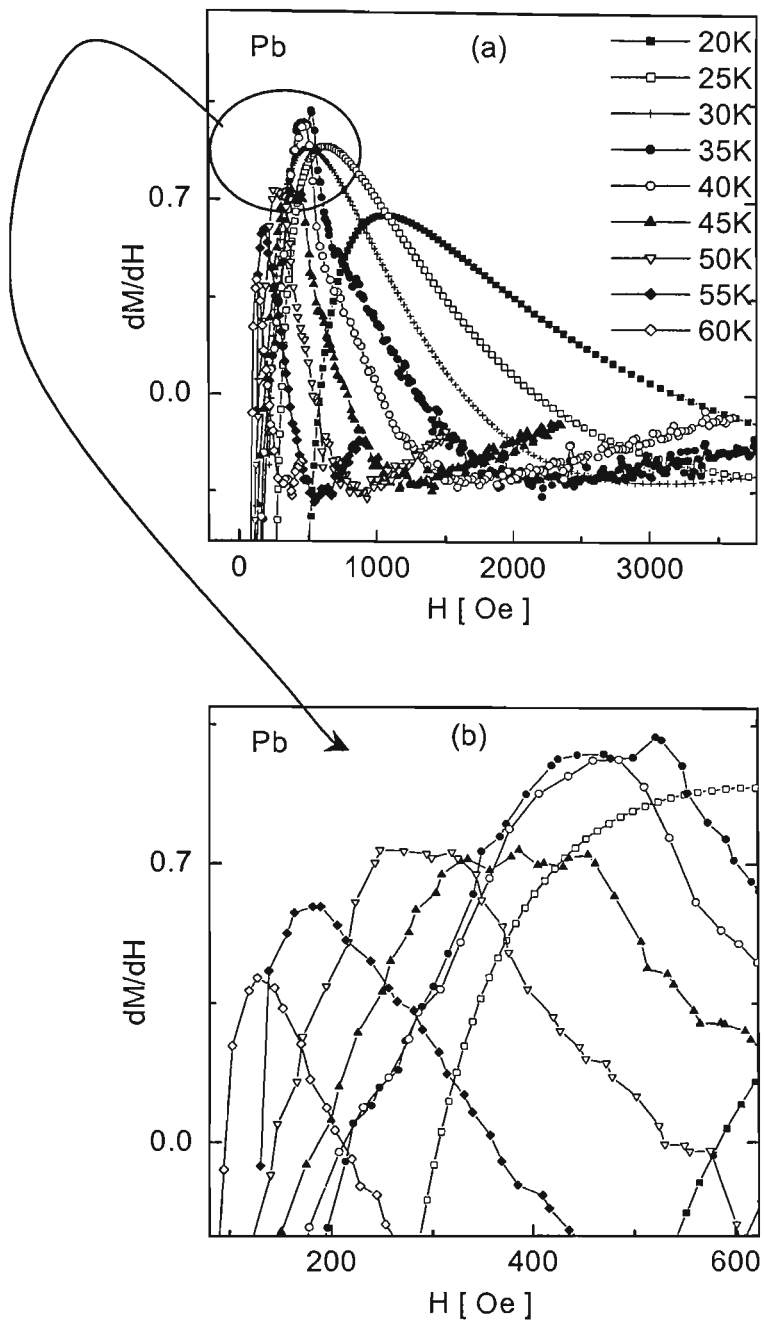

Fig. 4.1.3.8: H_{infl} vs temperature for (a) heavily Pb doped Bi2212 single crystal and (b) an enlarged portion indicated by the circle in (a).

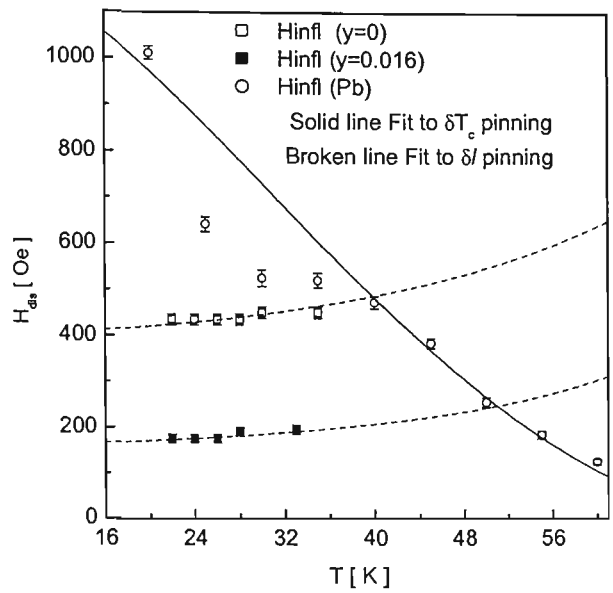

Fig. 4.1. 3.9: $H_{dis} \approx H_{infl}$ vs T for pure Bi2212 single crystal (open squares), Fe doped (y = 0.016) Bi2212 single crystals (filled squares) and heavily Pb doped Bi2212 single crystal (open circles). The solid line is obtained using the relation $H_{dis}(T) \propto \xi(T)^{-3}$ for δT_c pinning and the broken line is obtained using $H_{dis}(T) \propto \xi(T)$ for δl pinning, where $\xi(T) \approx [(1 + t_1^2)/(1 - t_1^2)]^{1/2}$ and $t_1 = T/T_c$ [section 5.1, page number 138].

4.2 Magnetic Relaxation

The decay of persistent currents with time leads to magnetic relaxation. The magnitude of the persistent current is usually observed to decrease logarithmically or by a Power law with time, depending upon the applied field, pinning energy and temperature. For high T_c superconductors, the relaxation is very fast in comparison with the conventional superconductors because the thermal energy for high T_c materials is usually large (due to the large critical temperatures, enabling operation at high temperatures) and the pinning energy is low (due to large anisotropy and extremely short coherence lengths). Magnetic relaxation measurements have been carried out for pure (y = 0), iron doped (y = 0.016) and heavily Pb doped Bi2212 single crystals. The normalized relaxation rate (S), current-voltage curve (I –V) and effective activation energy U_{eff} have been obtained from the relaxation data. The main objective in this section is to study the effect of c-axis coupling on S, the I-V curve and U_{eff}.

In the magnetic relaxation measurements, the crystals were first zero-field-cooled from above T_c to the desired temperature T. A magnetic field H larger than the field used in the relaxation measurements by several times the field of full penetration was applied [7]. The field was then lowered to the measuring field in "no overshoot" mode of the magnet, and the magnetic moment as a function of time was measured. This procedure ensured an approximately linear flux profile in the crystals. The relaxation data were recorded at different fields around the second peak of the hysteresis loop. The experimental points of the first 100 seconds were not included because of uncertainty in the time that passed between the establishment of the field and the measurement of the first experimental point. Our instrument shows the time measured from the moment the instrument was activated. We obtained the time zero as the time at which the first point

was measured after application of the field. However there is always a delay between the application of the field and the measurement of the first point, which depends on the particular conditions of the experiment (value of initial moment, decay rate, previous experiment). Therefore, there is an uncertainty in measuring the time on the order of 10s. Plotting such measurements on a log t scale would give much distorted and therefore misleading results. Because of this we chose not to use the experimental points for t<100s.

In relaxation measurements, it is well established that the diamagnetic current, i.e. magnetisation, decays with time [10, 19]. The classical equation for the decay of magnetisation is [10, 19]:

$$M_{irr}(t) = \frac{M_{irr}(0)}{\left[1 - \frac{k_B T}{U_0} \ln\left(\frac{t}{t_0}\right)\right]} \qquad (4.2)$$

where $M_{irr}(t)$ and $M_{irr}(0)$ are the irreversible magnetization measured at time t and t= 0, respectively, k_B is the Boltzmann constant and U_0 is the activation energy for $T = 0$. The irreversible magnetization was obtained as $M_{irr} = M - M_{eq}$, where M_{eq} is the equilibrium magnetization: $M_{eq} = (M^- + M^+)/2$. M^- and M^+ are the branches of the hysteresis loop corresponding to the decreasing and increasing fields, respectively.

4.2.1 Normalized Relaxation Rate

The results for the normalized relaxation rate S have been used to study the mechanism of flux pinning in pure, iron doped (y= 0.005) and heavily Pb doped Bi2212 single crystals. From the relaxation data, the normalized relaxation rate, S, was obtained by using the relation:

$$S \equiv \frac{d \ln M_{irr}}{d \ln t} \qquad (4.2.1)$$

Figure 4.2.1.1 shows magnetic relaxation for a pure Bi2212 single crystal at temperatures of 13, 15, 17, 19, 21, 22, 24 and 26 K. The relaxation data were recorded for an applied field H = 620 Oe that was within the second magnetization peak in its magnetic hysteresis loop for all the measured temperatures. The magnetic relaxation for iron doped (y = 0.005) single crystals measured at field H = 520Oe and temperatures T = 15, 17, 19, 21, 23 and 25 K is shown in Fig. 4.2.1.2. In the relaxation, M_{irr} versus time can be described by $M_{irr} \sim t^n$. For both samples, the value of n changes at $t \approx 1{,}000s$, giving two normalized relaxation rates: $S(\mathrm{I})$ for $t \leq 1{,}000s$ and $S(\mathrm{II})$ for $t \geq 1{,}000s$.

A crossover temperature T_{CR} was obtained as the temperature of the peak in plots of the normalized relaxation rate (S) as a function of temperature, for each of the time windows (Fig. 4.2.1.3). T_{CR} was proposed to separate two different pinning regimes: the single vortex pinning regime and the vortex bundle pinning regime [20]. The value of T_{CR} for the pure crystal at a field of 620Oe was 21K for $S(\mathrm{I})$ and 19K for $S(\mathrm{II})$ (Fig. 4.2.1.3). Similarly, the value of T_{CR} for the low iron doped (y = 0.005) Bi2212 single crystal at H = 520Oe was $S(\mathrm{I})$ = 19K and $S(\mathrm{II})$ = 21K, see Fig.4.2.1.4.

Unlike pure Bi2212 single crystal, the Pb doped crystal showed a single power law in $M_{irr}(t)$ for all measured temperatures, see Fig. 4.2.1.5. The relaxation was measured at temperatures 18, 20, 24, 26, 28, 30, 33, 35, 38 and 40K for an applied filed H = 1,200 Oe that was around the second magnetization peak for all these temperatures. A large increase of the crossover temperature T_{CR} in $S(T)$ was observed with lead doping. The observed T_{CR} in the Pb doped crystals was at 35K with H=1,200 Oe (Fig. 4.2.1.6). A similar increase of T_{CR} has been reported for ion irradiated Bi2212 single crystals [20], where the irradiation improved the c-axis coupling of the pancake vortices.This suggested that the unusually strong vortex pinning in heavily Pb doped crystal originated from the improved Josephson coupling of the pancake vortices.

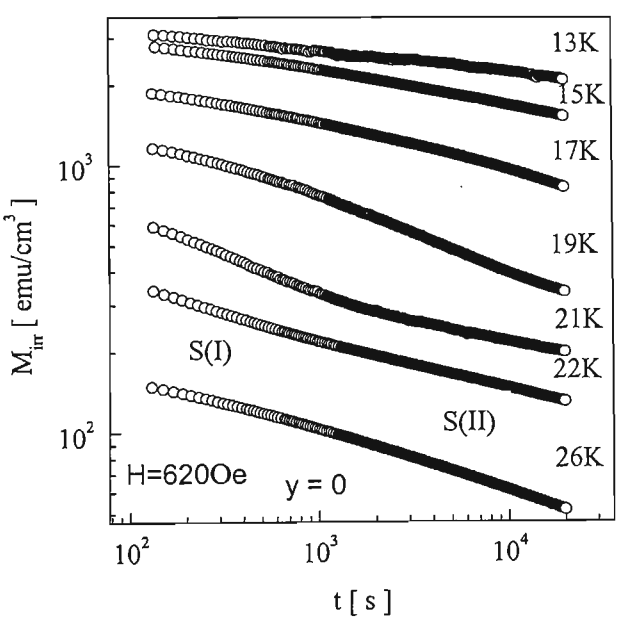

Fig.4.2.1.1: Magnetization M_{irr} vs time for pure Bi2212 single crystal measured at H = 620Oe.The measured temperatures were T =13, 15, 17, 19, 21, 22 and 26K.

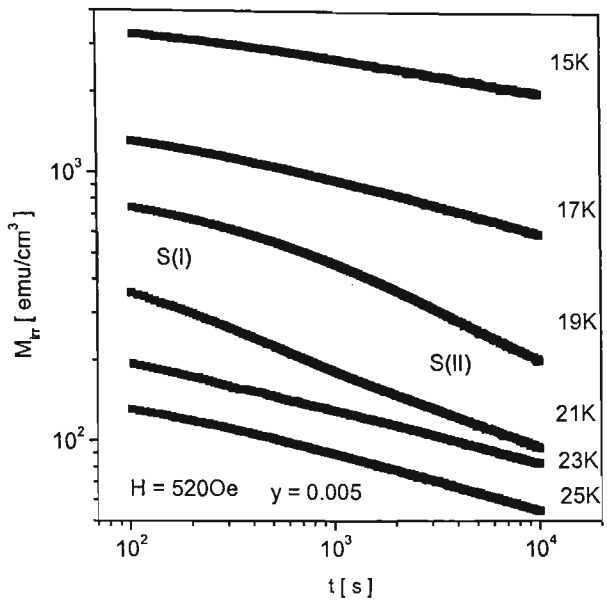

Fig.4.2.1.2: Magnetization M_{irr} vs time for y = 0.005 single crystal measured at H = 520 Oe. The measured temperatures were T =15, 17, 19, 21, 23 and 25K.

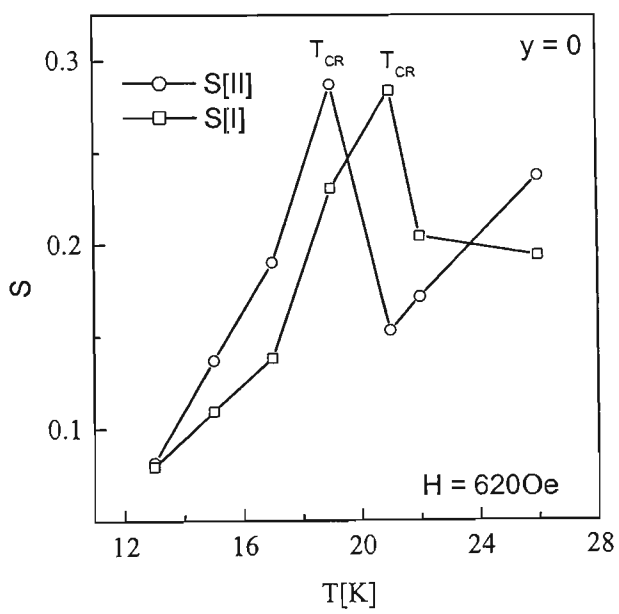

Fig. 4.2.1.3: Normalized relaxation rate S vs T for pure Bi2212 single crystal measured at H = 620 Oe. Here, the time-window of S(I) is t < 1000s and S(II) is t > 1000s.

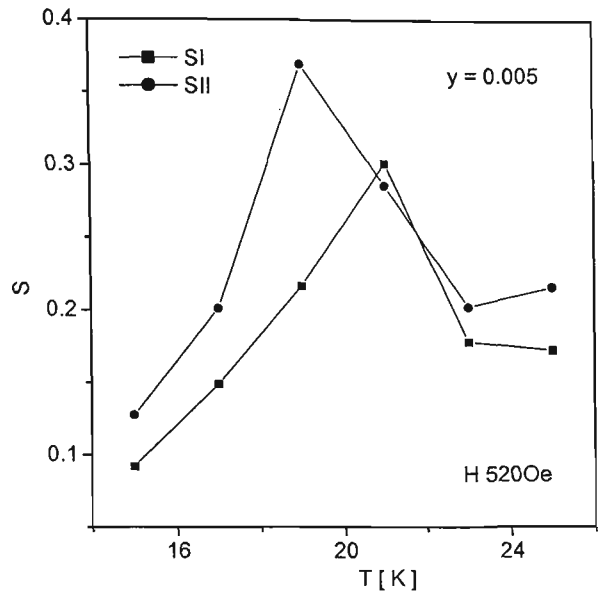

Fig. 4.2.1.4: Normalized relaxation rate S vs T for y = 0.005 Bi2212 single crystal measured at $H = 520$ Oe. Here, the time-window of $S(\mathrm{I})$ is $t < 1000$s and $S(\mathrm{II})$ is $t > 1000$s.

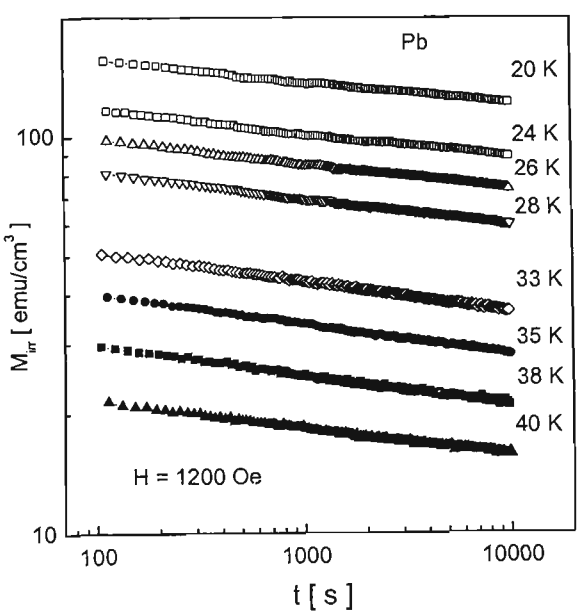

Fig. 4.2.1.5: Magnetization M_{irr} vs time for heavily Pb doped Bi2212 single crystal measured at $H = 620$ Oe. The measured temperatures were $T = 20$, 24, 26, 28, 33, 35, 38 and 40 K.

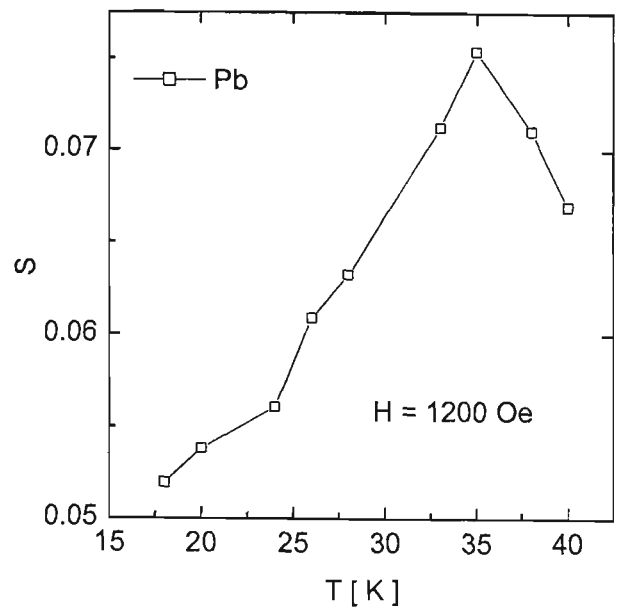

Fig. 4.2.1.6: Normalized relaxation rate S vs T for heavily Pb doped Bi2212 single crystal measured at $H = 1200$ Oe.

In section 4.1.1, the field H_{infl} has been proposed to describe the order-disorder transition. H_{infl} was obtained from the derivative of the magnetization with respect to magnetic field (dM/dH) in a hysteresis loop, where it is the field corresponding to the peak in dM/dH. A study has also been done on the field dependence of the normalized relaxation rate $S(H)$ around the field H_{infl} in the pure, and heavily Pb doped Bi2212 single crystals. A sharp minimum in $S(H)$ has been observed at H_{infl} for the crystals. A similar minimum has been reported at H_{dis} for Y123 crystal [12]. Results of magnetic relaxation measurements for Pb doped single crystals are presented in Fig. 4.2.1.7. The relaxation data were recorded at various fields around the second peak at 35 K. Fig 4.2.1.7 also shows the normalized relaxation rate S. The minimum in $S(H)$ occurs at H_{infl} = 550 Oe for heavily Pb doped Bi2212 single crystal, therefore at the order-disorder transition field.

Fig. 4.2.1.8 shows the magnetic relaxation for a pure Bi2212 single crystal. The relaxation was recorded at various fields around the second peak at $T = 24$ K. Note that the normalized relaxation rate S(H) in pure Bi2212 exhibits a sharp minimum at H_{infl} = 420 Oe. An order-disorder transition field H_{dis} = 380 Oe, independent of temperature, was obtained in Hall probe measurements [8,21]. We propose that the pronounced peak in dM/dH in Figs. 4.1.1.7 and 4.1.1.8, which corresponds to the steepest change in the magnetization (inflection point) on the low field side of the second peak, be interpreted as H_{dis}. This definition of H_{dis} has also been used with Y123 single crystals [15].

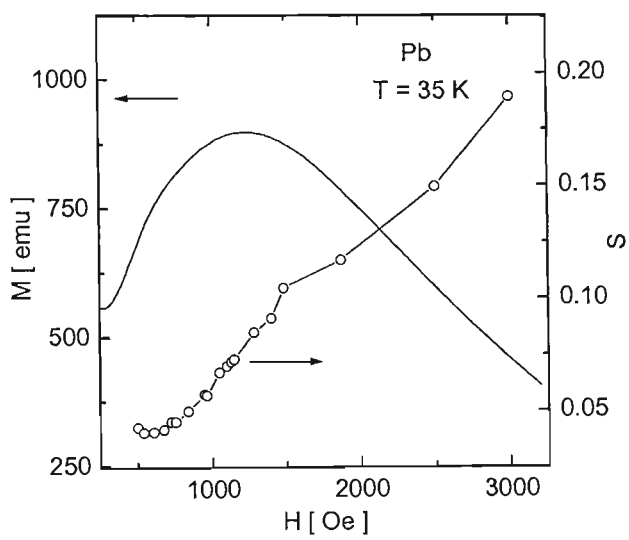

Fig. 4.2.1.7: The magnetization M as a function of applied field H measured at $T = 35$ K for heavily Pb doped single Bi2212 crystal. The normalized relaxation rate $S = |\, d\ln M_{irr} / d\ln t \,|$ is indicated by large open circles.

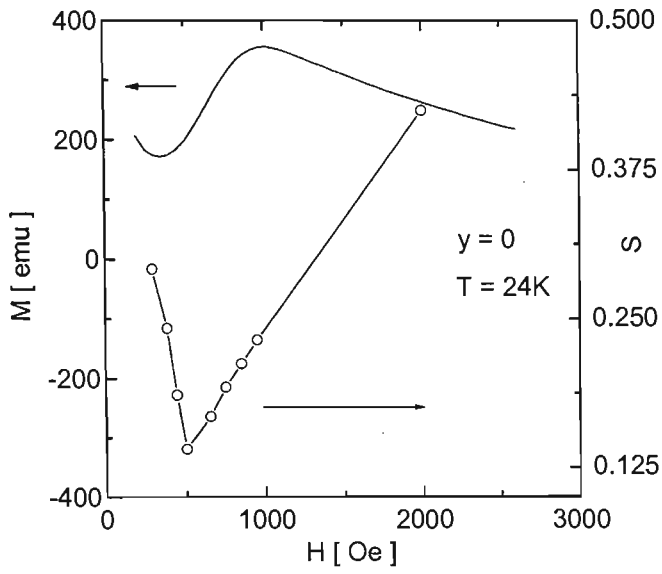

Fig. 4.2.1.8: The magnetization M versus applied field H measured at $T = 35$ K for pure (y = 0) Bi2212 single crystal. The normalized relaxation rate $S = |\, d\ln M_{irr} / d\ln t \,|$ is indicated by large open circles.

4.2.2 Current-Voltage Characteristics

The dependence of the electric field E on the current density J was obtained using relaxation measurements, since $dM_{irr}/dt \sim E$ and $M_{irr} \sim J$ (Bean's relation) [7]. The fourth Maxwell equation gives:

$$\nabla \times \boldsymbol{E} = -\frac{d\boldsymbol{B}}{dt} \qquad (4.2.2.1)$$

For a rectangular shaped sample with breadth 'a' and length 'b', equation 4.2.2.1 can be integrated to give

$$E \cong -l\frac{dB}{dt}, \text{ where } l = \sqrt{a^2 + b^2} \qquad (4.2.2.2)$$

For an applied field H, the total magnetic induction B inside the sample is $B = \mu_0(H + M)$, where M is the magnetization in units of Ampere per meter and $M = M_{irr} + M_{eq}$. Substituting the value of B in equation (4.2.2.2), we have

$$E \cong -l\mu_0\frac{dM}{dt}, \qquad (4.2.2.3)$$

where M_{eq}, H = constant. The $E(J)$ curves obtained from magnetic relaxation for the pure, Fe doped and Pb doped crystal are shown in Figures 4.2.2.1, 4.2.2.2 and 4.2.2.3, respectively. Figure 4.2.2.1 shows a deviation in the $E(J)$ curve for the pure single crystal at about 21K for H = 620 Oe. A similar deviation in $E(J)$ curve is seen for y = 0.005 single crystal at T > 19K, see Fig. 4.2.2.2. This indicated two different pinning regimes above and below 21 K. However, for heavily Pb doped Bi2212 single crystal, the deviation was not observed for the relaxation data when recorded for a time of 10,000 seconds. Because of this, the relaxation data were recorded for a larger time window 30,000 seconds, at temperatures T = 30, 33, 35 and 38K. There was only a hint of a deviation in the $E(J)$curve for the lead doped crystal at T = 38K, see Fig. 4.2.2.3. A clear deviation for this crystal was not observed because of its much smaller value of

S. Since the experimental noise remained the same for all the measurements, the relative noise in $E(J)$ for the Pb-doped crystal was higher and the deviation was masked by the noise.

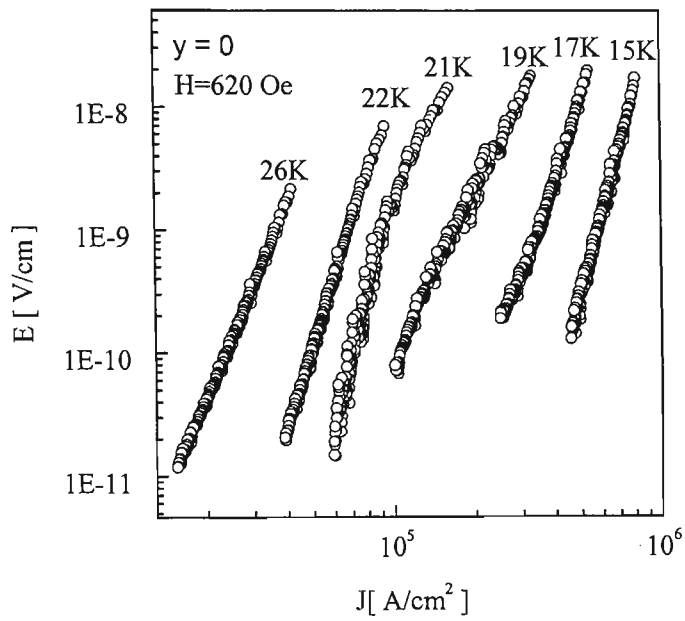

Fig. 4.2.2.1: $E(J)$characteristics for pure Bi2212 single crystal as extracted from the relaxation data for different temperatures and H = 620 Oe.

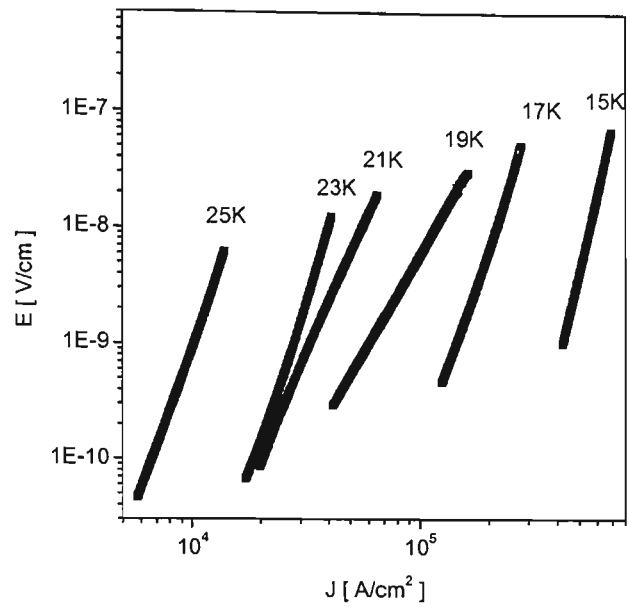

Fig. 4.2.2.2: $E(J)$ characteristics for y = 0.005 Bi2212 single crystal as extracted from the relaxation data for different temperatures and H = 520 Oe.

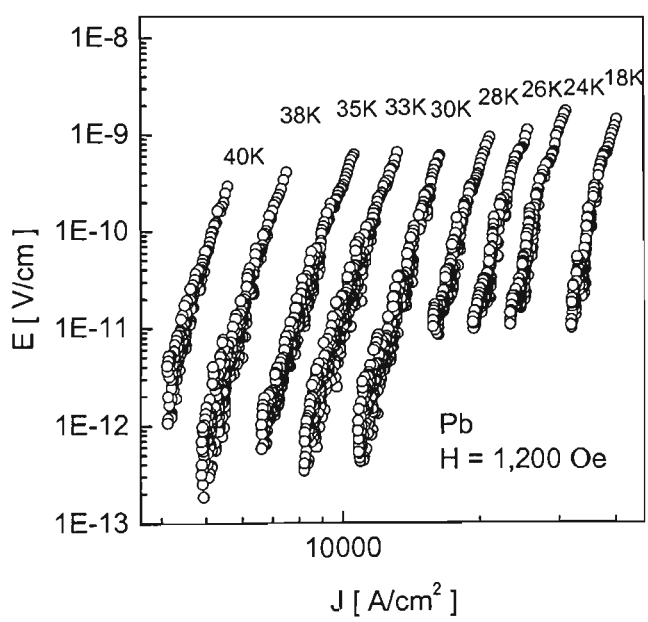

Fig. 4.2.2.3: $E(J)$ characteristics as a function of temperature for heavily lead doped Bi2212 single crystal measured at H = 1,200 Oe.

4.2.3 Effective Activation Energy

To derive the current dependence of the effective activation energy U_{eff} from the relaxation measurements, Maley's method was employed [22]:

$$\frac{U_{eff}(T)}{k_B} = -T\ln\left|\frac{dM_{irr}}{dt}\right| + T\ln\left[\frac{Ha_d\gamma_0}{d\pi}\right] \qquad (4.2.3.1)$$

where γ_0 is the attempt frequency, a_d is the hopping distance of the vortices and d is the thickness of the superconductor. A physically meaningful constant $C = \ln\left(\frac{Ha_d\gamma_0}{d\pi}\right)$ has been obtained as a fitting parameter for a set of relaxation data measured at different temperatures and constant field. An appropriate choice for the value of C resulted in a smooth dependence of U_{eff} on M_{irr}.

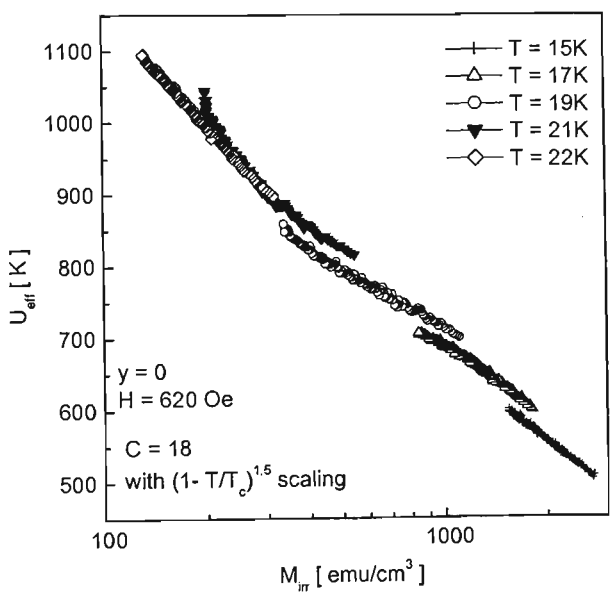

Fig. 4.2.3.1: U_{eff} vs M_{irr} curve for pure Bi2212 crystal at temperatures 15, 17, 19, 21 and 22 K. U_{eff} was obtained using $C = 18$ and $(1-T/T_c)^{1.5}$ scaling.

Figure 4.2.3.1 shows $U_{eff}(M_{irr})$ for pure Bi2212 single crystal at $H = 620$ Oe with C = 18, using a temperature scaling $(1-T/T_c)^{1.5}$. The measured temperatures were 15, 17, 19, 21 and 22 K. During the measurements, the magnetic field was applied parallel to the c-axis. This temperature scaling did not give a smooth curve of U_{eff}. However, a different temperature scaling, $1-(T/T_c)^2$ for U_{eff} gave a smooth curve of $U_{eff}(M_{irr})$ with $C = 18$ (Fig. 4.2.3.2).

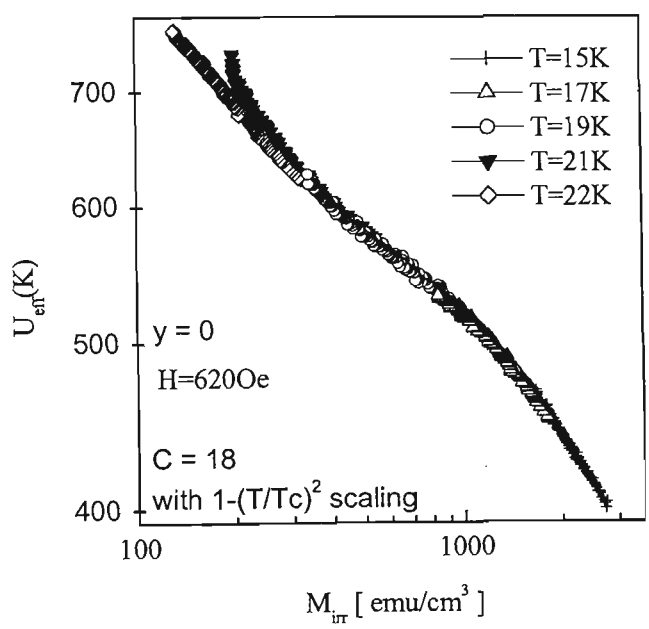

Fig. 4.2.3.2: The dependence of activation energy U_{eff} on the magnetic moment M_{irr} at temperatures 15, 17, 19, 21 and 22 K for pure Bi2212 crystal. U_{eff} was obtained using $C = 18$ and $1-(T/T_c)^2$ scaling.

In Fig. 4.2.3.2, an upward deviation in the U_{eff} curve is also seen at 21 K for a long time-window (i.e. small M_{irr} for a particular T), showing a variation of pinning energy due to different pinning regimes. Other values for C were also tried but did not result in a smooth fit for our measurements (Figs. 4.2.3.3 and 4.2.3.4) [23-25]. Adjusting the value of C without temperature scaling did not result in a smooth U_{eff}, either. Fe-doped (y=0.005) single crystals showed a smooth fit up to 19K with $C=$ 16 by using $1-(T/T_c)^2$, see Fig. 4.2.3.5.

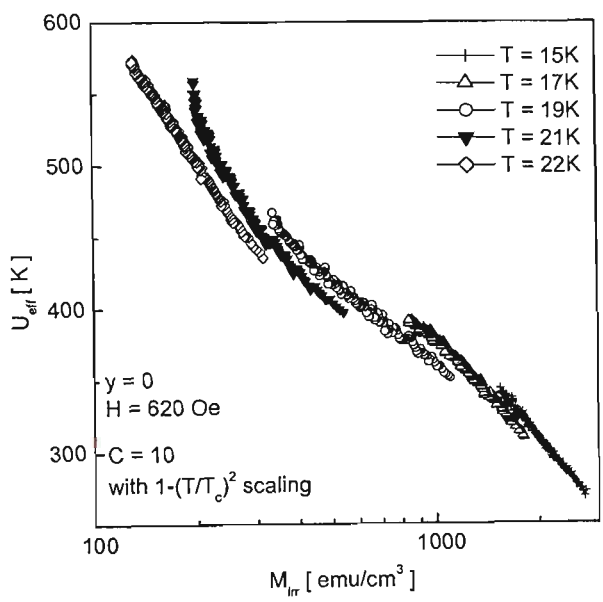

Fig. 4.2.3.3: U_{eff} vs M_{irr} curve for pure Bi2212 crystal at temperatures 15, 17, 19, 21 and 22 K. U_{eff} was obtained using $C = 10$ and $1-(T/T_c)^2$ scaling.

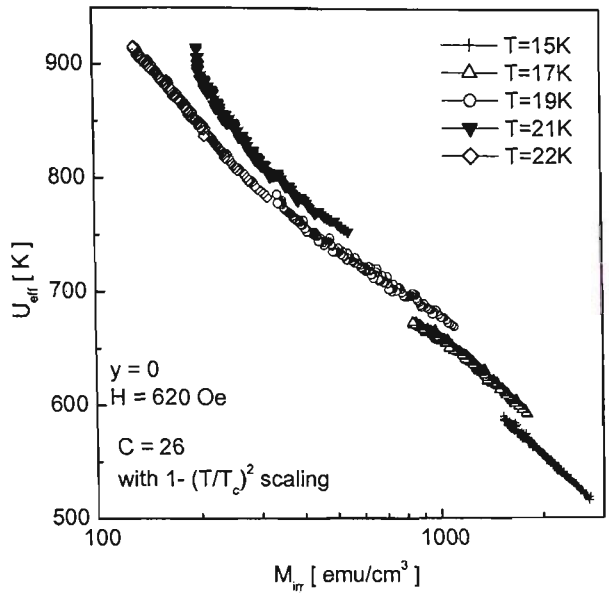

Fig. 4.2.3.4: U_{eff} vs M_{irr} curve for pure Bi2212 crystal at temperatures 15, 17, 19, 21 and 22 K. U_{eff} was obtained using $C = 26$ and $1-(T/T_c)^2$ scaling.

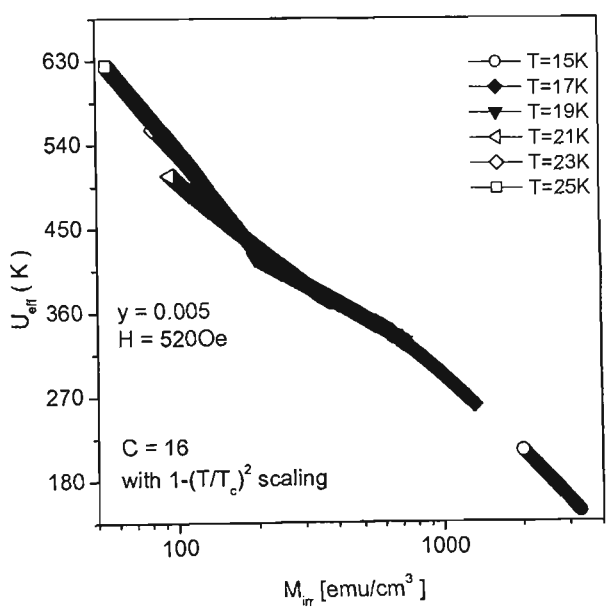

Fig. 4.2.3.5. U_{eff} vs M_{irr} curve for y = 0.005 Bi2212 crystal at temperatures 15, 17, 19, 21, 23 and 25 K. U_{eff} was obtained using $C = 16$ and $1-(T/T_c)^2$ scaling.

In heavily Pb doped crystal, however a smooth curve in $U_{eff}(M_{irr})$ was observed with H = 1200 Oe up to 40 K (Fig. 4.2.3.6). The fit was made with C = 24 and $1-(T/T_c)^2$ scaling.

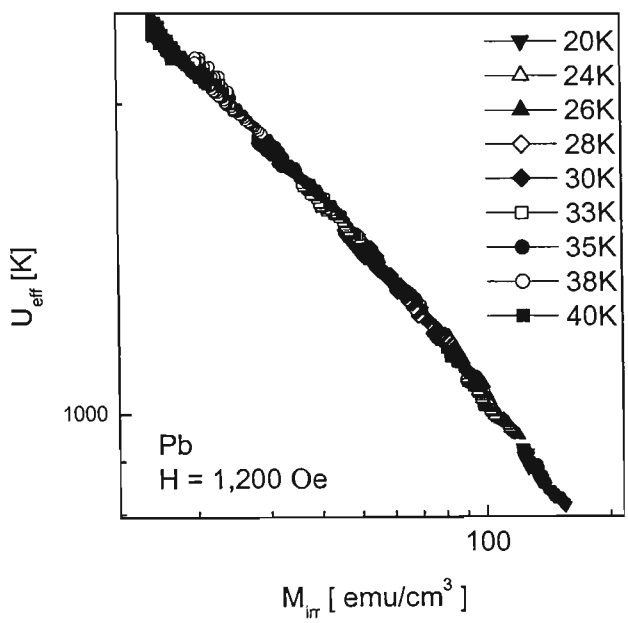

Fig. 4.2.3.6: The dependence of the activation energy U_{eff} on the magnetic moment M_{irr} at temperatures 20, 24, 26, 28, 30, 33, 35, 38 and 40 K for heavily Pb doped Bi2212 single crystal. U_{eff} was obtained using C= 24 and $1-(T/T_c)^2$ scaling.

4.3 Summary of experimental results:

4.3.1 Critical current density J_c and Irreversibility field H_{irr}.

- A significant improvement in the critical current density J_c has been observed for Bi2212 single crystal after Pb doping. However, in Bi2212 single crystals with Fe doping, J_c becomes lower.
- A strong upward shift of the irreversibility field has been observed in Bi2212 single crystal with heavy Pb doping. In contrast to this, Fe doped Bi2212 single crystal has a stronger temperature dependence of H_{irr} .

4.3.2 Temperature dependence of H_{infl} (a field that corresponds to the inflection point in the hysteresis loop), H_{peak} (a field that corresponds to the second magnetization peak) and H_{min} (a field that corresponds to a minimum point between first and second magnetization peak).

- H_{infl} decreases with temperature for heavily Pb doped Bi2212 single crystal. However, a temperature independent of H_{infl} was observed for pure and Fe doped Bi2212 single crystals.
- H_{peak} in heavily Pb doped Bi2212 single crystal appears above 20 K and persists up to critical temperature, T_c, whereas H_{peak} appeared between 20 and 40K for pure and Fe doped Bi2212 single crystals.
- H_{min} decreases with temperature T in heavily Pb doped single crystals. In contrast to this, H_{min} increases in both pure and Fe doped Bi2212 single crystals.

4.3.3 Relaxation behaviour

- T_{CR} (a crossover temperature) in $S(T)$ (normalized relaxation rate) increases for Bi2212 single crystals after heavy Pb doping. However, T_{CR} did not increase in Bi2212 single crystals after Fe doping.

- A deviation in $E(J)$ curve has been observed for pure and Fe doped Bi2212 single crystals at $T \cong 21$ K. This temperature corresponds to the T_{CR} in $S(T)$. No such deviation has been observed for heavily Pb doped Bi2212 single crystal for $T < 38$ K.
- A similar upward deviation from a smooth $U_{eff}(J)$ curve has been observed for pure and Fe doped Bi2212 single crystals at $T = 21$ K. However, no such deviation was observed for heavily Pb doped Bi2212 single crystal.

4.4 References for Chapter four

1. J. Horvat, X. L. Wang and S. X. Dou, *Physica* C **324,** 211 (1999).
2. X. L. Wang, Ph.D thesis, University of Wollongong (2000).
3. G. D. Gu, G. J. Russell and N. Koshizuka, *J. Crystal Growth* **137,** 472 (1994).
4. I. Chong, Z. Hiroi, M. Izumi, J. Shimoyama, Y. Nakayama, K. Kishio, T. Terashima, Y. Bando and M. Takano, *Science* **276,** 770 (1997).
5. T. Motohashi, Y. Nakayama, T. Fujita, K. Kitazawa, J. Shimoyama and K. Kishio, *Phys. Rev. B* **59,** 14080 (1999).
6. B. vom Hedt, W. Lisseck, K. Westerholt and H. Bach, *Phys. Rev. B* **49,** 9898 (1994).
7. Y. Yeshurun, A. P.Malozemoff and A. Shaulov, *Rev. Mod. Phys.* **68** 911 (1996).
8. C. P. Bean, *Phys. Rev. Lett.* **8,** 250 (1962).
9. H. Küpfer, Th. Wolf, C. Lessing, A.A. Zhukov, X. Lanccon, R. Meier-Hirmer, W. Schauer, and H. Wühl, *Phys. Rev. B* **58,** 2886 (1998).
10. G. Blatter, M. V. Feigel'man, V. B. Geshkenbein, A. I. Larkin and V. M. Vinokur, *Rev. of Mod. Phys.* **66,** 1125 (1994).
11. M. Kosugi, Y. Matsuda, M. B. Gaifullin, K. Kumagai, N. Chikumoto, J. Shimoyama, K. Kishio, K. Hirata and M. Konczykowski *Physica* C **293** 208 (1997).
12. D. Giller, A. Shaulov, Y. Yesurun, J. Giapintzakis, *Phys. Rev. B* **60,** 106 (1999).
13. S. Kokkaliaris, A. A. Zhukov, P. A. J. de Groot, R. Gagnon, L. Taillefer, T. Wolf, *Phys. Rev. B* **61,** 3655 (2000).
14. Y. Abulafia, A. Shaulov, Y. Wolfus, R. Prozorov, L. Burlachkov, Y. Yeshurum, D. Majer, E. Zeldov and V. M. Vinokur, *Phys. Rev. Lett.*, **77** 1596 (1996).

15. T. Nishizaki, T. Naito, S. Okayasu, A. Iwase and N. Kobayashi, *Phys. Rev. B* **61,** 3649 (2000).

16. D. Giller, A. Shaulov, R. Abulafia, Y. Wolfus, L. Burlachkov, Y. Yeshurun, *Phys. Rev. Lett.* **79** 2542 (1997).

17. M. Baziljevich, D. Giller, M. McElfresh, Y. Radzyner, J. Schneck, T. H. Johansen and Y. Yeshurun, *Phys. Rev. B* **62** 4058 (2000).

18. B. Khaykovich, M. Konczykowski, E. Zeldov, R. A. Doyle, D. Majer, P. H. Kes, T. W. Li, *Phys. Rev. B* **56,** R517 (1997).

19. M. V. Feigel'man, V. B. Geshkenbein and V. M. Vinokur, *Phys. Rev. B* **43**, 6263 (1991).

20. V. V. Metlushko, G. Guntherodt, I. N. Goncharov, A. Yu. Didyk, V. V. Moshchalkov and Y. Bruynseraede *Physica B,* **194-196**, 2219 (1994).

21. M. F. Goffman, J. A. Herbsommer, F. de la Cruz, T. W. Li and P. H. Kes, *Phys. Rev. B* **57,** 3663 (1998).

22. M. P. Maley, J. O. Willis, H. Lessure and M. E. McHenry, *Phys. Rev. B* **42,** 2639 (1990).

23. P. J. Kung , M. P. Maley, M. E. McHenry, J. O. Willis, M. Murakami and S. Tanaka, *Phys. Rev. B* **48,** 13922(1993).

24. H. Darhmaoui and J Jung, *Phys. Rev. B* **57,** 8009 (1998).

25. Hai-hu Wen, P. Ziemann, H. A. Radovan and T. Herzog, *Physica C* **305,** 186(1998).

CHAPTER FIVE: DISCUSSION

5. DISCUSSION

5.1 Critical Current Density

A distinct improvement in critical current density J_c was observed for Bi2212 single crystal with heavy lead doping. Figures 4.1.1.1 and 4.1.1.2 suggest that heavy Pb substitution suppresses flux flow at high temperature and leads to increase in J_c. The weak field dependence of J_c/J_{c0} for lead doped crystal (Figs. 4.1.1.3, 4.1.1.4 and 4.1.1.5) has also indicated strong vortex pinning in this crystal, as compared to the pure (y = 0) and Fe doped (y = 0.005, 0.016, 0.022) Bi2212 single crystals. The field dependence of J_c/J_{c0} at 20K was weaker for the pure crystal, as compared to that for the Pb-doped crystal (Fig. 4.1.1.5). However, for T = 30K, Fig. 4.1.1.3 shows that J_c/J_{c0} for the pure crystal had become strongly field dependent. As discussed in section (2.7.2), the vortices below 20K are in the 0D pinning regime. Strongly disordered point defects present in the 0D pinning regime can act as strong pinning centres. The dominant energy in the 0D pinning regime is also proposed to be the pinning energy ($U_{pin} > U_{shear}$ or U_{tilt}) [1]. This resulted in the weak field dependence of J_c/J_{c0} as a function of field in the pure single crystal. But at higher temperatures (T =30K) and higher fields, due to the large anisotropy of Bi2212 and thermal excitation, the vortices are easily unpinned from their pinning sites, and therefore J_c became strongly field dependent. However, the lead doped crystal showed a weak field dependence of J_c/J_{c0} over a wide range of fields at 30K, indicating a strong pinning at this temperature, see Fig. 4.1.1.3. The improved Josephson coupling in heavily Pb doped Bi2212 single crystal can be responsible for strong pinning. The role of the

Josephson coupling in the enhancement of vortex pinning has been discussed in various papers [1,2,3]. An approximate relationship between the Josephson coupling of the pancake vortices and the inter-layer conductivity was obtained in [4].

Z. Hiroi et. al. have reported that the observed two-phase microstructure i. e. lead rich and lead poor lamellar plates for $x > 0.4$ in their heavily Pb doped $Bi_{2.2-x}Pb_xSr_{1.8}CaCu_2O_{8+\delta}$ single crystals, was responsible for the improved pinning [5]. The lead content in our $Bi_{2-x}Pb_xSr_8CaCu_2O_{8+\delta}$ crystal was roughly 0.34. This corresponds to the same ratio of Bi to Pb as for $x = 0.4$ in the crystals studied by Hiroi et al [5]. They also reported a regular structural modulation with $x = 0.4$, leading to homogeneous morphology. In our heavily Pb doped Bi2212 single crystal, studies on the surface morphology using Atomic Force Microscopy (AFM) have indicated the presence of laminae. There was also another evidence supporting the existence of the laminae in our crystal [6]. However, it is believed that the frequency of their occurrence should be small because of relatively low level of Pb doping. We therefore believe that the pinning in our heavily Pb doped crystal was not dominated by these defects.

A weak field dependence of J_c/J_{c0} indicated an improved vortex pinning in the $y = 0.005$ crystal with small Fe doping (Fig. 4.1.1.6). It is believed that the small Fe content in $y = 0.005$ crystal can introduce point-like pinning centres which pin vortices, thus improving J_c/J_{c0}. The Fe, being a 3d element, replaces Cu atoms in the CuO_2 planes. The critical temperature is observed to be strongly suppressed with increasing Fe-doping. This suppression is explained in terms of the pair breaking scattering mechanism introduced by magnetic impurities in CuO_2 planes [7]. In other words, the

superconducting order parameter is suppressed with Fe-doping. B. Vom Held et al. have reported a decrease in the coherence length (ξ) with increasing Fe concentration [7]. This decrease in ξ with Fe doping has been proposed to explain the low J_c/J_{c0} in y = 0.016 and 0.022 crystals, see Fig. 4.1.1.6. The field dependence of J_c/J_{c0} for $T/T_c = 0.30$ has qualitatively the same results as for $T = 24K$, showing that the results are not affected by different values of T_c for the crystals (Fig. 4.1.1.7). Fig. 4.1.2.1 shows that heavy Pb doping in Bi2212 single crystal enhances the irreversibility field, H_{irr}. However, H_{irr} is not improved with Fe doping in Bi2212 single crystals.

5.2 Second Magnetization Peak

The pronounced second magnetization peak of the hysteresis loop $M(H)$ (peak effect) in the heavily Pb doped Bi2212 crystals of Fig. 4.1.3.1 reflects the enhanced vortex pinning. The second peak appears below 20K and persists up to T_c, see Fig.4.1.3.2. A strong peak close to T_c has also been reported for Y123 single crystals [8]. Several articles discuss the origin of the peak effect in Y123 single crystals with various types of defects [8-18]. The peak effect in Y123 crystals is crucially dependent on the defects such as twin structures and columnar defects [8,9,11,12]. Intrinsic pinning from the CuO_2 plane is also suggested for the origin of the peak effect in Y123 crystal [19].

Motohashi et al. have observed a resistivity anisotropy, $\gamma \cong (\rho_c/\rho_{ab})^{1/2}$ for heavily Pb doped Bi2212 single crystal approximately one order of magnitude smaller than for pure Bi2212 single crystals [19]. For example, the heavily Pb doped Bi2212 single crystals have c-axis resistivity $\rho_c \sim 0.2\Omega$cm and pure Bi2212 single crystals have $\rho_c \sim 3$ Ωcm [19]. Winkeler et al. have reported that the Josephson interlayer coupling energy increases 3.5 times with heavy Pb doping in Bi2212 single crystals [20]. The increased

coupling energy enhances the layer coupling in heavily Pb doped single crystal, which thus aligns the pancake vortices into strongly coupled stacks that behave as 3D vortex lines, similar to the vortex lines in Y123 [21,22]. Distortion of the vortex lines and the proliferation of long-range topological defects in the vortex lattice are also proposed as the origin of peak effect in [23,24]. It is therefore believed that one of the possible answers for the origin of the strong peak effect in the heavily Pb doped single crystals comes from their 3D vortex lines.

The second peak in the height of the magnetic hysteresis loop (ΔM) of pure and iron doped Bi2212 single crystals is absent below 20 K, see Fig. 4.1.3.4a, b. When a magnetic field H is applied perpendicular to the CuO_2 layers, vortex lattice is proposed to have three relevant energy scales, namely, the tilt energy $U_{tilt} \approx c_{44}(R_c)[(r_p/L_c)^2 R_c^2 L_c]$, the shear energy $U_{shear} \approx c_{66}\ .[(r_p/L_c)^2 R_c^2 L_c]$ and the pinning energy $U_{pin} \approx (\gamma_p \xi^4 R_c^2 L_c / r_p^2 a_0^2)^{1/2}$. Here c_{44} is the dispersive tilt modulus, c_{66} is the shear modulus, r_p is the range of the pinning force, γ_p is the disorder strength, L_c is the Larkin correlation Length, and R_c is the collective pinning radius [25,1]. These energies can be used to distinguish the four possible pinning regimes in Bi2212 single crystals: 0D pinning regime ($U_{pin} > U_{tilt}, U_{shear}$), 1D pinning regime ($U_{tilt} > U_{pin} > U_{shear}$), 2D pinning regime ($U_{shear} > U_{pin} > U_{tilt}$) and 3D pinning regime ($U_{tilt}, U_{shear} > U_{pin}$) [18,19]. In pure Bi2212 single crystal, the vortices below 20K are said to be in the ``0D pinning regime '' and the vortices are proposed to be individually pinned [25,1]. This is because the Larkin correlation length along the c-axis $L_c \approx \varepsilon\xi\,(J_0/J_c)^{1/2} \approx$12 - 16 Å in Bi2212 crystal which is close to the layer spacing s = 15 Å [1,26]. Here, ε is the mass anisotropy parameter, J_0 is the depairing current density at $T = 0$ K, and ξ is the coherence length. In principle, $L_c \leq$ s implies highly disordered vortex structure. Below 20 K, disordered point defects

can act as strong pinning centers [23]. The absence of the second peak in the pure Bi2212 single crystals may be caused by these strong point defects.

Above 20 K, the Larkin correlation length L_c and the collective pinning radius R_c grow very fast as a result of the thermal depinning [18]. For L_c > s, the collectively pinned object is a vortex line [1]. In order to neglect interaction between the vortex lines, the magnetic field must be weak enough, so that $L_c < \varepsilon a_0$ [1]. In Bi2212 single crystals, for fields $H < \Phi_0/\lambda^2$ and temperatures between 20 and 40 K, the vortices are in the 1D pinning region, where single vortex lines are pinned individually [25]. Here, λ is the penetration depth and Φ_0 is the flux quantum. In this regime, the shear modulus c_{66} decreases exponentially with H,

$$c_{66} \approx \frac{\varepsilon_0}{\lambda^2}\left(\frac{H\lambda^2}{\Phi_0}\right)^{1/4} e^{-\sqrt{\Phi_0/H\lambda^2}} \qquad (5.2.1)$$

where ε_0 is the energy of the isolated vortex line. Thus in the 1D pinning regime, the shear energy U_{shear} becomes smaller than both the U_{tilt} and U_{pin} energies. At fields $H > \Phi_0/\lambda^2$ and temperatures > 20K, the shear energy grows linearly with field H,

$$c_{66} \approx \frac{\varepsilon_0 H}{4\Phi_0} \qquad (5.2.2)$$

and U_{shear} becomes larger than U_{tilt} and U_{pin}. The vortex line thus gradually enters into the 3D pinning regime. It is proposed that the second magnetization peak appears at about the field $H \approx \Phi_0/\lambda^2$, where the vortex lines go from the 1D to the 3D pinning regime [25]. In pure Bi2212 single crystals, the second magnetization peak appears for temperatures between 20 and 40K. Figure 4.1.3.3 shows the peak effect for pure (y = 0) and iron doped (y = 0.005, 0.016 and 0.016) Bi2212 single crystals at 24K. At higher fields, a crossover from the 3D to the 2D pinning regime is predicted [25]. Above 40 K, no clear peaks are observed since thermal fluctuations dominate the pinning energy.

As for pure single crystal, Fe doped Bi2212 single crystals exhibit the peak effect between 20 and 40 K. Figure 4.1.3.4 shows the absence of the peak effect at 20 and 40K for Fe doped Bi2212 single crystals. In the Fe doped single crystals, the main defects are reported to reside in the CuO_2 planes, since Fe replaces Cu in the plane [7]. The *c*-axis conductivity is not improved with Fe doping in this crystal. Thus the peak effect in Fe doped Bi2212 single crystals can be described in a similar way as it is depicted for pure Bi2212 single crystal. This suggests that the dimensionality of the vortices (pancake stacks or Abrikosov flux lines) play a dominant role in the occurrence of a strong peak effect.

In the following, we will discuss the effects of Pb and Fe doping on the three characteristic fields H_{min}, H_{infl} and H_{peak} of Bi2212 single crystals.

It is well known that the relationship between the vortex pinning energy, the vortex elastic energy, and the thermal fluctuation energy, may be used to estimate the conditions for different vortex phases to occur, namely, the vortex liquid phase, a weakly disordered quasi-lattice (Bragg glass) and a highly disordered solid phase (entangled or amorphous solid). The vortex liquid phase results from the competition between the elastic energy of the vortex lattice and the thermal energy k_BT. Similarly, the amorphous vortex solid phase may be estimated from the competition between the elastic energy and the pinning energy of the vortex lattice. The elementary pinning forces collectively interact with the elastic vortex lattice. This interaction is characterized by the size of the correlation volume $V_c \approx (4/3\pi)R_c^2L_c$, within which the order of the vortex lattice is established and the pinning forces are correlated. Here, the

Larkin lengths L_c and R_c are the longitudinal and transverse size of the ellipsoid-shaped correlation volume.

In this dissertation we interpreted the inflection point H_{infl} in the magnetization curves as the field H_{dis} which separates the weakly disordered vortex lattice from the strongly disordered entangled vortex lattice ($H_{min} < H_{infl} < H_{max}$). In pure Bi2212 single crystals, we observed $H_{dis} \approx 420$ Oe independent of temperature up to $T = 40$ K, see Figs. 4.1.3.7 and 4.1.3.9. An order-disorder transition field $H_{dis} \approx 380$ Oe, independent of temperature, was obtained in Hall probe measurements [23,27]. We suggest that the pronounced peak in $| dM/dH |$ in Figs 4.1.1.7 and 4.1.1.8, which corresponds to the steepest change of the magnetization (inflection point) on the low field side of the second peak, may be interpreted as H_{dis}. This definition of H_{dis} has also been used with Y123 single crystals [10]. The minimum observed in the normalized relaxation rate $S(H)$ of pure Bi2212 crystals in Figs. 4.2.1.7 and 4.2.1.8 also indicates two different flux creep processes in the two solid regimes: in one S is decreasing and in the other S increasing with increasing H. This minimum occurs at the same field as H_{infl}. Above $T = 40$ K, the vortex lattice in pure Bi2212 single crystals has been reported to undergo a first order melting transition, where a negative slope of the melting line separates the vortex solid phase from the vortex liquid phase [27].

Recently, Avraham et al. have observed a "melting line" below $T = 40$ K in pure Bi2212 single crystals using a shaking technique that reduces the pinning-caused irreversibility by applying a small ac magnetic field perpendicular to the applied dc field [28]. They observed a positive slope of the "melting line" in H_{irr} versus temperature diagram at about $T = 40$ K and a temperature independent "melting line" extending to temperatures

below 40 K, coinciding with the temperature-independent second magnetization peak field. The authors inferred that a first order transition between ordered and disordered vortex phases occurs in this experiment below 40 K. However, the second peak disappears below 20 K. This may mean that the first order transition also disappears at 20 K, implying that $T = 20$ K is a critical point. But this is unlikely, because the order-disorder transition involves a change in the symmetry of the vortex structure, see also the discussion in [29]. It is also possible that the Bi2212 superconductor becomes 2D at this temperature, which again means 0D pinning and thus may be the reason for the disappearance of the second peak. There are indeed numerous reports showing that 0D pinning sets in below 20 K in Bi2212 single crystals [25, 27].

As with pure Bi2212 single crystals, H_{dis} in Fe doped Bi2212 single crystals was observed to be independent of temperature. The values of H_{dis} for single crystals with y = 0.005, 0.016 and 0.022 were around 350 Oe, 185 Oe and 170 Oe, respectively, see Figs. 4.1.3.7 and 4.1.3.9 for the y = 0.016 crystal. However, in heavily Pb doped single crystals, H_{dis} was found to decrease with increasing temperature, see Figs. 4.1.3.8 and 4.1.3.9. The temperature dependence of H_{dis} has also been reported for Y123 [10]. The magnetic phase diagram of the vortices in Y123 shows 3D-vortex lines over a wide range of fields and temperatures [1]. We therefore have reason to believe that the observed T dependence of H_{dis} (T) in Pb doped single crystals comes from its improved c axis coupling or 3D vortex behaviour.

The peak field H_{peak} in all the crystals is observed to decrease with increasing temperature, see Fig. 4.1.3.5. The minimum field H_{min} in the pure and iron doped Bi2212 single crystals is observed to increase with increasing temperature whereas in

heavily Pb doped single crystals, it is observed to decrease, see Fig. 4.1.3.6. The geometric and surface barriers are reported to dominate vortex pinning at low fields [30-32]. All our crystals were of approximately the same rectangular shape. Therefore, the effects of these barriers should not produce two opposite temperature dependences of H_{min} in pure or iron doped Bi2212 single crystals and in heavily Pb doped single crystals.

The theoretical temperature dependence of the order-disorder transition field $H_{dis}(T)$ has been obtained [29]. The $H_{dis}(T)$ values for the single vortex pinning regime and for the small bundle and large bundle pinning regimes are calculated by Mikitik et al.[29]. For the single vortex pinning regime, $H_{dis}(T)$ is given by

$$H_{dis} = \frac{\Phi_0 c_L^2}{\xi^2}\left(\frac{c_L L_c}{\varepsilon\xi}\right)^{\alpha} \qquad (5.2.3)$$

where c_L is the Lindemann constant, L_c is the Larkin correlation length, ε is the mass anisotropy parameter, Φ_0 is the flux quantum, ξ is the coherence length and $\alpha = 2\varsigma/(1 - \varsigma) \approx 3$ (here ς is the roughness exponent). The parameter $\varepsilon\,\xi / L_c$ generally depends upon the temperature T by the following relation:

$$\frac{\varepsilon\xi(T)}{L_c(T)} = Dg_0(t) \qquad (5.2.4)$$

with $g_0(t) = [1-(t)^2]^{1/2}$ for δl pinning (caused by spatial fluctuations of the electron mean free path), $g_0(t) = [1-(t)^2]^{-1/6}$ for δT_c pinning (caused by spatial fluctuations of the transition temperature), where $t = T/T_c$ and $D = \varepsilon\xi(0)/L_c(0)$ is the strength of the quenched disorder. Substituting equation 5.2.4 in equation 5.2.3 and using D, one obtains $H_{dis}(T) \propto \xi(T)$ for δl pinning and $H_{dis}(T) \propto \xi(T)^{-3}$ for δT_c pinning, where $\xi(T) \approx [(1 + t^2)/(1 - t^2)]^{1/2}$.

We have used both these functions to fit our experimental data for H_{min}, H_{infl} and H_{peak}. For pure Bi2212 single crystal, a temperature independence of $H_{infl} \approx H_{dis}$ is observed at low temperatures, see Fig. 4.1.3.9 (curve y=0). In this particular case, the data allowed us to fit H_{infl}(T) by the equation, $H_{dis}(T) \propto \xi(T)$ for δl pinning, with the choice of $H_{dis}(0)$ = 420 Oe. The fitted curve showed almost no temperature dependence. The more strongly T dependent $H_{min}(T)$ and $H_{peak}(T)$ do not allow a fit by either of these formulas. A similar behaviour was observed in Fe doped Bi2212 single crystal (curve y = 0.016 in Fig. 4.1.3.9) with fitted $H_{dis}(0)$ = 180 Oe. For the heavily Pb doped single crystal in Fig.4.1.3.9, the δT_c pinning formula fits our data, with $H_{dis}(0)$ = 560 Oe.

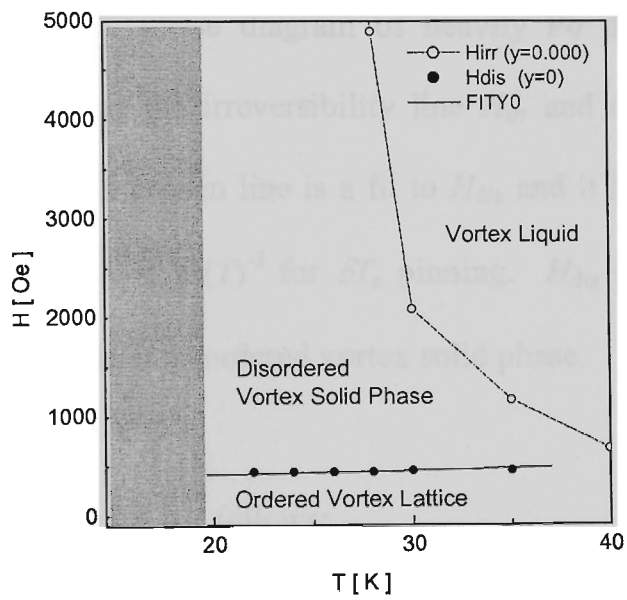

Figure 5.2.1: Magnetic phase diagram of pure (y = 0) Bi2212 single crystal showing the irreversibility field line H_{irr} and order-disorder transition line H_{dis}. The solid line is obtained using the relation $H_{dis}(T) \propto \xi(T)$ for δl pinning. H_{dis} separates the ordered vortex lattice from the disordered vortex phase. The shaded area indicates zero dimensional pinning regime.

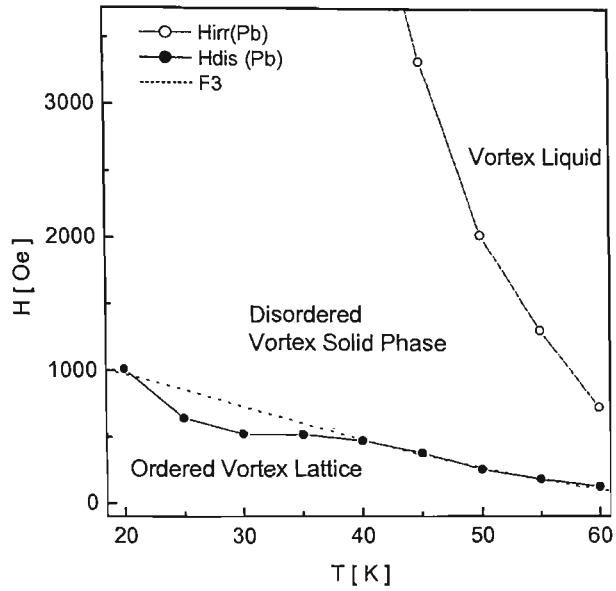

Figure 5.2.2: Magnetic phase diagram of heavily Pb doped Bi2212 single crystal indicating the irreversibility line H_{irr} and order-disorder transition line H_{dis}. The broken line is a fit to H_{dis} and it is obtained using the relation $H_{dis}(T) \propto \xi(T)^{-3}$ for δT_c pinning. H_{dis} separates the ordered vortex lattice from disordered vortex solid phase.

This section is summarized as follows:

- In pure Bi2212 single crystals, no second magnetization peak H_{peak} appears below 20 K. Below 20K, 2D pancake vortices are individually pinned (they are said to be in zero dimensional (0D) pinning regime.
- Second peak appears between 20 and 40 K for pure Bi2212 single crystal. Between 20 and 40 K regime, the 2D pancake vortices couple to form vortex lines and topological distortion of this flux line is proposed for the origin of the peak.

- Second peak appears up to critical temperature T_c in Bi2212 single crystal after heavy Pb doping. An enhanced *c*-axis coupling of the 2D pancake vortices with heavy Pb doping is proposed for the enhanced second peak.
- H_{peak} does not change quantitatively for Bi2212 single crystal with Fe doping. The peak appears between 20 and 40 K. It is proposed that Fe doping does not enhance *c*-axis coupling.
- A temperature independent order-disorder transition field H_{dis} has been observed for pure and iron doped Bi2212 single crystal crystals.
- A decrease of H_{dis} with temperature has been observed for heavily Pb doped Bi2212 single crystal crystals. This temperature dependence of H_{dis} is related to the improved c-axis coupling.
- The minimum field H_{min} increases with temperature for both pure and iron doped Bi2212 single crystals, however it decreases for heavily Pb doped Bi2212 single crystal.

5.3 Normalized Relaxation Rate

A peak in $S(T)$ was observed for the heavily lead doped crystal with the temperature of the peak $T_{CR} = 35K$ (Fig. 4.2.1.6). No peak in $S(T)$ was observed for Y123 crystals [33,34]. There was always an increase of S with T for Y123, with a plateau at intermediate temperatures. The increasing $S(T)$ generally obeys a flux creep relation obtained from the collective pinning theory [34]. However, the peak in $S(T)$ for the pure and Pb doped Bi2212 single crystals could not be explained by the collective pinning theory. It has been suggested that the peak in $S(T)$ for single crystal Bi2212 represents a crossover regime from single vortex pinning to vortex bundle pinning [35]. Another publication reported that the peak was associated with a dimensional crossover from a 3D to a 2D vortex lattice [36]. M. Reissner claimed that the peak corresponded to the transition from bulk to surface pinning [37]. R. A. Doyle et al. and N. Morozov et al. reported that the surface barrier effects dominated vortex dynamics only in the absence of strong bulk pinning, which was obtained in very clean Bi2212 crystals at about 40K [25, 27]. D. T. Fuchs at el. also reported that the bulk pinning regime occurred below T = 36K and the surface barrier pinning regime for 70K $\geq T \geq$ 36K [26]. In contrast to this, A. Mazilu at el. reported that only bulk pinning affected the flux dynamics in pure Bi2212 single crystals [38]. Therefore, it can be said that the peak in $S(T)$ generally occurs as a consequence of a transition between two different types of vortex pinning that dominate the relaxation process.

A large increase of T_{CR} to higher temperatures was also reported for ion irradiated Bi2212 crystals [35]. It was claimed that the strong pinning in the ion irradiated crystals was due to improved inter-layer Josephson coupling of pancake vortices along

the irradiation damage tracks [28,39]. As for ion irradiated Bi2212 single crystal, the increase in the *c*-axis conductivity by one order of magnitude in heavily Pb doped single crystals leads to stronger Josephson coupling of the pancake vortices, and it is believed that this coupling is responsible for the increase of T_{CR} in the heavily Pb doped crystals.

Depending on the experimental time window, different values of T_{CR} are observed for pure (y = 0) and iron doped (y = 0.005) Bi2212 single crystal. For example, for pure Bi2212 single crystals at H = 620 Oe, T_{CR} = 19K and 21K was obtained for the time windows $S(\mathrm{II})$ and $S(\mathrm{I})$, respectively (Fig. 4.2.1.3). Similar values of T_{CR} were observed for Fe doped (y = 0.005) Bi2212 single crystal at H = 520 Oe, see Fig. 4.2.1.4 for both, S(I) and S(II). This indicated that the pancake coupling did not improve in Fe doped Bi2212 single crystal, since the increase of T_{CR} is related to the improvement of the *c*-axis coupling. Theoretically, the change in the pinning process for the individual flux lines in Bi2212 single crystals is expected at a temperature $T_L^* = \Phi_0\sqrt{B}/(2\pi\kappa)^2 \cong 30\mathrm{K}$, where $\kappa = \lambda/\xi$ is the Ginzburg-Landau parameter [40]. The two values of T_{CR} obtained for the same field, but different experimental time windows, suggested that there was a possibility of two different vortex pinning regimes before and after 1,000*s* of relaxation measurements, see Figs. 4.2.1.3 and 4.2.1.4.

5.4 Current-Voltage Curve

Fig. 4.2.2.1 shows a deviation in $E(J)$ for pure Bi2212 at an approximate temperature T = 21K and a field H = 620 Oe. The observed deviation in $E(J)$ also demonstrated a transition from one pinning regime to another. A similar $E(J)$ result has been observed for iron doped (y= 0.005) Bi2212 single crystals, see Fig. 4.2.2.2. No such deviation in

the $E(J)$ curve was observed for the heavily Pb doped crystal, although there was a hint of the deviation at 38K for a long relaxation time (Fig. 4.2.2.3). This was probably due to the very small value of S, resulting in an increased scatter of experimental points in $E(J)$, thereby masking out the deviation.

5.5 Effective Activation Energy

Maley et al. has described a method for extracting J-dependence of effective pinning potential, $U_{\text{eff}}(J)$, from magnetic relaxation data [41]. This procedure begins with collecting magnetic relaxation data at different temperatures. Remembering that $J \propto M_{\text{irr}}$, the equation (2.7.5.6) suggests that U_{eff} is related to $-k_B T \ln(dM_{irr}/dt)$. By plotting the expression $-k_B T \ln(dM_{irr}/dt)$ as a function of M_{irr} at different temperatures T, a set of curves is found which are vertically shifted with respect to each other. However, in relaxation measurements the principal effect of increasing temperature is to produce monotonically decreasing value of M_{irr}. Maley showed that a selection of single constant $C = \ln(Ha_d\gamma_0/\pi\ d)$ multiplied by a temperature T for each temperature can result in all of the relaxation data to fall onto a smooth dependence of U_{eff} on M_{irr}. Here γ_0 is the attempt frequency, a_d is the hopping distance and d is the thickness of the superconductor. However, Maley's approach to elucidating the explicit dependence of U_{eff} on M_{irr} by using a single value of C for each field does not always result in a smooth curve over a wide range of temperatures, especially for the higher temperatures in high T_c superconductors. Various groups have presented evidence that a smooth $U_{eff}(\Sigma_{irr})$ dependence measured over a wide temperatures range can be obtained by an appropriate temperature scaling of U_{eff} [42-48]. This is because the energy scale associated with vortex motion must also reflect the scaling of fundamental

pinning related parameters (such as coherence length) with temperature and field [42]. There are different temperature scaling laws for the activation energy. M. Tinkham mentioned in 1988 that the height of the activation barrier $U_{\text{eff}}/k_B T$ can be scaled by $g(t_1) = 1 - t_1^2 (1 - t_1^4)^{\frac{1}{2}} / t_1$, where $t_1 = T/T_c$ [42]. He proposed that the value of $g(t_1)$ for the relaxation data taken at higher temperatures is $(1 - t_1)^{\frac{3}{2}}$. This scaling did not work well with our crystals, see Fig. 4.2.3.1.

P.J. Kung et al. proposed that, keeping the applied field constant, the activation energy U_{eff} (M_{irr}, T) can usually be expressed in the following scaling form to separate its thermal dependence [45]:

$$U_{\text{eff}}(M_{\text{irr}}, T) = G(T)\, U_{\text{eff}}(M_{\text{irr}}, 0) \qquad (5.5.1)$$

Here, G(T) is the temperature dependence function, which is chosen as

$$G(T) = \left[1 - \left(\frac{T}{T_{irr}}\right)^2\right]^m \qquad (5.5.2)$$

where $1 \le m \le 2$ and T_{irr} is the irreversibility temperature. They studied this scaling property in Y-Ba-Cu-O. In the present study, the same temperature scaling as that employed by P. J. Kung was used except that T_{irr} was replaced by T_c. A similar $1 - (T/T_c)^2$ temperature scaling was suggested by Tinkham for the relaxation data taken at low temperatures. In pure Bi2212 single crystals a $1 - (T/T_c)^2$ scaling worked well with the choice of a physically meaningful value of the constant C = 18, Fig.4.2.3.2. Other values of C did not bring a smooth dependence of $U_{eff}(M_{irr})$, see Figs. 4.2.3.3 and 4.2.3.4. In all measured crystals, the $1 - \left(\frac{T}{T_c}\right)^2$ scaling was attempted. The smooth fit of $U_{eff}(M_{irr})$ obtained over a temperature range of $20K - 35K$ for lead doped crystal

also indicated that there was only one type of pinning regime up to 35K (Fig. 4.2.3.6). Similarly, pure Bi2212 single crystal shows a smooth $U_{eff}(M_{irr})$ up to 21K for an applied field of 620 Oe, and Fe doped Bi2212 single crystals up to 21K for 520 Oe, see Figs. 4.2.3.2 and 4.2.3.5. The upward deviation from the fit in $U_{eff}(M_{irr})$ was obtained for long relaxation times in the pure crystals. This deviation probably also corresponded to a change in the vortex pinning process.

5.6 References for Chapter Five

1. G. Blatter, M. V. Feigel'man, V. B. Geshkenbein, A. I. Larkin and V. M. Vinokur *Rev. Mod. Phys* **66,** 1125 (1994).
2. M. Kosugi, Y. Matsuda, M. B. Gaifullin, K. Kumagai, N. Chikumoto, J. Shimoyama, K. Kishio, K. Hirata, and M. Konczykowski, *Physica C* **293,** 208 (1997).
3. N. Morozov, M. P. Maley, L. N. Bulaevskii and J. Sarrao *Phys. Rev. B* **57** R8146 (1998).
4. K. K. Uprety and D. Dominguez, *Phys. Rev. B* **51,** 5955 (1995).
5. Z. Hiroi, I. Chong and M. Takano, *J. Solid State Chem* **138,** 98 (1998).
6. J. Horvat, X. L. Wang and S. X. Dou, *Physica C* **324,** 211(1999).
7. B. vom Hedt, W. Lisseck, K. Westerholt and H. Bach, *Phys. Rev. B* **49,** 9898 (1994).
8. H. Küpfer, Th. Wolf, C. Lessing, A. A. Zhukov, X. Lançcon, R. Meier-Hirmer, W. Schauer, and H. Wühl, *Phys. Rev. B* **58,** 2886 (1998).
9. W. K. Kwok, J. A. Fendrich, C. J. van der Beek, and G. W. Crabtree, *Phys. Rev. Lett.* **73,** 2614 (1994).
10. T. Nishizaki, T. Naito, S. Okayasu, A. Iwase, N. Kobayashi, *Phys. Rev. B* **61,** 3649 (2000).
11. M. Oussena, P. A. J. de Groot, R. Gagnon, and L. Taillefer, *Phys. Rev. Lett.* **72,** 3606 (1994).
12. S. Okayasu, M. Sasase, N. Kuroda, A. Iwase, Y. Kazumata and T. Kambara, *Physica C.* **357,** 505-508 (2001).
13. V. Vinokur, B. Khaykovich, E. Zeldov, M. Konczykowski, R. A. Doyle and P. H. Kes, *Physica C* **295,** 209 (1998).

14. D. Giller, A. Shaulov, R. Abulafia, Y. Wolfus, L. Burlachkov and Y. Yeshurun, *Phys. Rev. B* **79,** 2542 (1997).

15. S. Kokkaliaris, P. A. J. de Groot, S. N. Gordeev, A. A. Zhukov, R. Gagnon and L. Taillefer, *Phys. Rev. Lett.* **82,** 5116 (1999).

16. Y. Paltiel, E. Zeldov, Y. Myasoedov, M. L. Rappaport, G. Jung, S. Bhattacharya, M. J. Higgins, Z. L. Xiao, E. Y. Andrei, P. L. Gammel and D. J. Bishop, *Phys. Rev. Lett.* **85,** 3712 (2000).

17. A. E. Koshelev and V. M. Vinokur, *Phys. Rev. B* **57,** 8026 (1998).

18. H. Küpfer, A. A. Zhukov, A. Will, W. Jahn, R. Meier-Hirmer, T. Wolf, V. I. Voronkova, M. Kläser and K. Saito, *Phys. Rev. B* **54,** 644 (1996).

19. T. Motohashi, Y. Nakayama, T. Fujita, K. Kitazawa, J. Shimoyama and K. Kishio, *Phys. Rev. B* **59**, 14080 (1999).

20. L. Winkeler, S. Sadewasser, B. Beschoten, H. Frank, F. Nouvertné and G. Güntherrodt, *Physica C* **265,** 194 (1996).

21. K. K. Uprety, J. Horvat, X. L. Wang, M. Ionescu, H. K. Liu and S. X. Dou, *Supercond. Sci. Technol.* **14,** 479 (2001).

22. M. Baziljevich, D. Giller, M. McElfresh, Y. Radzyner, J. Schneck, T. H. Johansen and Y. Yeshurun *Phys. Rev. B* **62,** 4058 (2000).

23. M. F. Goffman, J. A. Herbsommer, F. de la Cruz, T. W. Li and P. H. Kes, *Phys. Rev. B* **57,** 3663 (1998).

24. E. H. Brandt, *Phys. Rev. B* **34,** 6514 (1986).

25. M. Nideröst, A. Suter, P. Visani, A. C. Mota and G. Blatter, *Phys. Rev. B* **53,** 9286 (1996).

26. V. F. Correa, J. A. Herbsommer, E. E. Kaul, F. de la Cruz, and G. Nieva, *Phys. Rev. B* **63,** 092502-1 (2001).

27. B. Khaykovich, M. Konczykowski, E. Zeldov, R. A. Doyle, D. Majer, P. H. Kes, and T. W. Li, *Phys. Rev. B* **56,** R517 (1997).

28. N. Avraham, B. Khaykovich, Y. Myasoedov, M. Rappaport, H. Shtrikman, D. E. Feldman, T. Tamegai, P. H. Kes, M. Li, M. Konczykowski, K. V. D. Beek and E. Zeldov, *Nature* **411,** 451 (2001).

29. G. M. Mikitik and E. H. Brandt, *Phys. Rev. B* **64,** 184514 (2001).

30. R. A. Doyle, S. F. W. R. Rycroft, C. D. Dewhurst, E. Zeldov, I. Tsabba, S. Reich, T. B. Doyle, T. Tamegai, S. Ooi, *Physica C* **308,** 123 (1998).

31. D. T. Fuchs, E. Zeldov, M. Rappaport, T. Tamegai, S. Ooi, and H. Shtrikman, *Nature* **391,** 373 (1998).

32. N. Morozov, E. Zeldov, M. Konczykowski, R. A. Doyle, *Physica C* **291** 113 (1997).

33. Y. Yeshurun, A. P. Malozemoff and A. Shaulov, *Rev. Mod. Phys.* **68,** 911 (1996).

34. J. R. Thompson, Y. R. Sun, L. Civale, A. P. Malozemoff, M. W. McElfresh, A. D. Marwick and F. Holtzberg, *Phys. Rev. B* **47,** 14440 (1993).

35. V. V. Metlushko, G. Guntherodt, I. N. Goncharov, A. Yu. Didyk, V. V. Moshchalkov and Y. Bruynseraede, *Physica B* **194-196,** 2219 (1994).

36. A. K. Pradhan, S. B. Roy, P. Chaddah, C. Chen and B. M. Wanklyn, *Phys. Rev. B* **49,** 12984 (1994).

37. M. Reissner, *Physica C* **290,** 173 (1997).

38. A. Mazilu, H. Safar, D. Lopez, W. K. Kwok, G. W. Crabtree, P. Guptasarma and D. G. Hinks, *Phys. Rev. B* **58,** R8913 (1998).

39. A. E. Koshelev, P. Le Doussal and V. M. Vinokur, *Phys. Rev. B* **53,** 8855 (1996).

40. M. V. Feigel'man and V. M. Vinokur, *Phys. Rev. B* **41,** 8986 (1990).

41. M. P. Maley, J. O. Willis, H. Lessure and M. E. McHenry, *Phys. Rev. B* **42,** 2639 (1990).

42. M. Tinkham, *Phys. Rev. Lett.* **61,** 1658 (1988)

43. M. E. McHernry, S. Simizu, H. Lessure, M. P. Maley, J. Y. Coulter, I. Tanaka and H. Kojima, *Phys. Rev. B* **44** 7614 (1991).

44. P. J. Kung, M. P. Maley, M. E. McHenry, J. O. Wills, M. Murakami and S. Tanaka, *Phys. Rev. B* **46,** 6427 (1992).

45. P. J. Kung, M. P. Maley, M. E. Mchernry, J. O. Wills, M. Murakami and S. Tanaka, *Phys. Rev. B* **48,** 613923 (1993).

46. M. Reissner and J. Lorentz, *Phys. Rev. B* **56,** 6273 (1997).

47. Y. G. Xiao, B. Yin, J. W. Li, Z. X. Zhao, X. K. Fu, H. T. Ren and L. Xiao, *J. Appl. Phys.* **81,** 2309 (1997).

48. H. Darhmaoui and J. Jung, *Phys. Rev. B* **57,** 8009 (1998).

CHAPTER SIX: CONCLUSIONS

6.1 Conclusions

Magnetization measurements have been performed for heavily Pb doped Bi2212 single crystals and for $Bi_{2.1}Sr_{1.9}Ca_{1.0}(Cu_{1-y}Fe_y)_2O_{8+\delta}$ single crystals with Fe content y= 0, 0.005, 0.016 and 0.022. The heavily Pb doped crystal was prepared using the self flux growth method [1]. The Fe doped and pure Bi2212 crystals were prepared by floating zone method [2]. The quality of the crystals was studied with the help of X-ray diffraction (XRD) and Atomic Force Microscopy (AFM). The critical temperature, T_c, of the crystals was measured using an *ac* susceptibility measurement. The y = 0, 0.005, 0.016 and 0.022 crystals had T_c = 88.5, 82.25, 73 and 65.5K, respectively. The heavily Pb doped crystal had T_c = 69 K.

In heavily Pb doped crystals, a strong second magnetization peak (peak effect) has been observed up to the critical temperature T_c, whereas in Bi2212 crystals with y = 0, 0.005, 0.016 and 0.022, no second peak was observed above 40K. A similar strong peak has been reported in Y123 single crystals [3]. Y123 has a resistivity anisotropy parameter, $\gamma^2 = \rho_c / \rho_{ab} \approx 10^3$, whereas pure Bi2212 crystals have $\gamma^2 \approx 10^5$ [4,5]. This suggested that the strong pinning in Y123 probably originated in stronger coupling of 2D pancake vortices. Furthermore, the *H-T* phase diagram of Y123 shows the presence of 3D vortex lines over a wide range of fields and temperatures [6]. In heavily Pb doped single crystals, Motohashi et al. have reported a *c*-axis conductivity that was one order of

magnitude larger than in pure Bi2212 single crystals, resulting in a significant reduction of anisotropy in the resistivity, $\gamma^2 = \rho_c / \rho_{ab} \approx 10^3$ [7]. Winkeler et al. have reported that the Josephson coupling energy was increased by 3.5 times in heavily Pb doped Bi2212 single crystal as compared to pure Bi2212 single crystal [8]. The increased coupling energy enhances the inter-layer coupling in heavily Pb doped single crystal, which thus aligns the pancake vortices into strongly coupled stacks that behave as 3D vortex lines, similar to the vortex lines in Y123. There is therefore reason to believe that the pronounced peak, which reflects strong vortex pinning behaviour in heavily Pb doped single crystals, originates from the improved Josephson coupling in heavily Pb doped Bi2212 single crystals. The second peak is not improved in Bi2212 single crystals after Fe doping. In Fe doped single crystals, point defects are reported to reside in the CuO_2 planes, since Fe replaces Cu in the CuO_2 plane [9]. The c-axis coupling is not improved with Fe doping in this crystal, and thus pancake coupling does not improve either. The peak field H_{peak} in all the crystals is observed to decrease with increasing temperatures, T.

We also observed a significant increase of the value of T_{CR}, a crossover temperature separating two different pinning regimes, with the heavy Pb doping of Bi2212 single crystal. The T_{CR} for heavily Pb doped single crystal is at 35 K. A similar increase of T_{CR} toward higher temperature has been reported for ion irradiated Bi2212 single crystals [10]. However, for the Fe doped crystals, T_{CR} did not increase toward higher temperature. The T_{CR} for pure (y = 0) and Fe (y = 0.005) doped crystals is 19K. In ion irradiated Bi2212 crystal, increased c-axis coupling has been reported [11]. This improved c axis coupling, which aligns 2D pancake into 3D vortex lines, has been interpreted as resulting in the increase of T_{CR} in ion irradiated single crystals [12]. A

similar argument has been proposed for the increase of T_{CR} in heavily Pb doped single crystals.

Studies of the temperature dependence of the field $H_{infl}(T)$ have also been made for pure, Fe doped and heavily Pb doped Bi2212 single crystals. Here, $H_{infl}(T)$ corresponds to a field value at which an inflection in the $M(H)$ curve occurs on the low-field-side of the peak. All single crystals showed a pronounced peak in $|dM/dH|$ versus H at $H_{infl}(T)$. We have related $H_{infl}(T)$ to the field $H_{dis}(T)$, an order-disorder field that separates a weakly elastically disordered vortex lattice from a plastically disordered vortex solid. A minimum observed in the normalized relaxation rate $S(H)$ at H_{infl} indicates two different flux-creep mechanisms above and below that field and two different solid vortex phases. In pure Bi2212 single crystals, we observed H_{dis} = 420 Oe, independent of temperature up to 40K. A similar result has also been confirmed by Hall Probe measurements [13]. In heavily Pb doped single Bi2212 crystals, $H_{dis}(T)$ was observed to decrease with increasing T. It is proposed that the temperature dependence of $H_{dis}(T)$ in heavily Pb doped single crystals comes from the 3D vortex behaviour. However, in all the Fe doped crystals, a temperature independent H_{dis} is observed.

In the course of our research some other ideas were conceived that would further elucidate the mechanisms of the increased pinning with heavy Pb doping, but which could not be realized in the limited time-frame of this Ph.D candidature. In heavily Pb doped Bi2212 single crystals, a significant reduction in the resistivity anisotropy parameter i. e. improved c-axis conductivity is proposed for the enhanced second peak H_{peak} (up to T_c), the decrease of order-disorder transition field H_{dis} with T and increase of crossover temperature T_{CR} with T. The reduction in the resistivity anisotropy

parameter has also been reported for heavily Pb doped Bi2212 single crystal after irradiating it with heavy ion beam [14]. Thus, it is believed that the study on the temperature dependence of H_{peak}, H_{dis} and T_{CR} for the heavy ion irradiated heavily Pb doped Bi2212 single crystals will help further clarifying a role of c-axis conductivity for the strong vortex pinning behaviour in the heavily Pb doped single crystals.

In heavily Pb doped single crystals, the resistivity anisotropy parameter, $\gamma = \rho_c/\rho_{ab}$, is determined using a standard dc-four probe technique. Here, ρ_c is out of plane resistivity and ρ_{ab} is in plane resistivity. No measurement has been carried out for determining the mass anisotropy parameter, $\varepsilon_m = M_c / M_{ab}$ of heavily Pb doped single crystals. Here M_c is the perpendicular and M_{ab} is the in-plane effective mass of the superconducting carriers. It is therefore useful to determine mass anisotropy parameter in the heavily Pb doped Bi2212 single crystals using torque magnetometer and also it will be interesting to compare the mass anisotropy parameter obtained from the magnetometer with the resistivity anisotropy parameter described in the literature. An experimental determination of the resistivity anisotropy parameter and mass anisotropy parameter has been described in the section [2.5.2].

6.2 References for Chapter Six:

1. J. Horvat, X. L. Wang and S. X. Dou, *Physica* C **324,** 211 (1999).
2. G. D. Gu, G. J. Russell, and N. Koshizuka, *J. Cryst. Growth* **137,** 472 (1994).
3. H. Küpfer, Th. Wolf, C. Lessing, A. A. Zhukov, X. Lançcon, R. Meier-Hirmer, W. Schauer, and H. Wühl, *Phys. Rev. B* **58** 2886 (1998).
4. T. Motohashi, Y. Nakayama, T. Fujita, K. Kitazawa, J. Shimoyama, and K. Kishio, *Phys. Rev. B* **59,** 14080 (1999).
5. T. A. Friedmann, M. W. Rabin, J. Giapitzakis, J. P. Rice and D. M. Ginsberg, *Phys. Rev. B* **42,** 6217 (1990).
6. G. Blatter, M. V. Feigel'man, V. B. Geshkenbein, A. I. Larkin, V. M. Vinokur, *Rev. Mod. Phys* **66,** 1125 (1994).
7. T. Motohashi, Y. Nakayama, T. Fujita, K. Kitazawa, J. Shimoyama and K. Kishio, *Phys. Rev. B* **59,** 14080 (1999).
8. L. Winkeler, S. Sadewasser, B. Beschoten, H. Frank, F. Nouvertné and G. Güntherrodt, *Physica C* **265,** 194 (1996).
9. B. vom Hedt, W. Lisseck, K. Westerholt and H. Bach, *Phys. Rev. B* **49,** 9898 (1994).
10. V. V. Metlushko, G. Guntherodt, I. N. Goncharov, A. Yu. Didyk, V. V. Moshchalkov and Y. Bruynseraede, *Physica B* **194-196,** 2219 (1994).
11. M. Kosugi, Y. Matsuda, M. B. Gaifullin, K. Kumagai, N. Chikumoto, J. Shimoyama, K. Kishio, K. Hirata, and M. Konczykowski, *Physica C* **293,** 208 (1997).
12. K. K. Uprety, J. Horvat, X. L. Wang, M. Ionescu, H. K. Liu and S. X. Dou, *Supercond. Sci. and Technol.* **14,** 479 (2001).

13. B. Khaykovich, E. Zeldov, D. Majer, T. W. Li, P. H. Kes and M. Konczykowski, *Phys. Rev. Lett.* **76,** 2555 (1996).

14. Y. Nakayama, T. Motohashi, K. Otzichi, J. Shimoyama, K. Kitazawa, K. Kishio, M. Konczykowski, N. Chikumoto, *Phys. Rev. B.* **62,** 1452-6 (2000).

1. K. K .Uprety, J. Horvat, X. L. Wang, G. D. Gu, H. K. Liu and S. X. Dou, "Field and temperature dependence of critical current density of Fe doped Bi2212 single crystals", *Physica C*, **341-348** (2000) 1351

2. K. K .Uprety, J. Horvat, X. L. Wang, M. Ionescu, H. K. Liu and S. X. Dou, " Flux creep in heavily lead doped Bi2212 single crystal", *Physica C* **341-348** (2000) 1369.

3. X.L. Wang, J. Horvat, G.D. Gu, K.K. Uprety, H.K. Liu, and S.X. Dou, "Enhanced flux pinning by Fe point defect in Bi2Sr2CaCu1-xFexO8+d single crystals", *Physica C* **337** (2000) 221.

4. K. K .Uprety, J. Horvat, X. L. Wang, M. Ionescu, H. K. Liu and S. X. Dou "Enhancement of vortex pinning by Josephson coupling of two-dimensional pancake vortices in heavy lead-doped $Bi_{2-x}Pb_xSr_2CaCu_2O_y$ single crystals" *Supercond Sci and Technol* **14** (2001) 479.

5. K. K. Uprety, J. Horvat, X. L. Wang, M. Ionescu, E. H. Brandt, H. K. Liu, S. X. Dou "Order-disorder transition in Bi2212 single crystals doped with Fe and Pb" *Phys. Rev. B*, **65**, 224501 (2002).

6. P.N. Mikheenko, K. K. Uprety and S.X. Dou
Handbook of superconducting materials (D1.2. BSSCO) in Press Institute of Physics, London

7. K. K. Uprety, J. Horvat, X. L. Wang, M. Ionescu, H. K. Liu, S. X. Dou and E. H. Brandt "Magnetic Hysteresis and relaxation in Bi2212 single crystals doped with Fe and Pb", will be published in *IEEE Transactions on Applied Superconductivity* (June, 2003).